Three-dimensional single particle tracking in a light sheet microscope

Dissertation zur Erlangung des Doktorgrades (Dr. rer. nat.)
der Mathematisch-Naturwissenschaftlichen Fakultät
der Rheinischen Friedrich-Wilhelms-Universität Bonn

vorgelegt von

Jan-Hendrik Spille

aus Oldenburg (Oldb.)

Bonn, Dezember 2013

Angefertigt mit Genehmigung der Mathematisch-Naturwissenschaftlichen Fakultät der Rheinischen Friedrich-Wilhelms-Universität Bonn.

In der Dissertation eingebunden:

Zusammenfassung

Lebenslauf

1. Gutachter: Prof. Dr. Ulrich Kubitscheck
2. Gutachter: Prof. Dr. Rudolf Merkel

Tag der Promotion: 24. April 2014

Erscheinungsjahr: 2014

Zusammenfassung

Technische Weiterentwicklung im Bereich der Mikroskopie und insbesondere der Fluoreszenzmikroskopie ermöglicht die Untersuchung immer feinerer Details biologischer Proben. Das Zusammenspiel von spezifischer Markierung, ausgefeilten optischen Aufbauten und empfindlichen Detektoren erlaubt sogar die Beobachtung einzelner fluoreszenzmarkierter Moleküle. Mit schnellen Videomikroskopen ist es so möglich, molekulare Mechanismen in lebenden Zellen durch Verfolgung einzelner Moleküle mit hoher räumlicher und zeitlicher Auflösung direkt zu beobachten. Die Einzelmolekülverfolgung kann detaillierte Informationen über die Dynamik dieser Vorgänge liefern. Technische Voraussetzungen für die Einzelmolekülbeobachtung begrenzen die Schärfentiefe der Beobachtung jedoch auf weniger als 1 µm. Daher ist die Einzelmolekülverfolgung oft auf Untersuchungen in planaren Membranen beschränkt. In ausgedehnten Proben basiert sie oft auf der Analyse von zweidimensionalen Projektionen kurzer Trajektorienfragmente.

Im Rahmen dieser Arbeit wurde diese Limitierungen durch eine Kombination aus Echtzeitlokalisierung einzelner Teilchen in drei Dimensionen und aktiver Rückkopplungsschleife überwunden. Ein ausgewähltes Teilchen wurde innerhalb des Beobachtungsvolumens gehalten. Zu diesem Zweck wurde ein Lichtscheibenmikroskop entworfen und an einem kommerziellen Weitfeldmikroskop aufgebaut. Es wurde mit einem schnellen Piezo-Hubtisch zur axialen Probenpositionierung ausgestattet. Dreidimensionale Ortsinformationen wurden mittels astigmatischer Detektion in die Form der Punktspreizfunktion eingeprägt und mit einem hierzu entwickelten Echtzeit-Bildanalysealgorithmus ausgelesen. Um Teilchen anhand weniger detektierter Photonen verfolgen zu können, wurde eine auf Kreuzkorrelation mit Masken basierende Lokalisationsmetrik entwickelt. Während der Nachbearbeitung der Daten wurden aus den Bildern gewonnene, relative axiale Lokalisierungen mit der Position des Hubtisches zu vollen, dreidimensionalen Trajektorien kombiniert.

Die mechanischen und optischen Eigenschaften des Aufbaus wurden mit geeigneten Prüfproben sorgfältig charakterisiert. Es konnte eine Zeitauflösung von 1,12 ms erzielt werden. Die Lokalisierungsgenauigkeit der Methode wurde experimentell durch wiederholte Abbildung immobilisierter fluoreszenter Partikel bestimmt. Die Fähigkeit einzelne Emitter zu verfolgen wurde an einem biochemischen Modellsystem nachgewiesen. Lipide wurden mit einzelnen synthetischen Farbstoffmolekülen markiert und in die Lipiddoppelschicht von unilamellaren Riesenvesikeln integriert, sodass sie auf der sphärischen Oberfläche der Vesikel verfolgt werden konnten. Trajektorien von mehr als 20 s Dauer konnten bei lediglich 130 detektierten Photonen pro Signal aufgenommen werden. Eine Analyse der photophysikalischen Eigenschaften zeigte, dass die Länge der Trajektorien nicht durch die Genauigkeit der Trackingmethode, sondern durch Photobleichen der Farbstoffe begrenzt war.

Um die Anwendbarkeit der Methode in biologischen Proben nachzuweisen, wurden

fluoreszente Nanopartikel in die Kerne von *C. tentans* Speicheldrüsenzellen mikroinjiziert. Die Teilchen konnten länger als 270 s in mehreren Tausend Bildern verfolgt werden.
Anschließend wurde die Methode benutzt, um mRNA und rRNA Partikel ebenfalls in den Zellkernen von *C. tentans* Speicheldrüsenzellen zu verfolgen. Die Biomoleküle wurden mit komplementären, bis zu drei Farbstoffmoleküle tragenden Oligonukleotiden spezifisch markiert. So war es möglich, Trajektorien von ≥ 4 s Dauer und 4 - 5 µm axialer Ausdehnung von Teilchen mit einem Diffusionskoeffizienten von 1 - 2 $\mu m^2/s$ aufzunehmen. Die längsten Trajektorien dauerten mehr als 16 s und deckten dabei 10 µm in axialer Richtung ab. Im Vergleich zu Messungen mit normaler 2D Einzelmolekülverfolgung wurden sowohl Beobachtungsdauer als auch axiale Ausdehnung der Trajektorien um mehr als eine Größenordnung erhöht. Dadurch war es möglich, Mobilitätszustände nicht anhand eines Ensembles von kurzen Beobachtungen, sondern individuell für einzelne Teilchen zu untersuchen.

Summary

Technical development in microscopy, and particularly in fluorescence microscopy, has facilitated the investigation of ever smaller details in biological specimen. The combination of specific labeling of molecular compounds, sophisticated optical setups and sensitive detectors enables observation of single molecules. Using fast video microscopy, it is now possible to directly observe the cell's *molecular machinery at work* by tracking single molecules with high spatial and temporal resolution. Single molecule tracking can reveal detailed information about the dynamics of biological processes. However, technical requirements for single molecule detection limit the depth of field to less than 1 µm. Thus, single molecule tracking is typically limited to studying phenomena in planar membranes or, in extended specimen, often relies on two dimensional projections of short trajectory fragments.

The work presented here strives to overcome these limitations by combining real-time three-dimensional localization of single particles with an active feedback loop to keep a particle of interest within the observation volume. To this end, a light sheet microscopy setup was designed and assembled around a commercial microscope body. It was equipped with a fast piezo stage for axial sample positioning. Three-dimensional spatial information was encoded in the shape of the point spread function by astigmatic detection and retrieved by real-time image analysis code developed for this purpose. A novel localization metric based on cross-correlation template matching was devised to enable tracking based on a low number of photons detected per particle. During post-processing, relative axial localizations determined from the image data were combined with the piezo stage position to obtain full three-dimensional particle trajectories.

Mechanical and optical properties of the setup were thoroughly characterized using appropriate test samples. A temporal resolution down to 1,12 ms was achieved. The localization precision of the method was experimentally determined by repeated imaging of immobilized fluorescent beads. The capability to track single emitters was validated in a biochemical model system. Lipids labeled with a synthetic dye molecule were incorporated in the bilayer membrane of giant unilamellar vesicles and tracked on their spherical surface. Trajectories of more than 20 s duration could be obtained at as little as 130 photons detected per frame. An analysis of the photophysical properties revealed that observation times per particle were limited not by failure of the tracking algorithm but by photobleaching.

Applicability of the method in biological specimen was proved by tracking fluorescent nanoparticles micro-injected into *C. tentans* salivary gland cell nuclei for more than 270 s in several thousand frames.

Subsequently, the method was applied to track mRNA and rRNA particles in *C. tentans* salivary gland cell nuclei. Biomolecules were specifically labeled by complementary oligonucleotides carrying up to three synthetic dye molecules. It was

possible to routinely acquire trajectories of particles with a diffusion coefficient of D = 1-2 µm^2/s spanning $\geq$ 4 s and 4-5 µm in axial direction. The longest trajectories lasted more than 16 s and covered 10 µm axially. Both, observation time and axial range, were increased by more than one order of magnitude as compared to standard 2D tracking experiments. It was thus possible to investigate mobility states not on the basis of an ensemble of short observations but for individual particles.

Contents

1 Introduction

1.1 Motivation and aim of the thesis

Fluorescence microscopy is a versatile tool for biological research. It allows the observation of living cells with minimal perturbation of the specimen. Highly specific contrast can be achieved by genetic modification of the specimen, anti-body based immunostaining, or a number of other labeling strategies. The advent of sensitive detectors and sophisticated imaging schemes, which drastically reduce background noise, enabled the first observations of single fluorescent molecules in the mid 1990's by near-field scanning optical microscopy [1] and total internal reflection microscopy (TIRF) [2]. While optical imaging is generally limited to a resolution of approximately half the emission wavelength by the laws of diffraction, sparse emitters can be localized with much higher precision [3]. The concept of localization microscopy has gained much attention in recent years. From thousands of single molecule localizations, specimen structures can be reconstructed with a resolution much smaller than the diffraction limit [4]. Early single molecule studies were, however, focused on particle dynamics, e.g. in lipid bilayers [5] and flat membranes of living cells [6]. The preference for membrane-based processes originated from the limited depth of field of the high numerical aperture objectives required for efficient single molecule detection. Particles can also be observed in the 3D volume of a specimen, but typically rapidly leave the axial detection range of ≤ 1 µm. If particle motion is not constrained to a two-dimensional (2D) surface, tracking results obtained from a 2D analysis can be misleading. This is already the case if a membrane is not flat but has a more complex, uneven topology [7]. Similarly, 2D data do not accurately represent three-dimensional (3D) particle motion if the specimen structure is not isotropic [8]. What seems like confined motion in 2D may actually be free diffusion in a trajectory leading out of the image plane.
One example for a cellular process which can hardly be captured in its entirety with classical 2D single particle tracking (SPT) is the transport of genetic information from its storage place on deoxyribonucleic acid (DNA) strands inside the cell nucleus to the cytoplasm, where it is translated to proteins. In a first step, messenger ribonucleic acid (mRNA) particles (mRNPs) containing a transcript of the information are fabricated at the gene locus. They travel through the nucleoplasm to reach pores in the nuclear envelope, undergo an export procedure to pass through the pores, and finally reach the cytoplasm where translation is initiated. Tracking of individual mRNA particles can reveal details of the trafficking process involved in regulating the dynamics of the mRNA life cycle. Limited observation times allow only short glimpses at the fate of individual particles. Conclusions on particle mobility [9] or export kinetics [10] are thus usually drawn from large ensembles of short single particle trajectories [11]. Ultimately however, the goal would be to follow a individual particles during their entire lifetime from the transcription site through the pre-processing and export steps to translation in the cytoplasm.

It has previously been demonstrated that single molecules can be detected dozens of microns deep inside large, semi-transparent specimen by light sheet fluorescence microscopy (LSFM) [12, 13]. The optical sectioning effect introduced by illuminating the focal plane orthogonal to the detection axis results in a reduced background intensity and increased image contrast. By inserting a weak cylindrical lens in front of the detector, 3D spatial information can be encoded in the shape of the point spread function (PSF) representing the image of a sub-diffraction-sized particle [14]. While 3D localization approaches have previously been used in conjunction with a feedback loop for active tracking of bright particles [15–17], none of them achieved the sensitivity required for tracking fluorescently labeled biomolecules, which yield only a small number of photons per frame.
In this work, a microscope capable of localizing single fluorescently labeled particles in 3D and actively following their course through the specimen was developed. A feedback loop for real-time SPT employing a novel localization scheme was developed to enable 3D localization at low photon counts and extend the realm of feedback tracking to a range much more relevant for biological and biomedical research.
In analogy to the very first single molecule tracking experiments, the method was tested by following particles in lipid bilayers. Instead of flat 2D membranes, the spherical surface of giant unilamellar vesicles (GUV) provided a suitable 3D model system. Fluorescently labeled lipids can easily be incorporated in the membrane in virtually arbitrary concentrations during vesicle preparation and their mobility controlled by means of the membrane composition.
Further, the instrument was used to track mRNPs in salivary gland cell nuclei of *Chironomus tentans* (*C. tentans*) larvae. Trafficking of these particles has previously been studied in this laboratory [9, 18] and revealed discontinuous motion in areas of the nucleoplasm devoid of chromatin. It is still not known how exactly mRNP trafficking is mediated in the nucleoplasm [10, 19]. Due to their high mobility and the limited depth of focus (≤ 1 µm), previous observations of individual mRNPs hardly exceed 0,2 s (compare e.g. Fig. S4 in [9]). Following them in a feedback loop and thus extending the observation time for single particles may help to uncover a larger part of the mRNP life-cycle in individual observations and thus allow for a more detailed analysis of mRNA trafficking dynamics.

Two students have been involved in parts of this work. Ana Lina Meskes wrote her thesis (Diploma in Chemistry, 2011, [20]) on *Mikroskopie mit Hochauflösung in drei Dimensionen*[1] and used the setup as well as an early version of the particle tracking algorithm presented in sec. 3.2.1 to obtain 3D superresolution images with the dSTORM approach under my guidance [21].
Similarly, Florian Kotzur wrote his thesis (Master of Science in Chemistry, 2012,

[1] *Microscopy with superresolution in three dimensions*

[22]) on *3D-Lokalisierung von Nanopartikeln und einzelnen Molekülen auf freistehenden Modellmembranen*[2] and used the instrument to track strepavidin-coated beads on the surface of GUVs. He was involved in early attempts to track lipids carrying a single emitter.
None of their work or results were used in this thesis.

1.2 Outline

The following sections of this chapter contain a brief introduction to fluorescence microscopy techniques (sec. 1.3) and light sheet microscopy in particular (sec. 1.3.4). The concept of the point spread function (PSF, sec. 1.5) and its implications for resolution and single particle localization are introduced. Single particle tracking and approaches towards 3D SPT are outlined in sec. 1.7. Giant unilamellar vesicles (sec. 1.8) and *C. tentans* salivary gland cells (sec. 1.9) were used as biochemical and biological model systems respectively to demonstrate the scope of the method developed in this work.
Materials are documented in appendix A and methods outlined in chapter 2.
Chapter 3 contains a detailed description of the light sheet microscope assembled for the measurements presented throughout this work. Further, the 3D localization algorithms developed for real-time particle tracking are explained (sec. 3.2) and the instrument characterized using various test samples (sec. 3.4).
The method was applied to track lipids carrying single fluorescent dyes in GUVs of various composition (sec. 4.1). Further, ribosomal RNA (rRNA) (sec. 4.2.3) as well as mRNA (sec. 4.2.4) particles were tracked in *C. tentans* salivary gland cell nuclei and their mobility analyzed on a single particle basis. Acquisition parameters for each experiment are stated in the respective chapters and summarized in Tab. C.1 in the appendix.
The implementation of astigmatic 3D SPT in a light sheet microscope and the results obtained with the setup are discussed in chapter 5.

[2] *3D localization of nanoparticles and single molecules in free-standing model membranes*

1.3 Microscopy

While the first microscopes were already described hundreds of years ago, a number of technical developments in the 20th century boosted their usability in the life sciences. Namely, fluorescence staining (already discovered in the 19th century), the invention of confocal microscopy [23, 24], utilization of lasers for illumination [25, 26] and the discovery of fluorescent proteins [27] presented important milestones in the last decades.
Electron microscopy provides a higher resolution than optical light microscopy due to the much smaller de Broglie-wavelength of electrons but cannot be used to observe life specimen. Optical microscopy on the other hand is a minimally invasive technique applicable to a large range of samples from a few dozen nanometers [4] up to several millimeters [28] in size and providing a temporal resolution down to milliseconds on the one hand [29] and observation periods of several days [30] on the other hand.
Contrast in optical microscopy can be achieved by any detectable modification of the state of a probing optical wave (e.g. intensity, wavelength, phase, polarization). Fluorescence microscopy utilizes the properties of fluorescent molecules to generate contrast by absorption of photons of a specific wavelength and emission of photons of a higher wavelength. High specificity is achieved by selective labeling strategies allowing fluorescent molecules to bind only to desired target structures, by genetic modification leading to co-expression of fluorescent proteins attached to the proteins of interest or by changing the emission properties of molecules based upon the nature of their immediate environment (e.g. Ca^{2+} concentration, pH value, etc.).

1.3.1 Epifluorescence microscopy

The basic components of any fluorescence microscope are (Fig. 1.1)

- an illumination source (I),
- a filter cube containing a dichroic mirror and optical filters (C),
- an illumination and detection objective (O),
- a tube lens (T),
- and a fluorescence detector (D).

If a white light source is used for excitation, an excitation filter can be employed to select a certain wavelength band and specifically excite fluorophores at the maximum of their absorption spectrum. In a typical configuration, the excitation light

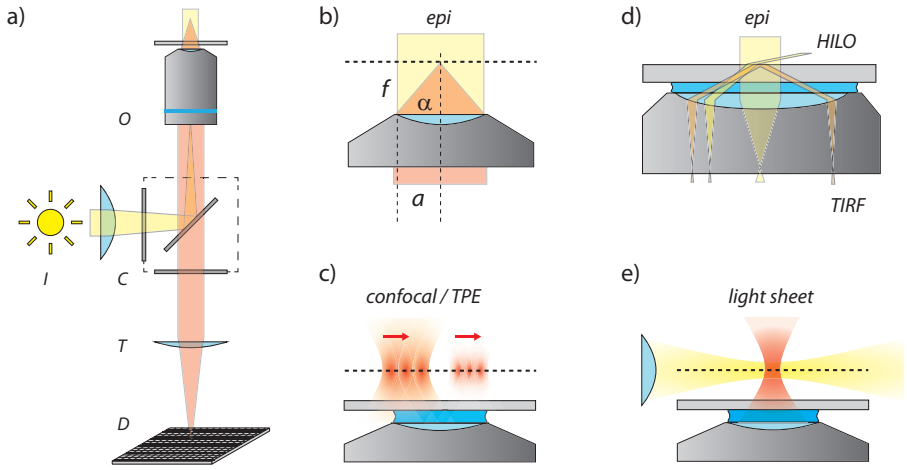

Fig. 1.1: **a)** Basic epifluorescence microscopy setup with illumination (yellow) and detection (orange) beam path. **b)** Fluorescence emitted in the focus can be collected under the aperture angle 2α. **c)** Schematic representation of the system PSF in confocal and two photon microscopy. Sectioning is achieved by background rejection or non-linear excitation with a point-scanned focus. **d)** In HILO and TIRF microscopy, the entire image field is illuminated at once, allowing for higher frame rates. **e)** Light sheet microscopy achieves optical sectioning by selective illumination of the focal plane orthogonal to the direction of detection. See Fig. 1.6 for a detailed representation of PSF contours.

is guided onto the illumination objective by a dichroic mirror which reflects light below and transmits light above a certain cutoff wavelength. Fluorescence is excited in the sample within an illumination light cone (Fig. 1.1 b)). A fraction of it is collected by the detection objective. The detection efficiency is characterized by the numerical aperture $\mathrm{NA} = n \cdot \sin\alpha$ of the objective where n designates the refractive index of the medium on the side of the objective facing the specimen and α the semi aperture angle under which the objective can collect light emitted at the focus. In epifluorescence microscopy, the detection objective is identical with the illumination objective. Typically, the fluorescence intensity is up to 10^6 times lower than the excitation intensity. Additional emission filters after the dichroic mirror can be used to further suppress any remaining, back-scattered excitation light. The tube lens focuses the fluorescence onto a (pixel-array) fluorescence detector. Due to fundamental laws of optics only light from the focal plane contributes to a sharp image on the detector. The depth of field depends on the emission wavelength and the NA of the detection objective. Fluorescence originating from outside the focal plane deteriorates the image by adding a blurry photon background and thus reducing contrast and signal-to-noise ratio (SNR). Under certain conditions, computational methods can be used to restore the in-focus information mathematically by deconvolution of the image data with the PSF [31].

1.3.2 Confocal and two-photon microscopy

Instead of illuminating and imaging the entire image plane at once, the image information is acquired sequentially and restored computationally in confocal microscopy. Classical confocal microscopy is a point-scanning technique. The basic building units are similar to those of an epifluorescence microscope. Scanning mirrors are used to sweep an excitation point focus across the focal plane. As in epifluorescence illumination, fluorescence is therefore excited throughout the entire specimen. However, out-of-focus signal is prevented from reaching the detector by inserting a confocal pinhole in the image plane of the tube lens and placing the detector behind it. Only light originating from the focal plane is focused exactly onto the pinhole and can thus pass the small aperture. Fluorescence emitted above or below the focal plane is focused in front of or behind the aperture and thus effectively prevented from reaching the detector. The same is true for fluorescence emission scattered on the way to the detector. The overall system PSF is essentially the product of excitation and detection PSF. Generally, sidelobes of the system PSF and especially its axial extent are strongly reduced in confocal microscopy. It can therefore be used for sectioned imaging of an extended specimen and reconstruction of high resolution 3D datasets. Axial resolution is determined by the numerical aperture of the objective used for illumination and detection.
To speed up the acquisition process, variants using line-scanning procedures or multiple confocal volumes have been developed. In line-scanning confocal microscopy, the pinhole is replaced by a slit aperture and fluorescence detected by a linear detector array. Spinning disc confocal microscopy employs a rotating disc with a number of pinholes to rapidly sweep multiple foci across the object field while detecting fluorescence through the same pinholes with a camera.
A similar reduction of the system PSF can be achieved by two-photon-excitation (TPE). TPE is a non-linear process, in which the energy for a fluorescence excitation process is delivered not by one but two photons, each of them carrying only a fraction of the required energy. Its probability scales with the square of the excitation power density. Therefore, the excitation PSF roughly corresponds to the square of the single photon point-scanning PSF of the respective wavelength. Its central maximum is accentuated with respect to the sidelobes, rendering a confocal detection pinhole unnecessary. Unlike in confocal microscopy, fluorescence photons scattered on the way to the detector are not blocked but can contribute to the image information [32]. One drawback of TPE microscopy is the high excitation power density, which needs to be achieved to evoke a satisfying signal strength. Small deteriorations of the PSF can have a severe impact on the local power density and thus severely reduce the two-photon excitation capability.

1.3.3 HILO and TIRF microscopy

Background reduction in widefield microscopy can also be achieved by changing the illumination scheme in order to reduce fluorescence excitation in out-of-focus regions instead of suppressing detection from these regions. Illuminating the specimen with a beam offset radially from the center of the objective (Fig. 1.1 d)) leads to a tilted beam in object space [33]. If a high NA objective is used and the beam displaced towards the outer edge of the objective aperture, it intersects with the focal plane of the instrument at a very flat angle. Thus, an optical sectioning effect is achieved. However, this approach, termed HILO (highly inclined laminated optical sheet microscopy), works only in a limited depth range and in the center of the object field. At the edges of the object field, the inclined beam illuminates sections below and above the focal plane respectively, resulting in image blur and loss of contrast. In TIRF, the illumination beam is displaced even further towards the edge of the objective aperture. The inclination angle is raised above the critical angle for total internal reflection at the interface between the coverslip and the buffer or sample above it [34]. Although light is reflected back from the interface, an evanescent wave extends into the medium above the interface. Its field strength decays exponentially on a length scale of a few dozen nanometers. Thus, TIRF can be used to limit fluorescence excitation to parts of the specimen in close proximity to the coverslip surface, e.g. the basal membrane of adherent cells.

1.3.4 Light sheet fluorescence microscopy

In light sheet fluorescence microscopy (LSFM), the illumination and detection light path are separated geometrically. Optical sectioning is achieved by illuminating the specimen from the side with a thin sheet of light. While sectioning is usually not as efficient as in confocal microscopy, LSFM has the major advantage of being extremely efficient on the photon budget. In contrast to confocal microscopy, out-of-focus fluorescence does not need to be prevented from reaching the detector since it is not even excited in these regions of the specimen. Additionally, fast cameras with high quantum efficiency can be used to detect fluorescence at rates of hundreds of frames per second. Imaging speed is increased by orders of magnitude as compared to point-scanning techniques due to the parallelized detection [35].
The concept of light sheet illumination was originally introduced more than a century ago by Siedentopf and Zsigmondy as *ultramicroscopy* [36]. They used their instrument to estimate the size of gold particles in ruby glass by the properties of light scattered off the particles. 90 years later, the technique was rediscovered for fluorescence microscopy by Voie et al. [37] and later Huisken et al. [38]. It proved to be a very effective tool in the hands of developmental biologists and is especially suited for investigations in large, semi-transparent specimen like zebrafish [35], fruit

fly embryos [38] or chemically cleared tissue [39].
Biological research using LSFM still goes hand in hand with technical development of the method. Early light sheet microscopes generated the illumination sheet by simply focusing an expanded, collimated laser beam into the specimen with a cylindrical lens [37, 38]. Shaping the beam in the excitation path enables replacing the cylindrical lens by an illumination objective. Objectives are usually much better corrected for a number of optical aberrations, resulting in a higher quality of the light sheet [40].
A scanning mirror in a conjugated plane can be used to rapidly pivot the illumination sheet within the focal plane during the detector integration time and thus reduce shadowing artifacts [41]. An alternative illumination concept was introduced by Keller et al. as digitally scanned light sheet microscopy (DSLM). In this approach, a homogeneous illumination intensity across the object field is achieved by rapidly scanning a focused laser beam across the focal plane [35]. In further developments, the approach was extended to two-sided illumination and detection [42, 43], two-photon excitation [44], and illumination with self-propagating Bessel beams [45].
Due to the unusual illumination path, sample mounting in LSFM is more complex than in standard microscopes. Large specimen like developing zebrafish or fruit fly embryos are often embedded in a low concentration agarose cylinder and placed in a small aquarium completely filled with buffer [46]. In this most common case, which has also been implemented in one of the first commercially available light sheet microscopes (Zeiss Light Sheet Z1), water-dipping objectives are used for illumination and detection [41, 47, 48].
In other configurations, an angle of up to 45° was introduced between the cover slide and both, the illumination and the detection objective [49, 50], or between a coverslip and the objectives [51] to adapt the technique for the observation of adherent cells. Alternatively, the light sheet can be reflected off an atomic force microscopy cantilever positioned next to the cell of interest [52]. The various implementations of light sheet illumination are reviewed in [53].
LSFM can be beneficial not only for imaging of large specimen but also for single molecule microscopy. The signal-to-noise ratio (SNR) and contrast ratio for single particle signals can be drastically improved by the intrinsic optical sectioning effect [40]. At the same time, sensitive high speed cameras enable fluorescence detection at frame rates of several hundred hertz. Single molecule LSFM has been used for both, single particle tracking [12, 13, 51, 52] and 3D superresolution imaging [20, 54, 55].

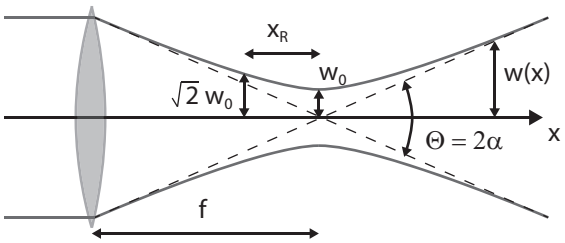

Fig. 1.2: Schematic representation of a Gaussian beam focus. Grey lines indicate the $1/e^2$-radius of the beam with a minimum waist w_0 and a divergence angle Θ. At a distance x_R from the focus, the beam radius is increased by a factor $\sqrt{2}$.

Light sheet geometry

Usually, the TEM_{00} mode of a continuous wave laser, representing a monochromatic Gaussian beam, is focused into the specimen to generate the light sheet. A Gaussian beam with a radial intensity profile $I(r) = I_0 \cdot e^{-r^2/2w^2}$ has a minimum waist w_0 usually characterized by the $1/e^2$-radius at which the intensity drops to a value of $I(w_0) = I_0/e^2$, where I_0 denotes the amplitude in the center of the beam (Fig. 1.2). The beam diverges along the optical axis x according to

$$w(x) = w_0 \cdot \sqrt{1 + \left(\frac{\lambda x}{\pi w_0^2}\right)^2} = w_0 \cdot \sqrt{1 + \left(\frac{x}{x_R}\right)^2} \tag{1.1}$$

where λ denotes the wavelength of the laser beam. A measure for the divergence of the beam is the Rayleigh length

$$x_R = \frac{\pi w_0^2}{\lambda} \tag{1.2}$$

at which $w(x_R) = \sqrt{2} w_0$ or the cross-section of the beam doubles. In practice, this relation dictates that a small waist w_0 results in a short Rayleigh length or a strong divergence of the beam. For $x >> w_0$, the angle of divergence $\Theta \to 2\lambda/(\pi w_0)$. A beam focused by a high numerical aperture $NA = n \cdot \sin\alpha$ results in a small beam waist or a thin focus since $\Theta = 2\alpha$ and $w_0 = \lambda \Big/ \left(\pi \operatorname{asin}\left(\frac{NA}{n}\right)\right)$. Thus, the minimum beam waist w_0 corresponding to the light sheet thickness in the illumination focus is determined by the effective numerical aperture or the height of the beam incident on the illumination objective.

1.4 Fluorescence

Fluorescence labeling presents a powerful tool to generate image contrast in fluorescence microscopy. Laser illumination is used to excite fluorescent molecules specifically attached to structures in the specimen under investigation. The availability of genetically modified fluorescent proteins [27] but also a plethora of other fluorescence labeling techniques enable the direct visualization of cellular components and the investigation of their behavior.

1.4.1 The Jablonski diagram

An extensive description of fluorescence phenomena can be found in [56], which shall be briefly summarized in the following paragraphs.
Fluorescence is light irradiation as a result of an electronic de-excitation process to a state of lower energy. For it to occur, the energy needs to be delivered to the system in the first place. This can be achieved by the converse process of photon absorption. Upon absorption of a photon with energy $E = h\nu = hc/\lambda$, the electron transitions from the singlet ground state S_0 to the excited state S_1 (Fig. 1.3). Typical energies required for this transition are on the order of 1 - 3 eV, corresponding to a wavelength of $\lambda = 412$ - 1240 nm (visible to near infrared).

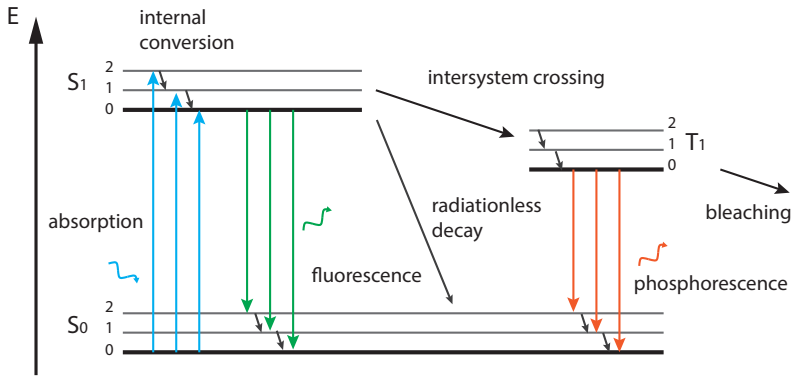

Fig. 1.3: Jablonski diagram. Photon absorption leads to excitation from S_0 to a vibrational level (0,1,2,...) of S_1. Vibrational levels are depopulated via *internal conversion*. Fluorescence can be emitted upon de-excitation from S_1 to S_0. The transition between singlet (S_0, S_1) and triplet states (T_1) has a much lower but still finite probability and can lead to phosphorescence emission upon the $T_1 \rightarrow S_0$ transition. Adapted from [56].

The electronic states are superimposed with vibrational and rotational states of lower energy separation. At room temperature, virtually only the lowest vibrational state of the electronic ground state is populated due to thermal excitation.

Nevertheless, the excitation by photon absorption can occur to any of the vibrational states of S_1 provided that the quantum mechanical wave functions of both states overlap (Franck-Condon principle). The multitude of possible transitions from S_0 to S_1 and additional thermal broadening result in the possibility to excite the fluorescent molecule not just by photons of a single wavelength but by a broad excitation spectrum (Fig. 1.4). Its amplitude corresponds to the efficiency of the excitation process at a specific wavelength, the *extinction coefficient* $\epsilon(\lambda)$ (sec. 1.4.2). Similarly, an emission spectrum results from the various $S_1 \rightarrow S_0$ transitions. Since the vibrational levels usually have a similar separation in both states, the emission spectrum often resembles a mirror image of the excitation spectrum. The exact energy levels and thus the shape of the spectra can depend on a number of factors like binding states of the fluorescent molecule, the solvent medium or e.g. the pH value of the surrounding medium.

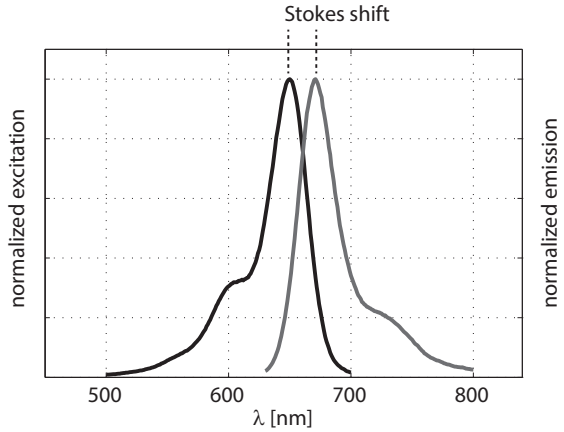

Fig. 1.4: Excitation (black) and emission (grey) spectrum of the synthetic dye AlexaFluor647. The shift between excitation and emission maximum is designated as Stokes shift.

Light absorption occurs on timescales of 10^{-15} s. Once in the excited electronic state, electrons quickly decay to the lowest vibrational state of S_1 through *internal conversion* within 10^{-12} s. Since fluorescence emission and other decay pathways from the S_1 state are stochastic processes with time constants of 10^{-9} s or more, they virtually occur after internal conversion. The energy lost during this cycle leads to emission of photons with a longer wavelength as compared to the excitation wavelength, a phenomenon known as Stokes shift. It enables the use of spectral filters to separate fluorescence emission from excitation light (Fig. 1.1 a)).
Transitions to the triplet state T_1 (*inter system crossing*) require a spin-flip. They are termed *forbidden*, but do occur with low probability on time scales of 10^{-6} s or longer. The radiative transition from T_1 to S_0 is known as phosphorescence emission.

1.4.2 Photon yield

One of the most important questions in single molecule microscopy is, how many photons one can detect from a single fluorophore and at which rate. Since all processes involved in the fluorescence cycle are of stochastic nature, this question can only be answered in terms of an ensemble average.
The molar extinction coefficient of a fluorescent dye $\epsilon(\lambda)$ ($[\epsilon] = \mathrm{L} \cdot \mathrm{mol}^{-1} \cdot \mathrm{cm}^{-1}$) quantifies how strong a substance absorbs light of a specific wavelength. It is thus directly related to the absorption cross section. However, even for an infinitely high excitation power density, the finite rate constants of the individual steps of the fluorescence cycle limit the photon emission rate. Since both, absorption and internal conversion, occur on timescales orders of magnitude shorter than the fluorescence decay, it is the latter which is rate limiting. Similar to radioactive decay, fluorescence emission is a stochastic process which can in the most simple case be described by a single exponential decay curve $e^{-k_F t}$ with a time constant $\tau_F = 1/k_F$ called the natural lifetime. A typical value of $\tau_F = 5 \cdot 10^{-9} s$ results in a maximum possible photon emission rate of $k_F = 2 \cdot 10^8/s$. Alternative de-excitation pathways reduce this value. Apart from fluorescence emission, the energy can be dissipated radiationless by a number of processes, including resonant energy transfer to a neighboring molecule or collisions with other molecules, which are generally summarized in a rate constant k_{rl}. *Intersystem crossing* to the triplet state T_1 also leads to depopulation of the S_1 state with a rate constant k_{ISC}.
The quantum yield of a fluorophore, $QY = k_F/\Sigma k$, describes how many fluorescence photons result from a number of absorbed photons. Together with the extinction coefficient it determines the brightness $\epsilon \cdot QY$ of a fluorescent molecule. Transitions to long-lived, non-fluorescent states other than the triplet state can lead to *off*-times of the fluorophore, a phenomenon known as *blinking* [57]. Ultimately, the total number of photons emitted by a single fluorophore, $\bar{N}$, is limited by *photobleaching*, the irreversible destruction of the fluorophore. While this process is still not fully understood, reactive oxygen species seem to play a fundamental role in photobleaching. It can be avoided to a large extent by use of specific buffers, which, however, are usually not compatible with live cell experiments [57].
Typical values for the total number of photons emitted before bleaching range from $\bar{N} = 10^5$ for fluorescent proteins [58] to $\bar{N} = 10^6 - 10^7$ for organic dyes respectively [57, 59]. The photon emission rate on the other hand is limited by the fluorescence lifetime and on the order of $10^8\ \mathrm{s}^{-1}$. One must further bear in mind the limited detection capability of optical microscopes. Typically, less than 10% of the emitted photons are finally registered by the detector (sec. 3.1.4).

1.4.3 Fluorophores

A variety of markers are used for fluorescence microscopy. As described above, key aspects for single molecule observation are photon yield, dye stability, a constant photon flux and, especially in biological applications, functionalization and toxicity of the label.
Fluorescent proteins can be genetically encoded and thus provide highly specific stainings of molecular targets. For single molecule observation, their limited photon yield before bleaching is the biggest problem. Typically, some 10^3 photons can be detected from each protein [58], sufficient for at best a few dozen observations of each molecule.
Organic dyes are smaller in size and available with a much higher photon yield than fluorescent proteins. On the downside they require sophisticated labeling strategies to achieve specific stainings, e.g. by genetically encoding a binding motif in the target molecule. Another possibility is to purify the target molecule, label it *in vitro* and redeliver it to the specimen e.g. by microinjection.
Other markers like semiconductor quantum dots [60], nanodiamonds [61] or single walled carbon nano tubes [62] can yield a virtually unlimited number of photons but are not widely used in biological research due to various difficulties ranging from transitions to dark, non-fluorescent states to toxic effects in live cells.

1.5 The point spread function

All fluorescent molecules are much smaller than the wavelength of the light they emit and can be regarded as point-like emitters in a first approximation. The PSF of an optical system describes, how a monochromatic wave of wavelength λ emitted from such a source is transformed by an optical system or, in other words, what the image of a fluorescent molecule looks like. The derivations summarized here follow closely the concise description by Born and Wolf [63]. A complete formulation as devised by Debye considers the amplitude of the electric field oscillations

$$h(x,y,z) = |h(x,y,z)| \cdot e^{i\phi(x,y,z)} \tag{1.3}$$

including its phase information $\phi(x,y,z)$, to determine the intensity distribution of the electric field,

$$I(x,y,z) = |h(x,y,z)|^2 \tag{1.4}$$

In the particle model of light, single photons emitted from $P(x_0,y_0,z_0)$ will hit a detector positioned at z_{det} with a probability proportional to $I(x,y,z_{det})$. According to Debye's formulation, the amplitude of a spherical wave converging from a circular aperture with radius a to a focal point at a distance f from the aperture along the optical axis can be described by

$$U(u,v) = -\frac{2\pi i a^2 A}{\lambda f^2} \cdot e^{i(f/a)^2} \int_0^1 J_0(v\rho) \cdot e^{-iu\rho/2} \rho d\rho \tag{1.5}$$

where A an arbitrary amplitude, (u,v) optical coordinates

$$u = \frac{2\pi}{\lambda}\left(\frac{a}{f}\right)^2 z \tag{1.6}$$

$$v = \frac{2\pi}{\lambda}\left(\frac{a}{f}\right)\sqrt{x^2+y^2} \tag{1.7}$$

and J_n the n-th order Bessel function. Using the Lommel function

$$U_n(u,v) = \textstyle\sum_{s=0}^{\inf} (-1)^s \left(\frac{u}{v}\right)^{n+2s} J_{n+2s}(v) \tag{1.8}$$

the intensity close to the focus and thus the intensity point spread function can be expressed as

$$I(u,v) = \left(\frac{2}{u}\right)^2 \left[U_1^2(u,v) + U_2^2(u,v)\right] I_0 \tag{1.9}$$

where the intensity in focus

$$I_0 = \left(\frac{\pi a^2 |A|}{\lambda f^2}\right)^2 \tag{1.10}$$

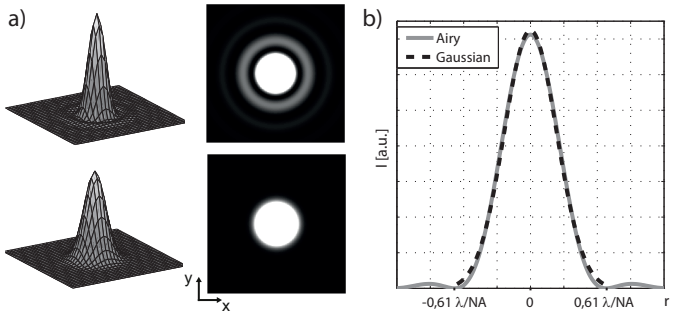

Fig. 1.5: Comparison of Airy and Gaussian PSF model. Parameters: NA = 1,15, λ = 640 nm. **a)** Intensity distribution in the focal plane according to eq. 1.11 and least squares approximation of a 2D Gaussian peak according to eq. 1.13. Sidelobes are present in the Airy model, but not in the Gaussian approximation. **b)** Intensity profile through the center of the Airy disk (grey solid) and Gaussian fit (black dashed).

In the focal plane, $u = 0$ and eq. 1.9 simplifies to

$$I(0, v) = I_0 \left(\frac{2J_1(v)}{v} \right)^2 \tag{1.11}$$

also known as the Airy formula. Its intensity distribution corresponds to a central peak, the so called Airy disk, surrounded by symmetric sidelobes, the Airy rings (Fig. 1.5 a)). The first minimum of eq. 1.11 occurs at a radial distance of

$$r = \sqrt{x^2 + y^2} = 0{,}61 \frac{f}{a} \lambda = 0{,}61 \frac{\lambda}{NA} \tag{1.12}$$

A very common simplification approximates the intensity distribution of the Airy disk by a 2D Gaussian peak (Fig. 1.5)

$$I(v) = I_0 \cdot e^{-\frac{(v-\mu)^2}{2w^2}} \tag{1.13}$$

or, in Cartesian coordinates,

$$I(x, y) = I_0 \cdot e^{-\frac{(x-x_c)^2}{2w_x^2} - \frac{(y-y_c)^2}{2w_y^2}} \tag{1.14}$$

with center coordinates (x_c, y_c) and $1/e^2$-radii (w_x, w_y) along the two axes. The Gaussian approximation does not exhibit the characteristic Airy rings but is able to accurately reproduce the center coordinates as well as the spread of the central Airy disk (Fig. 1.5 b)). In fact, the center position can be determined with an accuracy much smaller than the width of the diffraction limited intensity distribution. This is used in single particle localization to obtain highly accurate estimates of the position of a molecule (sec. 1.7.1). The Gaussian model is sufficient in most single

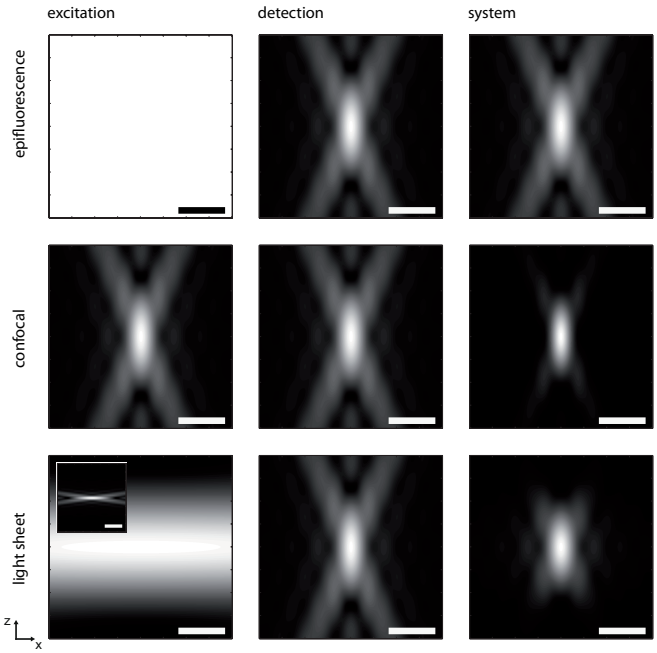

Fig. 1.6: Comparison of excitation, detection and system PSF contours for common microscopy techniques. In confocal and light sheet microscopy, the system PSF is axially confined. All PSFs were calculated from eq. 1.9 using NA = 1,15; $NA_{LightSheet}$ = 0,3; λ = 640 nm; n = 1,333 (water); grid size 5 nm. Scale bar 1 µm, inset scale bar 10 µm.

molecule imaging experiments since the amplitude of the Airy sidelobes is small in comparison to the central peak and does usually not exceed the background noise level [64].
Away from the focal plane the diameter of the Airy disk and the Airy rings increases symmetrically in negative and positive direction.
The intensity distribution along the optical axis ($v = 0$) can be described by

$$I(u,0) = \left(\frac{\sin u/4}{u/4}\right)^2 I_0 \tag{1.15}$$

with the depth of field of the imaging system determined by the first minima occurring at

$$z = \pm\frac{1}{2} f^2 \lambda / a^2 = \pm\frac{1}{2}\frac{\lambda}{NA^2} \tag{1.16}$$

Fig. 1.6 shows PSF intensity contours numerically calculated with 5 nm grid size and typical parameters according to eq. 1.9. The lateral (eq. 1.11) and axial (eq. 1.15) intensity profiles can be found along horizontal and vertical cuts through the profiles respectively.

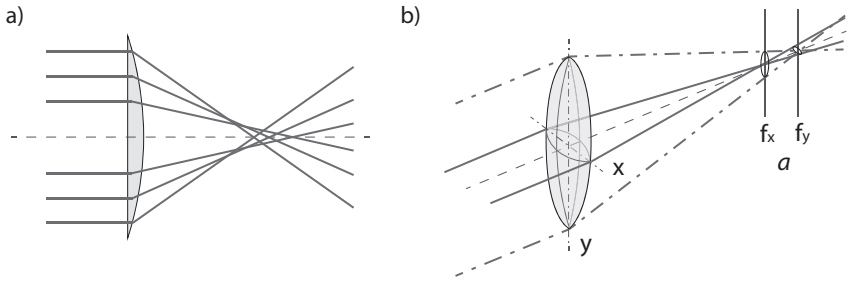

Fig. 1.7: Optical aberrations. **a)** Spherical aberration arises if the refractive power of a lens changes with the distance from the optical axis (dashed). **b)** Astigmatism is caused by different refractive powers for paraxial beams in the x- and y-plane.

The equations presented here account for the special case of a point source emitting monochromatic light registered by an ideal detection system. In real measurements, a number of further aspects need to be considered.
Firstly, the concept of the PSF has to be expanded from describing only the detection signature of the optical system to include the spatial illumination profile of the microscopy technique. As shown in Fig. 1.6, the illumination mode significantly affects the overall system PSF, the product of excitation and detection PSF. Whereas classical epifluorescence excitation ideally has a homogeneous illumination intensity (Fig. 1.6 a)), excitation and detection PSF in point-scanning confocal microscopy (Fig. 1.6 b)) are identical if the Stokes shift between absorption and emission wavelength is neglected. In comparison to the epifluorescence system PSF, sidelobes are suppressed in both, lateral and axial direction. A similar effect results from the orthogonal illumination in light sheet microscopy (Fig. 1.6 c)). However, in this case the PSF size is reduced only in the axial direction.
Secondly, optical aberrations alter the shape of the PSF (Fig. 1.7). Spherical aberration, for example, leads to an axial elongation of the PSF whereas astigmatism results in an elliptical PSF for $u \neq 0$.
Thirdly, fluorescence emission is more realistically characterized by a dipole emitter than by a point source. The emission pattern becomes visible if the fluorophore orientation is fixed with respect to the imaging system over the integration period of the detector. This can be the case for rigidly bound molecules [65]. In most cases, however, rotational mobility will lead to an averaging effect, which effectively lets the emitter appear as a point source to the observer.

1.6 Resolution and localization precision

The resolution of a microscope is determined by the PSF. Since the shape of the PSF can be derived from the laws of diffraction, the resolution is *diffraction-limited* in an ideal system. In this case the spot size for single emitters in the focal plane is given by eq. 1.11. According to the Rayleigh criterion, two point sources can be separated if the distance between the maxima of their diffraction limited images is at least as large as the distance from the peak to the first minimum of the PSF intensity distribution given by eq. 1.12. Other criteria (Abbe, Spatz) result in slightly different formulas but yield similar absolute values of approximately half the wavelength of the emitted light for the resolution of a microscope.
In single molecule imaging it is important to distinguish the resolution from the precision with which the true center position of a diffraction limited spot can be determined. With additional knowledge about the underlying structure, e.g. the number of emitters forming a signal, a localization precision far below the optical resolution can be achieved.
While the resolution is governed by fundamental laws of optics, the localization precision for sparse emitters depends mostly on the number of photons detected from the emitter. With an infinite number of photons, zero localization error could be achieved. In real experiments, the finite number of photons emitted and the Poisson statistics determining their emission pattern lead to shot noise in the photon distribution. Unspecific photon background reduces the SNR and finite detector pixel size, detector noise as well as instrument stability limit localization precision. Thompson et al. [66] derived a formula expressing the 1D lateral localization precision for a Gaussian (eq. 1.13) least squares fit to pixelated data

$$\sigma_x^2 = \frac{w^2 + a^2/12}{N} + \frac{8\pi b^2 w^4}{a^2 N^2} \tag{1.17}$$

where w the width of the PSF, a the image pixel size, N the number of photons contributing to the signal and b the standard deviation of the background noise in units of photons. Mortensen et al. [67] expanded the model and derived the more accurate relationship

$$\sigma_x^2 = F\left(\frac{16\left(w^2 + a^2/12\right)}{9N} + \frac{8\pi b^2\left(w^2 + a^2/12\right)^2}{a^2 N^2}\right) \tag{1.18}$$

where $F = 2$ for electron-multiplying charge-coupled device (EMCCD) cameras and $F = 1$ for scientific complementary metal-oxide-semiconductor (sCMOS) cameras. Deschout et al. [68] presented expressions for the additional broadening of the signal due to particle motion during the detector integration time. For a particle with diffusion coefficient D and integration time Δt, they found

$$w_{eff}^2 = w_0^2 + \frac{1}{3} D \Delta t \tag{1.19}$$

1.7 Single particle tracking

The high localization precision for sparse fluorescence emitters is used in single particle tracking to investigate the mobility of single molecules. It has become an important tool for studying membrane protein interactions but also the nature of the plasma membrane [69] by direct observation of molecular motion. Accuracies in the range of 1 nm have been reported for *in vitro* experiments using sophisticated instrumentation [3]. A variety of related, fluorescence microscopy-based methods have been developed to study molecular mobility in biological specimen. Each of them performs best on specific timescales and poses constraints towards the concentration of fluorescent particles.

Fluorescence recovery after photobleaching (FRAP) uses a strong laser to rapidly bleach fluorescent molecules in a small spot. Fluorescence is restored when unbleached molecules diffuse into the bleached area. If analyzed with an appropriate model, the kinetics of fluorescence recovery yield information on the average mobility of the fluorescent molecules as well as mobile and immobile fractions [70]. Since FRAP reads out the total fluorescence intensity in a certain area, higher concentrations of fluorescent molecules lead to more robust results. At low concentrations, intensity fluctuations may impede the measurements.
In contrast, fluorescence correlation spectroscopy (FCS) can infer particle concentration and mobility from the temporal correlation of fluorescence intensity fluctuations in a small volume. Slowly moving particles reside in the detection volume (system PSF, see chapter 1.5) for a longer time span and thus have a longer correlation time. The detection volume is on the order of 1 femtoliter and a fast detector with a sampling rate of $\geq 10^6$ s^{-1} is required. FCS works best if only a limited number of $1 - 100$ fluorescent molecules is present in the detection volume, corresponding to concentrations in the nanomolar range [71].
Similar to FCS, image correlation microscopy uses the cross-correlation between spatially separated image pixels over time to observe transport phenomena on larger scales [72]. It is, however, restricted to diffraction-limited resolution. To overcome this drawback, particle image correlation spectroscopy (PICS) has been proposed. This approach uses the temporal correlation not between image pixels but between single particle localizations with sub-pixel accuracy to determine the particle mobility [73]. Fluorescent molecules are individually localized as intensity peaks in a series of image frames and their center coordinates determined with nanometer precision. In PICS, mutual distances between particles are evaluated.
Finally, in classical SPT, the particle localizations are connected to trajectories to follow the motion of each individual fluorescent molecule. From the distribution of displacements or *jump distances* in the trajectories, mobility components as well as the type of motion can be inferred (sec. 1.7.5) [74]. The spatial separation between

individual localizations in one frame must exceed the typical jump distance between subsequent frames to avoid particle assignment to the wrong trajectory. Thus, the tolerable particle concentration for SPT depends strongly on their mobility. Far less than one fluorescent molecule may be present per PSF volume to enable localization of each individual particle, i.e. concentrations in the low picomolar range are used.

Similar to FRAP and FCS, SPT has first been applied in biological systems to study molecular mobility in flat membranes [5]. Their geometry simplifies the mathematical models required for FRAP and FCS data analysis as well as the observation of particle trajectories in SPT by confining their motion to a 2D surface. While 3D models have been developed for FRAP [75] and FCS, most SPT studies, even if conducted not on the cell membrane but in the cytoplasm, are still limited to a 2D analysis of the data. However, this simplification can only yield valid results if the particle motion occurs in an isotropic environment. Curvatures or ripples in 2D membranes [7] or anisotropic volumetric structures in the specimen like the cytoskeleton [8] or chromatin channels [76] will inevitably result in artifacts if only the 2D projections of a 3D motion are analyzed.

1.7.1 Single particle localization

To obtain jump distance distributions, particles are tracked by first localizing them and subsequently assigning localizations to trajectories. The process of single particle localization can usually be divided into a first step, in which candidate positions are determined with pixel accuracy and a second step, in which the data are analyzed more thoroughly to filter out valid candidates. Usually, a model function is fitted to the intensity distribution in a small subimage for each candidate to determine a localization with sub-pixel accuracy. Invalid candidates are rejected based on criteria like the intensity peak height or shape [77]. Fluorescence background, motion blur for moving particles, a finite number of detected photons and detector noise limit the localization precision (sec. 1.6).
A straightforward approach for the identification of localization candidates relies on the search for local maxima in the intensity distribution. A pixel is added to the candidate list if it represents a local maximum in the intensity distribution within a neighborhood of a size corresponding to the extent of the PSF. Pixels below a certain threshold are rejected. If the SNR is low, a noise filtering step can be included before identifying candidates. Inhomogeneous background, e.g. due to autofluorescence, can impede the intensity thresholding method. It may be dealt with by calculating a filtered background image, e.g. by applying a median filter to the raw data and subtracting the resulting background image from the raw data.

Instead of using the image intensity to identify candidates, the normalized cross-correlation between the raw image data and either an experimentally acquired or a theoretically calculated PSF image can be determined [78]. The identification and filtering procedure can then be applied to the cross-correlation image without the need for image smoothing or background subtraction (see Fig. 3.7).
A simple method to obtain a sub-pixel localization from the intensity distribution on the chip is calculating its first moment (*center of mass* or centroid). Pixel coordinates are weighted by their respective intensity and an average coordinate is determined. The second moment (variance) of the intensity distribution is a measure for its width. The moment calculations require a thorough background subtraction since any background contribution will lead to a bias of the centroid towards the center of the evaluated subimage on the one hand and increase the variance on the other hand. Calculating the moments is computationally very fast but becomes inaccurate at low SNR [79].
Recently, an approach utilizing the radial symmetry of intensity peaks has been published. For each pixel of the evaluated subimage, the intensity gradient is calculated. The center coordinates of the intensity distribution are determined by finding the position with the minimum distance to all gradient tangents [80]. While this approach is computationally fast, too, it provides no information on peak height or width. The candidate filtering process thus needs to be included in the identification process.
Maximum likelihood estimators (MLE) have been reported to achieve the theoretically optimal localization precision [81]. They iteratively determine the likelihood of a candidate to represent a particle based on not only the shape of the intensity distribution but also noise and background characteristics. An accurate analytical model of the expected intensity distribution is needed for MLE calculation. While MLE calculation has been performed in a highly parallelized manner on a graphics processing unit (GPU) to achieve real-time performance, computation times for single localizations on the central processing unit (CPU) are comparable to those of iterative least squares fitting procedures.
The most common technique for single particle localization is still iterative least squares fitting of a 2D Gaussian peak (eq. 1.14) to the intensity distribution. It provides reasonably high accuracy with low bias and robust performance over a large range of signal intensities [79]. The iterative procedure can be sped up by providing good initial parameter estimates, e.g. from a moment calculation.
Methods to determine localizations of multiple particles with overlapping PSFs exist [82] but shall not be discussed here since particle densities in tracking experiments were usually chosen low enough for individual PSFs to be well separated.

1.7.2 Connecting the dots

Once all particles have been localized, tracking algorithms are used to assign the localizations to trajectories.
If the mutual separation between particles is much larger than the distance a particle travels between subsequent localizations, a simple nearest neighbor approach is sufficient for this purpose [83]. To avoid misassignment of particles to the wrong trajectory, a trajectory usually ends if multiple localizations within the maximum jump distance preclude an unambiguous continuation of the trajectory.
More elaborate solutions exist for cases of higher particle density [84] or cases in which further knowledge about the expected motion pattern is available [85]. Generally, a global cost metric is minimized to find the most likely solution for particle assignments. Aspects like the intensity determined for each localization or the previously observed mobility of a particle can be used to improve the solution.

1.7.3 3D single particle tracking

The same conditions apply if 3D coordinates of the particles are obtained. A number of approaches towards 3D single particle tracking have been suggested. Here, the most relevant ones shall be introduced briefly (Fig. 1.8).
An intuitive way to acquire 3D spatial and temporal information is to record a series of (confocal) image stacks [86]. However, this method does not offer the sensitivity and time resolution to be widely applicable for tracking mobile particles in biological specimen.
Temporal resolution can be improved if the confocal volume is not scanned across the sample to generate classical image information but rather moved in circular orbits around a particle of interest (Fig. 1.8 a)). Any deviation of the particle position from the center of the orbit will lead to intensity fluctuations over the course of one orbital scan, which can be used to infer the particle position. The orbital scanning approach has been combined with simultaneous epifluorescence imaging to relate the particle trajectory to its environment [15].
Similarly, four focal volumes can be positioned with partial overlap to determine the 3D coordinates of a particle situated in between the four foci from the relative intensities detected in each of the channels [17]. This approach has already been used in the 1970's to record the 3D motion of bacteria in a water tank [87] but does also require simultaneous epifluorescence imaging to relate trajectories to their environment (Fig. 1.8 b)).
To a certain extent, 3D spatial information is already encoded in the 2D images of the PSF acquired in SPT experiments. Since the width of the Airy disk increases with the distance from the focal plane, its diameter or the diameter of the Airy

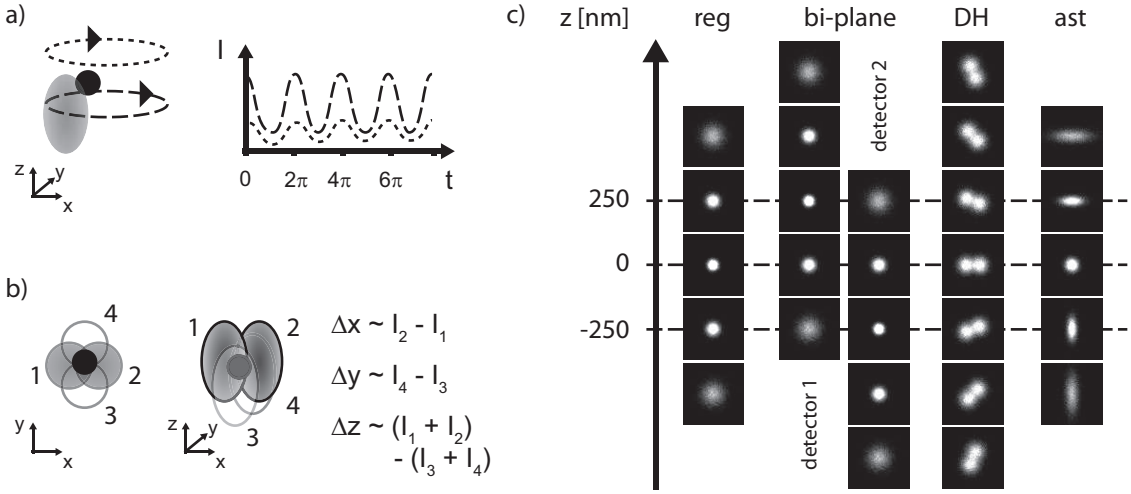

Fig. 1.8: Comparison of 3D localization schemes. **a)** Principle of orbital scanning. Black: Single particle. Grey: Detection volume. Adapted from [15]. **b)** Use of four static detectors for 3D localization. The displacement of the particle from the midpoint between the detectors can be calculated from intensity differences between the respective channels. Adapted from [88]. **c)** PSF engineering approaches break the axial symmetry of the regular PSF (reg) to encode 3D information in the PSF shape. PSFs were reconstructed from values given in [89] (double helix, DH) or [78] (bi-plane and astigmatism, ast) according to eq. 1.13. Specifically, $w_0 = 280$ nm, $w_0^{DH} = 1{,}7 \cdot w_0$, $d_{DH} = 3 \cdot w_0^{DH}$ (point separation for DH-PSF), $\Delta f_{12} = 500$ nm focal plane separation for bi-plane imaging, $\Delta f_{xy} = 500$ nm astigmatism.

rings can be used to infer axial information from a single image of the PSF (Fig. 1.8 c)). Two aspects prevent this fact from being used more widely. Firstly, the symmetry of a perfect PSF renders the axial information contained in it ambiguous. This can be overcome by limiting the accessible volume to one half of the axial space, i.e. by setting the focal plane to the interface between coverslip and sample medium, such that particle localizations can deviate from the focal plane in only one direction [90]. Secondly, the signal level in SPT experiments is often so low that Airy rings are not visible in the image data. Axial localization thus has to rely on the width of the Airy disk alone, which changes only slightly in close proximity to the focal plane [91]. Thus, axial localizations will be very inaccurate compared to their lateral counterparts unless the instrument is used in a defocused configuration at all times. This modality would increase axial precision but reduce signal level and lateral resolution significantly.

The idea of defocused imaging can be improved by simultaneous observation of two or more axially separated focal planes, i.e. by obtaining multiple measurements of eq. 1.9 simultaneously (Fig. 1.8 c)). Comparison of PSF amplitude and width in both image planes yields a unique axial localization. Separate focal planes can be established by increasing the physical path length between tube lens and detector

for one of the images (bifocal imaging, [92]) or by using a sophisticated combination of gratings and prisms to vary the optical path length between different areas on a single detector (multifocal plane microscopy, [93]). Both implementations distribute the photons emitted by a particle onto more than one image plane. Thus, only a fraction of the photons contributes to each of the images. This can partially be cured computationally by recombining the images but requires accurate image registration and transformation [94].
Alternatively, the PSF itself can be engineered to carry more and distinct axial information by altering the phase term $\phi(x, y, z)$ in eq. 1.3. A specific phase mask can be used to generate a PSF with the shape of a double helix [95]. Instead of one central maximum it exhibits two separate peaks of nearly constant intensity over an axial range of up to 2 µm with the angle between the two maxima rotating with axial position. The advantage of this approach is its nearly constant localization precision over the axial detection range. However, the transmission efficiency of the phase element used to shape the PSF is limited, again impeding the use for low photon applications. Further, a separate detection channel is required to acquire undistorted epifluorescence images of the specimen.
Astigmatic imaging (sec. 1.5) can be used for the same purpose of breaking the axial symmetry of eq. 1.9 by modulating the phase of the fluorescence signal. Either a cylindrical lens [14] or a deformable mirror [96] is inserted in the detection beam path to separate the focal planes for beams focused along the $x-$ and $y-$axis and thus create an elliptical PSF. Its major axis changes by 90° when a particle moves from one focal plane to the other. In an effective focal plane between the $x-$ and $y-$focus, the PSF still appears round-shaped but slightly enlarged. The amount of astigmatism and thus the exact shape of the PSF strongly depends upon the position, in which the astigmatic element is placed and on the optical path length difference introduced by it. It also controls the balance between axial and lateral localization precision. Strong astigmatism would enable a very accurate axial localization but impede lateral localization precision.

1.7.4 Particle tracking in a feedback loop

Common to all methods outlined above is the limited axial detection range of 1-2 µm. To observe particles over a larger axial range, either the PSF needs to be extended axially (*extended depth-of-field microscopy*, [97]) discarding most of the axial information, or the focal plane has to be continuously adjusted in a feedback loop to permanently coincide with the particle position.
Such feedback loops are a prerequisite for orbital scanning [15] but have also been implemented in conjunction with four static detectors [17, 88]. In the latter case, the particle under observation is brought back to the focal plane using a fast piezo

translation stage.
Other approaches towards full 3D positional control involve optical tweezers to trap a particle in a certain volume and measure its mobility by evaluating the forces which are needed to keep it in place [98]. Similarly, single fluorophores have been kept in an anti-Brownian electrokinetic trap for several seconds [99]. Regardless of their success in observing particles for a long period of time, trapping methods exert an external force on the particle under observation and thus interfere with its natural behavior.
In contrast, image-based methods maintain the advantage of fluorescence microscopy being a non-invasive method with minimal influence on the specimen. Juette et al. have presented sub-millisecond tracking of fluorescent beads by following a particle with a piezo-mounted objective and a focused laser beam steered by a descanned mirror [16]. Positional information was gained from two areas of 5×5 pixels each on an EMCCD camera, representing two axially separated detection planes. The small image field allowed for a frame rate of ≥ 3 kHz. Even though areas of only $0{,}75 \times 0{,}75$ µm^2 in object space were imaged in this case, it represents a first step towards using real-time image analysis for 3D particle tracking. In the light of ever faster cameras and lab computers it becomes feasible to extract the information needed to control the feedback loop directly from the image data.
In this work, full image frames were read out from the camera and 3D particle localizations relative to the focal plane were encoded in an astigmatic PSF. The information for a single particle was extracted from the PSF shape and used as feedback signal to address the sample stage and keep the particle of interest close to the focal plane.

1.7.5 Diffusion

In SPT experiments, the mobility of individual particles is measured to elucidate the nature of their motion. Pure Brownian (random) motion due to thermal energy in the system results in typical distributions of particle displacements during a given time interval governed by the Maxwell-Boltzmann distribution. Brownian motion of a spherical particle with hydrodynamic radius r in a medium of viscosity η at temperature T can be characterized by a diffusion coefficient

$$D = \frac{k_B T}{6\eta\pi r} \tag{1.20}$$

where k_B is Boltzmann's constant [100]. This relationship is also known as the Stokes-Einstein equation. Without residual drift or directed transport and in large ensembles, the average particle displacement equals zero due to its stochastic nature. Therefore, the mean square displacement (MSD) shall be considered.

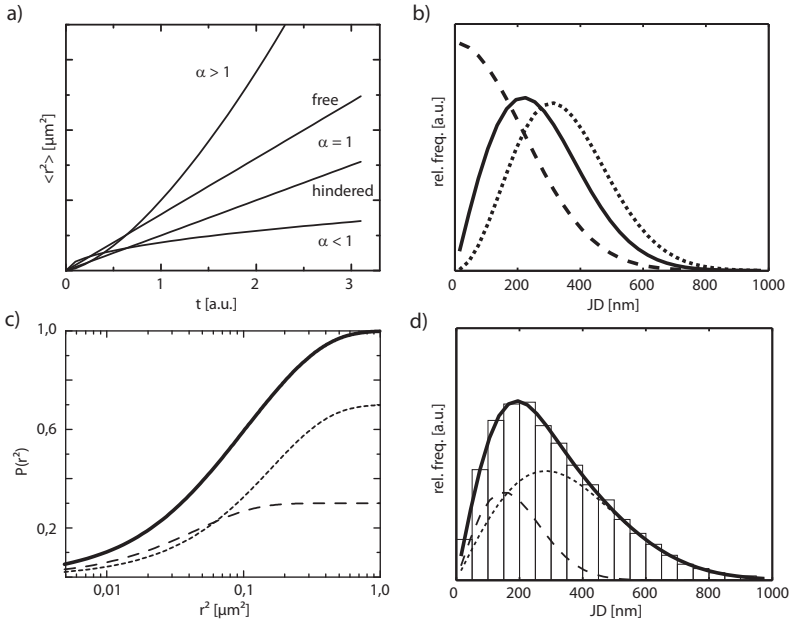

Fig. 1.9: **a)** Characteristic MSD shapes according to eq. 1.25 for (top to bottom) directed flow with $\alpha \geq 1$, free diffusion, hindered diffusion with the same diffusion coefficient and confined motion with $\alpha \leq 1$. **b)** 1D (dashed), 2D (solid) and 3D (dotted) jump distance distribution according to eq. 1.26 - 1.28. **c)** Cumulative distribution of the squared displacement r^2 (eq. 1.31) of a bimodal distribution with components $D_1 = 0{,}7$ µm^2/s, $a_1 = 0{,}3$ (dashed) and $D_2 = 2{,}5$ µm^2/s, $a_1 = 0{,}7$ (dotted). **d)** Bimodal jump distance distribution according to eq. 1.29 (2D, solid). Parameters as in **b)**. $\Delta t = 16$ ms.

In a one dimensional system

$$\left\langle \Delta x^2 \right\rangle = 2D\Delta t \tag{1.21}$$

The mean square displacement is proportional to the time lag Δt with the diffusion coefficient being the proportionality factor. In the case of Brownian motion, orthogonal axes can be treated independently. Therefore

$$\left\langle \Delta x^2 \right\rangle = \left\langle \Delta y^2 \right\rangle = \left\langle \Delta z^2 \right\rangle = 2D\Delta t \tag{1.22}$$

$$\left\langle \Delta r_{xy}^2 \right\rangle = \left\langle \Delta x^2 \right\rangle + \left\langle \Delta y^2 \right\rangle = 4D\Delta t \tag{1.23}$$

$$\left\langle \Delta r_{xyz}^2 \right\rangle = \left\langle \Delta x^2 \right\rangle + \left\langle \Delta y^2 \right\rangle + \left\langle \Delta z^2 \right\rangle = 6D\Delta t \tag{1.24}$$

Thus, the diffusion coefficient can be determined from the slope of a simple linear fit to either $\langle \Delta x^2 \rangle$, $\left\langle \Delta r_{xy}^2 \right\rangle$ or $\left\langle \Delta r_{xyz}^2 \right\rangle$. A more general formulation for the n-dimensional case is

$$\left\langle \Delta r_n^2 \right\rangle = 2n \cdot D\Delta t^\alpha + \sigma_n^2 \tag{1.25}$$

where σ_n denotes an offset due to finite localization precision. An exponent $\alpha = 1$ is characteristic for Brownian motion (Fig. 1.9 a)). For directed flow or transport

in addition to the random thermal motion $\alpha \geq 1$ applies, whereas diffusion confined to a limited area or volume results in $\alpha \leq 1$. Diffusion hindered by obstacles leads to a proportionality factor n lower than the dimensionality of the data [74].
If more than one mobility fraction is present in the data, the distribution of displacements rather than its mean value may yield additional insight. The probability distribution to find a particle initially located at the origin at a radius r after time Δt is (Fig. 1.9 b))

$$p(r = x, \Delta t)\, dx = \frac{2}{\sqrt{4\pi D \Delta t}} \cdot e^{-\frac{xr2}{4D\Delta t}}\, dr \qquad \text{(1D)} \qquad (1.26)$$

$$p(r = r_{xy}, \Delta t)\, dr = \frac{1}{4\pi D \Delta t} \cdot e^{-\frac{r^2}{4D\Delta t}} \cdot 2\pi r\, dr \qquad \text{(2D)} \qquad (1.27)$$

$$p(r = r_{xyz}, \Delta t)\, dr = \frac{1}{\sqrt{4\pi D \Delta t^3}} \cdot e^{-\frac{r^2}{4D\Delta t}} \cdot 4\pi r^2\, dr \qquad \text{(3D)} \qquad (1.28)$$

If several populations with relative fractions a_i ($\sum_i a_i = 1$) are present

$$p(r = r_{xy}, \Delta t)\, dr = \sum_i \frac{a_i}{4\pi D_i \Delta t} \cdot e^{-\frac{r^2}{4D_i\Delta t}} \cdot 2\pi r\, dr \qquad (1.29)$$

holds for the 2D case (Fig. 1.9 d)) and accordingly for data of other dimensionality. In practice, either histogrammed data with finite bin width ($dr \rightarrow \Delta r$) or the cumulative probability density distribution

$$P(r^2 = r_{xy}^2, \Delta t) = \int_0^{r^2} P(r^2 = r_{xy}^2, \Delta t)\, dr^2 \qquad (1.30)$$

$$= 1 - \sum_i a_i \cdot e^{-\frac{r^2}{4D_i\Delta t}} \qquad (1.31)$$

can be fitted by the appropriate functions (Fig. 1.9 c)). The number of fractions is not a fit parameter but needs to be set according to either *a priori* knowledge about the sample or the quality of the fit, e.g. judged by the χ^2 error and inspection of the residuals. The latter should be randomly scattered around zero and show no systematic trends [83].

1.8 Biochemical model system: Giant unilamellar vesicles

Giant unilamellar vesicles (GUVs) served as a biochemical model system for observing 3D single particle motion in this work. The basic structure of cell membranes in most organisms is formed by a lipid bilayer separating the cytoplasm from the cell exterior. GUVs are one of several *in vitro* model systems for natural lipid bilayers. In an aqueous environment, lipids, which are amphipathic molecules consisting of a hydrophilic head group and a hydrophobic tail, arrange themselves in a bilayer with the headgroups facing outward and the tails pointing inward (Fig. 1.10 a)) for entropic reasons [101]. In GUVs, these bilayers form a spherical surface with a diameter of several tens of microns (Fig. 1.10 b)). In contrast to flat, supported lipid bilayers, the GUV membrane is not in contact with a solid substrate but usually surrounded by aqueous buffer. Thus, artifacts and defects due to lipid-substrate interaction are avoided. GUVs have been used to study e.g. lipid aggregation phenomena, mechanical properties of a lipid bilayer and protein interactions in a membrane but also as microscopic reaction containers [102].
They can be formed from a large range of lipid compositions, greatly affecting their properties. As a mimic of eucaryotic cell membranes, phospholipids and cholesterol, the most abundant lipid components in these membranes, are used. The phase state of the membrane depends on its constituents and the temperature. Below a transition temperature, lipids arrange in a liquid crystalline gel phase of low fluidity, whereas a fluid phase can be found at higher temperatures [101]. The order within the membrane can be disturbed by lipids containing kinked, unsaturated hydrocarbon chains. If these are not present in the membrane, high concentrations of cholesterol incorporated in the bilayer can prevent crystallization by disturbing interactions between the phospholipids [103]. Both effects increase the mobility of individual lipids in the membrane (Fig. 1.10 c)). Vice versa, cholesterol can also contribute to the order of the bilayer in the fluid phase by interacting with parts of the hydrocarbon chains close to the polar headgroups of the phospholipids [103].
Some lipid compositions lead to formation of small (*lipid rafts*, [104]) or large [105] phase domains in the lipid bilayer.
Fluorescently labeled lipids can be incorporated to visualize the GUV membrane or, at suitably low concentrations, to perform SPT experiments in the lipid bilayer.

In this work, GUVs were used as a simple model system exhibiting 3D particle motion on a well-defined topology. The knowledge that fluorescently labeled lipids incorporated in the GUV membrane diffuse on a spherical surface facilitated verification of tracking results. Further, minimal background fluorescence made tracking lipids on GUVs easier than tracking biomolecules inside living tissue.

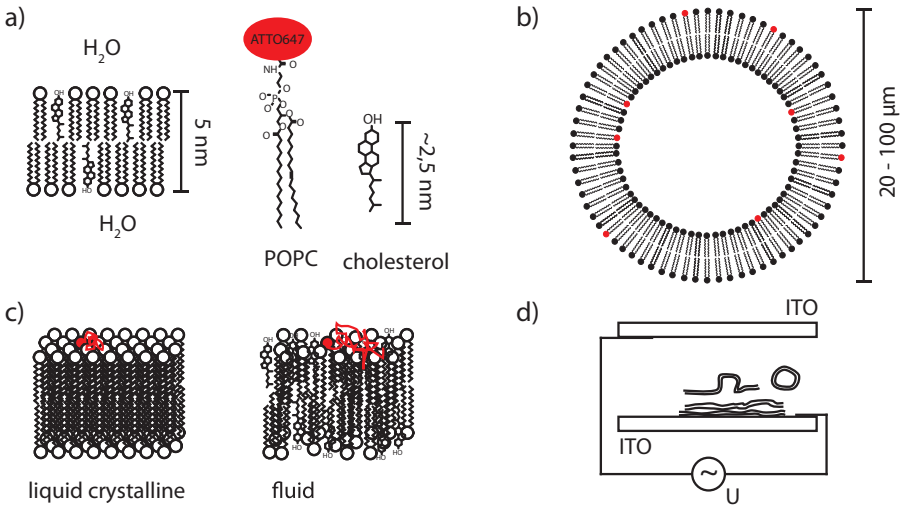

Fig. 1.10: **a)** Lipid bilayers consisted of cholesterol and DPPC or POPC. A small fraction of the lipids carried an ATTO647 dye at its headgroup. **b)** In GUVs the thin lipid bilayer forms a large vesicle of 20 - 100 µm diameter. **c)** Depending on the exact composition of the lipid mixture and the temperature, the bilayer displayed either liquid crystalline or fluid phase. This has a large impact on the mobility of individual lipids. **d)** GUVs were prepared by electroformation (sec. 2.1.5) [106].

GUVs were formed from binary mixtures of cholesterol and DDPC[3] or POPC[4]. Bilayers of these compositions can exist in different phase states at room temperature, depending on the fraction of cholesterol [107]. The phase state strongly affects the membrane fluidity. The ability to thus control the mobility of single lipids via the GUV composition was highly beneficial for optimizing the 3D tracking technique. From a different perspective, the prolonged observation times for individual lipids achieved by applying 3D SPT (see. sec. 4.1.2) may expand the scope of applications of the model system itself e.g. by enabling more detailed observations of aggregation processes in lipid bilayers.

[3] **di**palmitoyl**p**hosphatidyl**c**holine
[4] 1-**p**almitoyl-2-**o**leoyl**p**hosphatidyl**c**holine

1.9 Biological model system: *Chironomus tentans*

In vivo experiments were performed in *C. tentans*. A concise description of the model system with a focus on the Balbiani ring (BR) mRNA particles investigated here was given by Daneholt in [108], from which the following brief summary was excerpted.
C. tentans is a dipteran 10 - 20 mm in size (Fig. 1.11 a)). The salivary gland cells of its larvae have particularly large nuclei of 50 - 80 µm diameter (Fig. 1.11 b), c)). Nuclei contain four polytene chromosomes, each of them consisting of 8000 - 16000 chromatids. Their perfect alignment leads to a characteristic striation of the chromosomes. Unlike in most other eucaryotic cells, the rest of the nucleoplasm is devoid of chromatin (Fig. 1.11 d)). The main function of the salivary gland cells is to produce and secrete proteins needed for building the larval tube from which the adult insects hatch. Some of these proteins have a size of more than 1 MDa and correspondingly large gene loci on the chromosomes. In the Balbiani ring transcription sites BR1, BR2, and BR3 on chromosome IV with high transcriptional activity, the structure of the polytene chromosomes is loosened in so called puffs (Fig. 1.11 d), g)).

1.9.1 The mRNA life cycle

Two large genes are encoded in BR2, designated BR2.1 (29 - 34 kilo base pairs (kbp)) and BR2.2 (32 - 41 kbp) [112]. The mRNA transcribed from the genes is only slightly smaller than the genes themselves (Fig. 1.11 g)). Already during transcription, protective chaperon proteins attach to the mRNA to form a spherical particle of about 50 nm diameter [113] (Fig. 1.11 f)). After transcription has been completed, the mRNPs dissociate from the polytene chromosome and distribute in the nucleoplasm. From the Stokes-Einstein equation (eq. 1.20) and measurements on inert particles an intranuclear viscosity of $\eta = 3$ - 5 cP has been determined [9]. The mobility of BR2.1 mRNPs was, however, found to be far below the expected value for free diffusion of a particle with the respective diameter. A detailed analysis indicated discontinuous motion of the particles [9]. The observed motion pattern could be explained by transient binding or interaction with larger structures on short timescales [18].
After export from the nucleus, ribosomes bind to mRNA in the cytoplasm and translation is initiated.

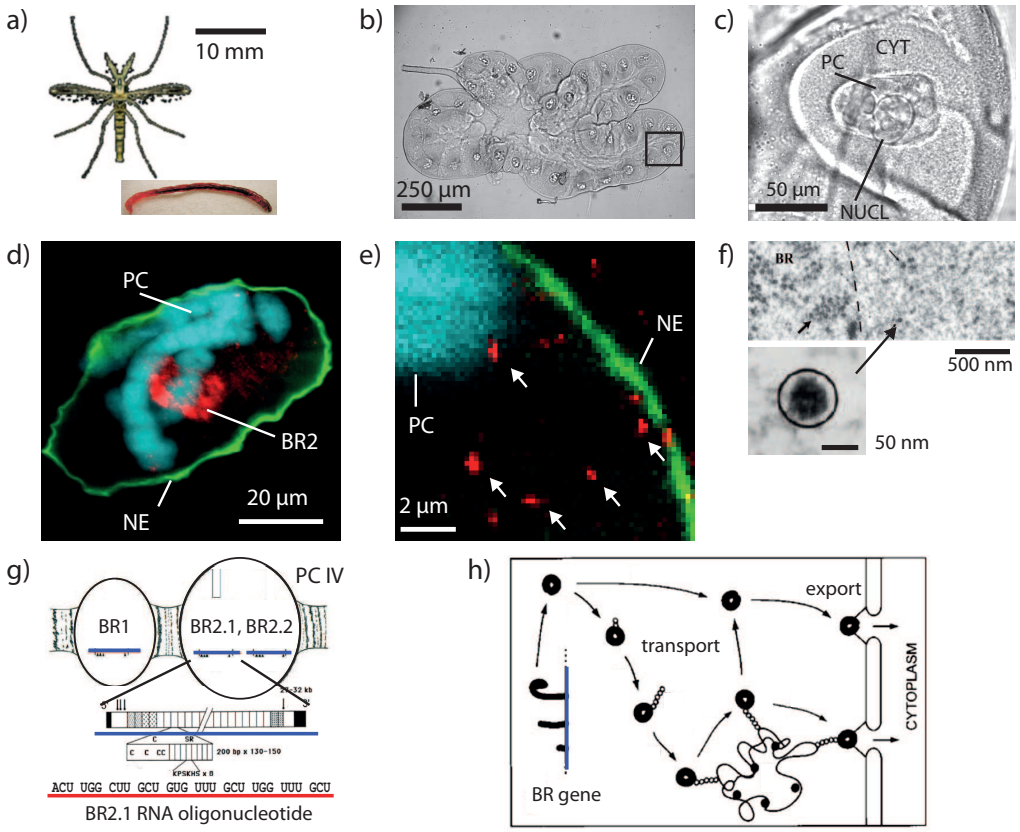

Fig. 1.11: *C. tentans* as a model system for mRNA tracking. **a)** Adult and larval stage. Adapted from [109]. **b)** Transmission image of a *C. tentans* salivary gland consisting of around 40 cells. **c)** Cells have a size of about 200 µm and carry a large nucleus of 50 - 80 µm diameter surrounded by cytoplasm (CYT). Polytene chromosomes (PC) and nucleolus (NUCL) can be identified. **d)** Fluorescence image of a nucleus with staining of the nuclear envelope (NE, green), the polytene chromosomes (cyan) and BR2.1 mRNA at the transcription site (BR2, red). **e)** Individual mRNPs (white arrows) can be observed. **f)** Electron microscopy images of mRNPs in fixed tissue show their spherical shape and a diameter of 50 nm [9, 110]. **g)** The BR1 and 2 transcription sites are located on PC IV. BR2 contains two genes, BR2.1 and BR2.2. BR2.1 mRNPs were specifically labeled by oligonucleotides carrying fluorescent dye molecules [110, 111]. **h)** mRNA is co-transcriptionally incorporated in a complex consisting of various proteins, transported through the nucleoplasm and exported through pores in the nuclear envelope. Adapted from [19]

1.9.2 mRNP tracking in *C. tentans* salivary gland cells

C. tentans salivary gland cells are well suited for *in vivo* mRNA tracking experiments. Other than in cultured cells, the chromatin is compacted in the polytene chromosomes. mRNP motion in the nucleoplasm is thus not hindered by the dense chromatin meshwork, making it easier to discern effects directly related to mRNA trafficking from unspecific interactions [9]. Further, the large diameter of the BR2.1 mRNPs studied here reduces their mobility and thus facilitates single particle tracking.
The size of the *C. tentans* salivary glands makes microinjection easier than in cultured cells. Injecting oligonucleotides targeted against repetitive parts of the BR2.1 mRNA sequence enables highly specific labeling without the need for genetic modifications to the organism [109]. On the other hand, the size of the specimen requires a sophisticated microscopy technique. Using light sheet illumination, single fluorescently labeled particles can be detected with high SNR and low fluorescence background even at a depth of several dozens of microns within these large specimen [12].

2 Methods

2.1 Methods

In this chapter, the methods used to obtain the results presented in the following chapters shall be outlined. Materials are listed in appendix A.

2.1.1 Light sheet calibration and characterization

ATTO647N was diluted in phosphate buffered saline (PBS) to a concentration of 100 µM, yielding a fluorescent liquid termed *calibration solution*, which allowed direct visualization of the excitation light sheet. The sample chamber was filled with the solution and sealed with a coverslip to prevent evaporation. Enclosure of air bubbles was avoided by slightly overfilling the sample chamber and letting the coverslip drop on it from a small height instead of sliding it over the chamber. The calibration solution was used for alignment of the excitation focus with the detection focal plane and camera field of view. The excitation focus can be identified by a dip in fluorescence intensity along the excitation axis (Fig. 2.1 a)). Moving the illumination objective and thus the excitation focus back and forth with a micrometer screw was helpful for identifying the focal position during visual inspection. The calibration solution was further used to determine the light sheet width from the fluorescence intensity profile.
To determine the light sheet height or thickness, sub-diffraction sized fluorescent beads (TetraSpeck 0,2 µm) were embedded in 1,5 - 2,5 % agarose. 1 µL fluorescent bead stock solution were diluted in 9 µL PBS in a reaction tube and sonicated for 10 min. Agarose was melted in a micro-wave oven (medium power, 30 s). 200 µL of the liquid agarose were added to the reaction tube, shaken in a vortexer for a few seconds and immediately transferred to a sample chamber using a 1000 µL lab pipette. Cutting away part of the pipette tip was helpful in transferring the highly viscous agarose. The sample chamber was sealed with a coverslip while the agarose was still liquid to avoid evaporation. The sample was imaged with the 10x air objective (NA 0.28) since its depth of field of ≥ 8 µm surpassed the typical light sheet thickness of 2 µm. By moving the sample through the light sheet in steps of 50 nm and acquiring an image frame at each position, the axial profile of the excitation light sheet could be sampled. Assuming that particles were kept well within the depth of field, the peak intensity of a single bead throughout the image stack reflected the excitation intensity. Intensity profiles were fitted with a Gaussian peak and $1/e^2$-radius values plotted against position along the optical axis (Fig. 2.1 b)). The resulting profile reflected the light sheet illumination profile according to eq. 1.1.

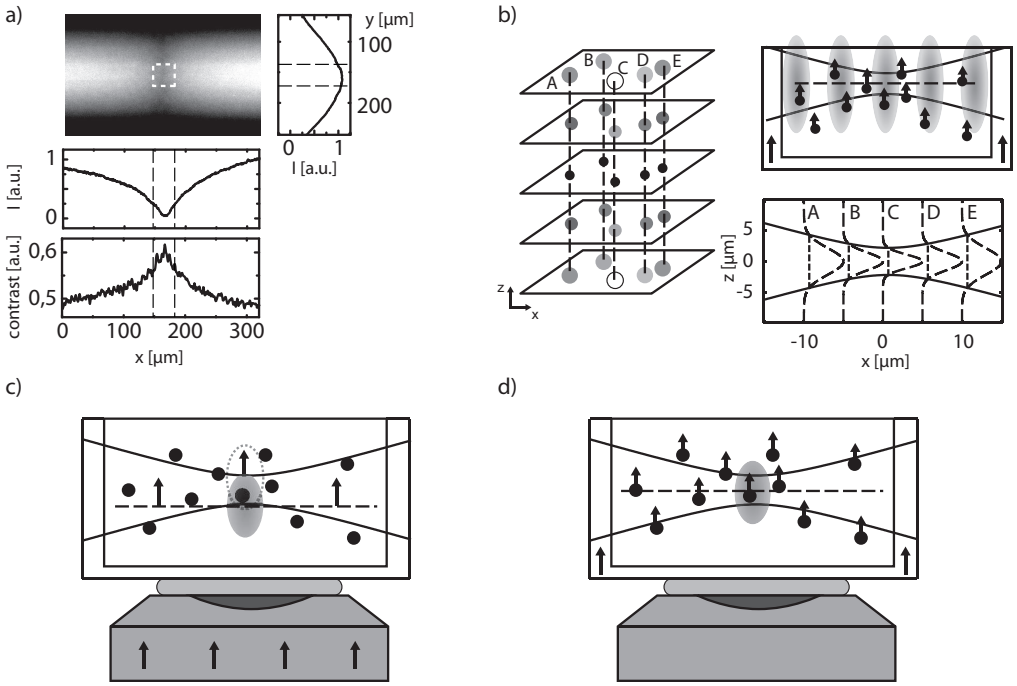

Fig. 2.1: Characterization of the light sheet. **a)** Calibration solution was used to determine the width of the light sheet and find the illumination focus. The latter could be identified as a region of reduced fluorescence intensity or high contrast due to suppressed background intensity. Dashed lines indicate a typical object field during tracking experiments. **b)** By moving immobilized fluorescent beads (A-E) through the light sheet, its axial profile was measured. Intensity traces of individual beads (dashed) were fitted by a Gaussian profile. The resulting $1/e^2$-radii represented the light sheet height profile according to eq. 1.1 (solid). **c)** The detection PSF was determined by keeping the beads fixed with respect to the light sheet illumination profile and displacing the detection objective and with it the focal plane (dashed line). **d)** In contrast, overlapping light sheet and detection focal plane and displacing the sample chamber yielded the complete system PSF (illumination $\otimes$ detection). Schematics not to scale.

2.1.2 PSF measurements

The same sample of immobilized beads was further used to measure detection and system PSF with the 40× objective. Since a water immersion objective was used, refractive index mismatch did not degrade the PSF at greater sample depth (compare Fig. 3.12 b)) as would be the case for oil immersion objectives [114]. To measure the detection PSF, the piezo-driven objective mount was set to its center position and a fluorescent bead brought to the focus using the motorized sample stage. Subsequently, an image stack was acquired by displacing the detection objective between individual frames. Thus, the excitation intensity at the position of

the fluorescent bead stayed constant while different planes of the detection profile were sampled (Fig. 2.1 c)).
In contrast, the detection objective was kept in a fixed position to determine the system PSF. Instead of the detection objective, the sample stage was moved axially between frames to drive a fluorescent bead through the focal plane. In this case both, axial position of the PSF and position within the light sheet illumination profile changed between frames (Fig. 2.1 d)). Since the light sheet FWHM was larger than the detection objective depth of field, the difference between system and detection PSF was small within a few 100 nm from the focal plane. Thus, either detection or system PSF could be used to obtain calibration data sets.

2.1.3 Photon counts

The number of detected photons in a single molecule signal N_{Phot} was calculated from the number of digital counts in the image data contributing to the signal N_{cts}. A photon hitting the camera chip results in an electron being stored in the semiconductor pixel with a probability corresponding to the quantum efficiency (QE) of the detector material at the specific wavelength. After the exposure time has elapsed, pixels are read out and the number of electrons is converted to a digital value as characterized by the analog-to-digital-unit (ADU) conversion factor B. In EMCCD cameras, the electron signal is amplified by a gain factor G during the readout process. N_{Phot} and N_{cts} are related by

$$N_{Phot} = N_{cts} \cdot B/(G \cdot QE) \tag{2.1}$$

Hardware-related parameters were obtained from datasheets provided by the manufacturer (see Tab. A.9). The number of counts per signal can be determined by summing up all counts in an image region larger than the PSF diameter and subtracting a background value determined in a spatially or temporally separated reference image region. Alternatively, the results of a 2D Gaussian fit (eq. 1.14) to the intensity peak were used. From eq. 1.14 follows

$$N_{cts} = \int\int_{x,y=-\infty}^{\infty} I_0\,(x,y)\,\mathrm{dx}\,\mathrm{dy} = 2\pi \cdot I_0 \cdot w_x \cdot w_y \tag{2.2}$$

for the total number of counts contributing to the signal, where I_0 the peak amplitude above background and $w_{x,y}$ the peak width along x and y respectively, assuming that $w_{x,y}$ were significantly smaller than the evaluated image region.
Control experiments showed that both approaches yield similar results. Minor deviations resulted from inaccuracies of the Gaussian PSF model.

2.1.4 Test particles in aqueous solution

Aqueous solutions of TetraSpecks of different sizes were prepared by diluting bead stock solution (0,1 - 1,0 µL TetraSpecks or 20 nm fluorospheres) in 200 µL PBS and sonicating for 10 min. These test samples were used to optimize and characterize the performance of the real-time tracking algorithms (sec. 3.4.7 - 3.4.9). Since smaller particles exhibited a higher mobility, smaller final concentrations were required for unambiguous trajectory assignments. The sample chamber was slightly overfilled and immediately sealed with a coverslip to avoid evaporation and sample drift due to airflow.

2.1.5 GUV preparation

GUV samples were provided by Katharina Scherer. Vesicles were formed by electroformation [106] from different compositions of cholesterol and DPPC or POPC. Lipids labeled with ATTO647 were added at a concentration of $\approx 10^{-7}$ mol% before electroformation. Lipid compositions used for the experiments presented here are summarized in Tab. 2.1.

Tab. 2.1: GUV compositions used for the experiments presented here. POPE: 1-**p**almitoyl-2-**o**leoyl-**p**hosphoethanolamine, DPPE: 1,2-**dip**almitoyl-**p**hospho**e**thanolamine.

mobility	composition	tracer	chapter
minimal	90 mol% DPPC, 10 mol% cholesterol	10^{-7} mol% DPPE-ATTO647	4.1.1
low	50 mol% DPPC, 50 mol% cholesterol	10^{-7} mol% POPE-ATTO647	4.1.2
high	100 mol% POPC	10^{-7} mol% POPE-ATTO647	4.1.3

Briefly, 20 µL of 1,3 mM lipid mixture were placed on two indium tin oxide coated coverslips respectively and the solvent evaporated. An O-ring was placed on one of the coverslips, filled with 265 µL of 250 mM sucrose solution and sealed with the second coverslip. Application of an AC voltage (1,8 V, 12 Hz) for 3 h at 40 - 60 °C led to formation of vesicles with a diameter of up to 20 - 100 µm (compare Fig. 1.10 d)). For imaging, 10 µL of the vesicle solution were added to a clean sample chamber filled with 150 µL of 250 mM glucose solution. The sample chamber was sealed with a coverslip. Due to the difference in density between glucose and sucrose solution, vesicles sank to the bottom of the sample chamber and remained there. The sample chamber bottom was optionally filled with a thin layer of low concentration agarose gel to elevate smaller vesicles to a position suitable for light sheet illumination (compare sec. 3.1.3).

2.1.6 SPT in *C. tentans* salivary gland cells

C. tentans salivary gland cell samples were prepared by Tim Kaminski. A detailed protocol for the preparation of salivary gland cells can be found in [115]. Briefly, complete salivary glands were dissected from fourth instar larvae and placed in a sample chamber coated with poly-L-lysine (Fig. 2.2 a)). Glands were initially kept in PBS.

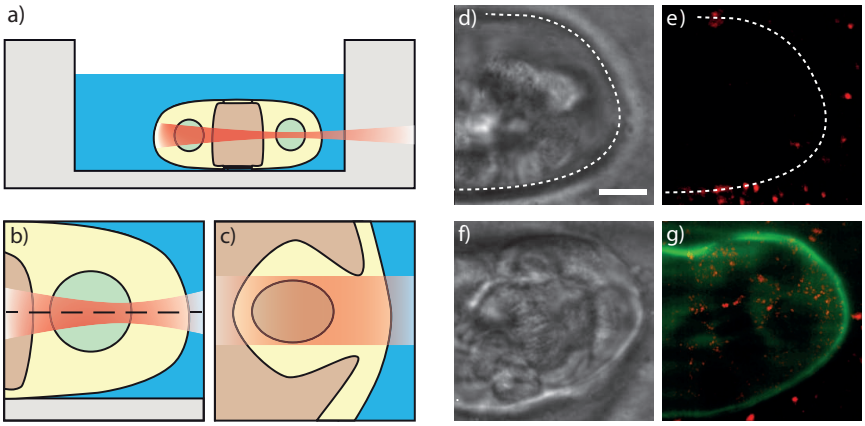

Fig. 2.2: Single molecule tracking in *C. tentans* salivary gland cells. **a)** Schematic of a salivary gland inside the sample chamber, illuminated from the side by light sheet (not to scale). Adapted from [12]. **b)** Detailed view. The light sheet is focused onto the salivary gland cell nucleus and excites fluorescence in a thin layer. **c)** Top view as observed in the microscopy images. The light sheet was tailored to have approximately the same width as the salivary gland cell nuclei. **d), f)** White light transmission images of *C. tentans* salivary gland cell nuclei (scale bar 10 µm). Dashed line indicates position of nuclear envelope. **e), h)** Fluorescence overlay images. The cell in the bottom row was microinjected with NTF2 (green, nuclear envelope) and mRNA oligonucleotides (red). The cell in the top row shows some autofluorescence mainly in the cytoplasm but not in the nucleus.

Fluorescent probes were delivered by microinjection of fluorescent markers or labeled proteins using a FemtoJet microinjector (Eppendorf, Germany) with an injection pressure of 500 - 1000 hPa for 0,1 - 0,5 s at a compensation pressure of 70 - 110 hPa. Injection solution was freshly prepared from stock before each experiment and small volumes ($\approx 10^{-12}$ L) were injected into the nuclei of several cells on the side of the gland facing the illumination objective. The injection volume was varied slightly to ensure the presence of at least a few cells with optimal labeling density in each gland.
After microinjection, PBS was optionally replaced by hemolymph, which kept the cells functional for a longer period of time. To reduce the required buffer volume from 160 µL to 40 µL, two polytetrafluoroethylene spacers could be placed at the

ends of the sample chambers. If hemolymph was used, the sample chamber was immediately covered with mineral oil to avoid evaporation and coagulation. Otherwise, a coverslip was used for this purpose.
The following strategies were used to label different compartments within the salivary gland cell nuclei. Concentrations correspond to injection solution before microinjection. Except for SYTOX green, all labels could be delivered in a single injection.

Nuclear envelope
: 50 µM NTF2-AF546. The nuclear transport factor NTF2 localized to the nuclear pore complex and thus resulted in a rim stain of the nucleus. Furthermore, it filled the nucleoplasm but did not enter the volume occupied by polytene chromosomes and the nucleolus. At high concentrations within the nucleoplasm, the two latter compartments and their structure could be identified as regions of lower fluorescence intensity.

Polytene chromosomes
: 5 mM SYTOX green. SYTOX green is a DNA staining dye usually used to identify apoptotic cells since only the nuclear envelopes of these cells become permeable to the dye. By microinjection directly into the nucleus, it was possible to label DNA in live cells with it.

BR2.1-mRNA
: 25 nM mRNA-oligonucleotides listed in Tab. A.2. Oligonucleotides specifically bound to BR2.1 mRNA. Unbound oligonucleotides moved too rapidly to be tracked at typical frame rates. Further, mRNA was highly abundant in the nucleus. Therefore it was assumed that all oligonucleotides were bound to mRNA.

rRNA
: 25 nM rRNA-oligonucleotides listed in Tab. A.2. Oligonucleotides specifically bound to the 28s subunit of ribosomal RNA particles. Again, unbound oligonucleotides moved too rapidly to be tracked at typical frame rates.

2.1.7 Analysis of jump distance distributions and sequences

As outlined in sec. 1.7, the distribution of jump distances is fitted by an appropriate probability function to determine diffusion coefficients as a measure for particle mobility in a typical SPT data analysis [74]. Datasets usually consist of hundreds to thousands of short trajectories, each comprising just a few particle localizations. The temporal order of the jump distances in a trajectory is thus of minor interest and neglected when analyzing jump distance distributions. Only relative frequencies of mobility states are extracted from the datasets.

This changes if long trajectories as generated by 3D feedback tracking are available. In addition to the relative frequency of mobility states, transitions between them may be revealed by analysis of the temporal order of jump distances if trajectories consist of hundreds of localizations. Ideally, the mobility states would be well separated and dwell times in either state could be identified by merely defining a jump distance threshold. However, in a realistic case, jump distances in each state follow the Maxwell-Boltzmann distribution for thermal motion and distributions overlap to a large extent.
A random trajectory of n_{loc} localizations results in a sequence of $n' = (n_{loc} - n_{JD})/n_{JD}$ non-overlapping jump distances, where n_{JD} indicates the number of frames, over which the jump distance is calculated. The sequence of squared jump distances shall be denoted $r^2(t)$. In a tracking experiment, the time t is separated into discrete time points $t \rightarrow i = 1 \ldots n'$. Defining a threshold r^2_{lim} separates $r^2(i)$ into two populations. The particle can be assumed to be part of population A of lower mobility at time i if $r^2(i) \leq r^2_{lim}$ and part of population B of higher mobility if $r^2(i) > r^2_{lim}$. If $P(r^2)$ denotes the cumulative distribution of squared jump distances, $p_A = P(r^2_{lim})$ corresponds to the probability of finding the particle in population A whereas $p_B = (1 - p_A)$ is the probability of finding it in population B (Fig. 2.3 a)) at a given time point.

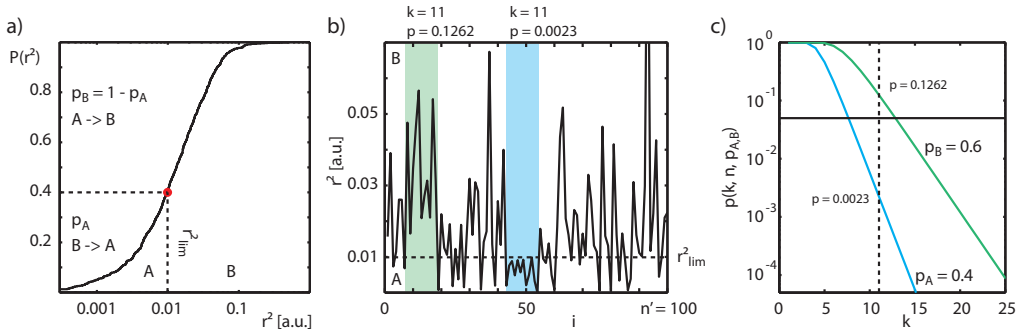

Fig. 2.3: Jump distances as a Bernoulli process. **a)** Cumulative distribution of squared jump distances $P(r^2)$. A particle is in state A with probability $p_A = P(r^2_{lim})$ and in state B with p_B. **b)** Temporal sequence $r^2(i)$ of $n' = 100$ squared jump distances. Dwell times of $k = 11$ time points and their p-values are indicated in green (B) and blue (A). **c)** p-value as a function of dwell time length k for $n' = 100$ and $p_A = 0{,}4$ (blue) or $p_B = 0{,}6$ (green) according to eq. 2.17. Black solid: $p < 0{,}05$ significance threshold. Black dashed: $k = 11$.

Determining the state of the particle at time point i can thus be referred to as a Bernoulli trial. It has exactly two outcomes A or B, which occur randomly with a certain probability given by $P(r^2_{lim})$. In the classical description of a Bernoulli trial, p_A denotes the *success probability* of finding the particle in A.
Similarly, transitions between the two states can be described as a Bernoulli trial. A particle in A at time point i is found in B at $i+1$ with probability p_B or remains

in A with probability p_A. Again, there are exactly two outcomes to the transition process. Either it is successful or it fails.
A series of n' independent Bernoulli trials with success probability p_A results in a binomial distribution $B(n', p_A)$. Its expectation value $\mathrm{E}[x]$ and variance $\mathrm{Var}[x]$ are

$$\begin{aligned} \mathrm{E}[B(n', p_A)] &= p_A \cdot n' && (2.3) \\ \mathrm{Var}[B(n', p_A)] &= p_A \cdot (1 - p_A) \cdot n' && (2.4) \end{aligned}$$

These equations apply for both, the number of occurrences of either state A or B and the number of transitions between A and B, in a sequence of jump distances $r^2(i)$. Since the probability p_A to find the particle in state A was determined from the actual distribution of jump distances $P(r^2)$, it is immediately clear that eq. 2.3 will always be fulfilled. The number of time points at which the particle is found in state A and B are per definition

$$\begin{aligned} n'_A = \mathrm{E}[B(n'_A, p_A)] = p_A \cdot n' && (2.5) \\ n'_B = \mathrm{E}[B(n'_B, p_B)] = p_B \cdot n' && (2.6) \\ n' = n'_A + n'_B && (2.7) \end{aligned}$$

However, if the analysis is applied to analyze transitions between A and B, the temporal sequence of the jump distances becomes important. If the jump distances in the trajectory are drawn randomly from the jump distance distribution $P(r^2)$, transitions occur stochastically. Hence, the expected absolute numbers of transitions according to eq. 2.3 are

$$\begin{aligned} \mathrm{E}[N_{A\to B}] = \mathrm{E}[B(n'_A, p_B)] = p_B \cdot n'_A = p_B \cdot p_A \cdot n' && (2.8) \\ \mathrm{E}[N_{B\to A}] = \mathrm{E}[B(n'_A, p_A)] = p_A \cdot n'_B = p_A \cdot p_B \cdot n' && (2.9) \\ \mathrm{E}[N_{tot}] = \mathrm{E}[N_{A\to B}] + \mathrm{E}[N_{B\to A}] = 2 \cdot p_A \cdot p_B \cdot n' && (2.10) \end{aligned}$$

The corresponding values of the variance are

$$\begin{aligned} \mathrm{Var}[N_{A\to B}] = p_B \cdot (1 - p_B) \cdot n'_A = p_B \cdot p_A \cdot n'_A && (2.11) \\ \mathrm{Var}[N_{B\to A}] = p_A \cdot (1 - p_A) \cdot n'_B = p_A \cdot p_B \cdot n'_B && (2.12) \\ \mathrm{Var}[N_{tot}] = \mathrm{Var}[N_{A\to B}] + \mathrm{Var}[N_{B\to A}] && (2.13) \\ = p_A \cdot p_B \cdot (n'_A + n'_B) = p_A \cdot p_B \cdot n' && (2.14) \end{aligned}$$

A normalized expression for the number of transitions is the relative transition frequency $s = N_{tot}/n'$. Since for large n', the binomial distribution $B(n', p_A)$ can be approximated by a normal distribution the standard deviation of s is $\sigma_{\hat{s}} = \sqrt{\mathrm{Var}[\hat{s}]}$.

Thus,

$$\hat{s} = \mathrm{E}\left[s\left(p_A\right)\right] = \frac{N_{tot}}{n'} = 2 \cdot p_A \cdot \left(1 - p_A\right) \tag{2.15}$$

$$\sigma_{\hat{s}}\left(p_A\right) = \frac{\sqrt{\mathrm{Var}\left[N_{tot}\right]}}{n'} = \sqrt{p_A \cdot \left(1 - p_A\right)/n'} \tag{2.16}$$

With these equations at hand, the significance of deviations between the experimentally determined transition probability $s(p_A)$ and the expectation value $\hat{s}(p_A)$ for a Bernoulli trial can be tested using confidence intervals derived from $\sigma_{\hat{s}}$. A significantly higher transition probability than in a randomly drawn sequence, $s(p_A) > \hat{s}(p_A)$, indicates a repulsive mechanism frequently forcing the particle from state A to B and back. Vice versa, $s(p_A) < \hat{s}(p_A)$ indicates a retention of the particle in either of the states, e.g. because a particle transiently binds to a structure and its mobility is thus reduced during the interaction time.
One should note, however, that jump distance distributions of states with a specific diffusion coefficient found in SPT datasets do usually overlap. Therefore populations A and B defined by a threshold r^2_{lim} do not necessarily correspond to states parametrized by a diffusion coefficient. The comparison between $s(p_A)$ and $\hat{s}(p_A)$ merely yields insights into the randomness of the temporal sequence of jump distances.
Dwell times in either of the states appear as multiple successive identical outcomes of the Bernoulli trial testing the state A or B of the particle. The probability to observe k successive occurrences of a state with probability p_A is simply p_A^k. However, in the case of trajectories with n' jump distances, a formula is sought, which describes the probability $p(k, n', p_A)$ to observe k such events in a row in a sequence of n' Bernoulli trials with stochastic outcome. An expression for $p(k, n', p_A)$ is given in eq. (16) in [116] (Fig. 2.3 c)):

$$p(k, n', p_A) = \sum_{m=0}^{\frac{n'+1}{k+1}} (-1)^m \; p_A^{mk} \, p_B^{m-1} \left(\binom{n' - mk}{m-1} + p_B \binom{n' - mk}{m} \right) \tag{2.17}$$

According to the conventions of statistical data analysis, the significance of a dwell time of k frames in a state observed with probability p_A is quantified by its p-value $p(k, n', p_A)$. A dwell time with $p(k, n', p_A) < 0{,}05$ is termed significant in a sense that the probability to observe it in a sequence of n' jump distances randomly drawn from the jump distance distribution $P(r^2)$ is $< 5\%$.
An example is given in Fig. 2.3 b), c). Dwell times of $k = 11$ time points in state A or B were found in a series of $n' = 100$ jump distances at a threshold chosen such that $p_A = P(r^2_{lim}) = 0{,}4$ and $p_B = 1 - p_A = 0{,}6$. The p-values are $p_1 = 0{,}0023$ and $p_2 = 0{,}1262$ respectively. Since $p_A < p_B$, a dwell time of duration $k = 11$ in state A is much more significant - or stochastically unlikely - than a dwell time of the same duration in state B.

3 Astigmatic 3D SPT in a light sheet microscope

A light sheet microscope was developed to enable astigmatic 3D SPT in extended specimen. In this chapter, the details of the instrumentation layout are presented. The implementation of the illumination optics, sample mounting unit and detection unit are described in sec. 3.1. To keep particles of interest close to the focal plane, a feedback loop was devised as outlined in sec. 3.2. In sec. 3.3, data handling and algorithms for live tracking as well as post-processing of the data are discussed. Characteristics and limitations of the method were tested and results are presented in sec. 3.4.

3.1 Setup

The instrument presented here (Fig. 3.1) was built around the body of a commercial inverted microscope to benefit from pre-assembled components like white light illumination, objective revolver, filter wheels, camera mounting and manual focus drive. The sample stage was removed from the instrument and replaced by a custom stage suited for light sheet illumination, manufactured by the precision mechanics workshop of the Institute for Physical and Theoretical Chemistry, University of Bonn. A light sheet illumination unit and an insert for a cylindrical lens were added to the instrument. In collaboration with LaVision BioTec (Bielefeld), a motorized stage was installed. All components are listed in appendix A.3.

The setup can be divided into the following building blocks:

- laser control unit
- illumination unit
- sample mounting unit
- detection unit
- lab PC and instrument control software

The design and implementation of these components will be outlined in the following sections.

3.1.1 Laser control unit

The instrument was equipped with three lasers to allow illumination with monochromatic light of wavelength $\lambda = 488$ nm, $\lambda = 532$ nm and $\lambda = 640$ nm (see Tab. A.3). All three laser lines were aligned by appropriate dichroic mirrors (DC1,2 in Fig.

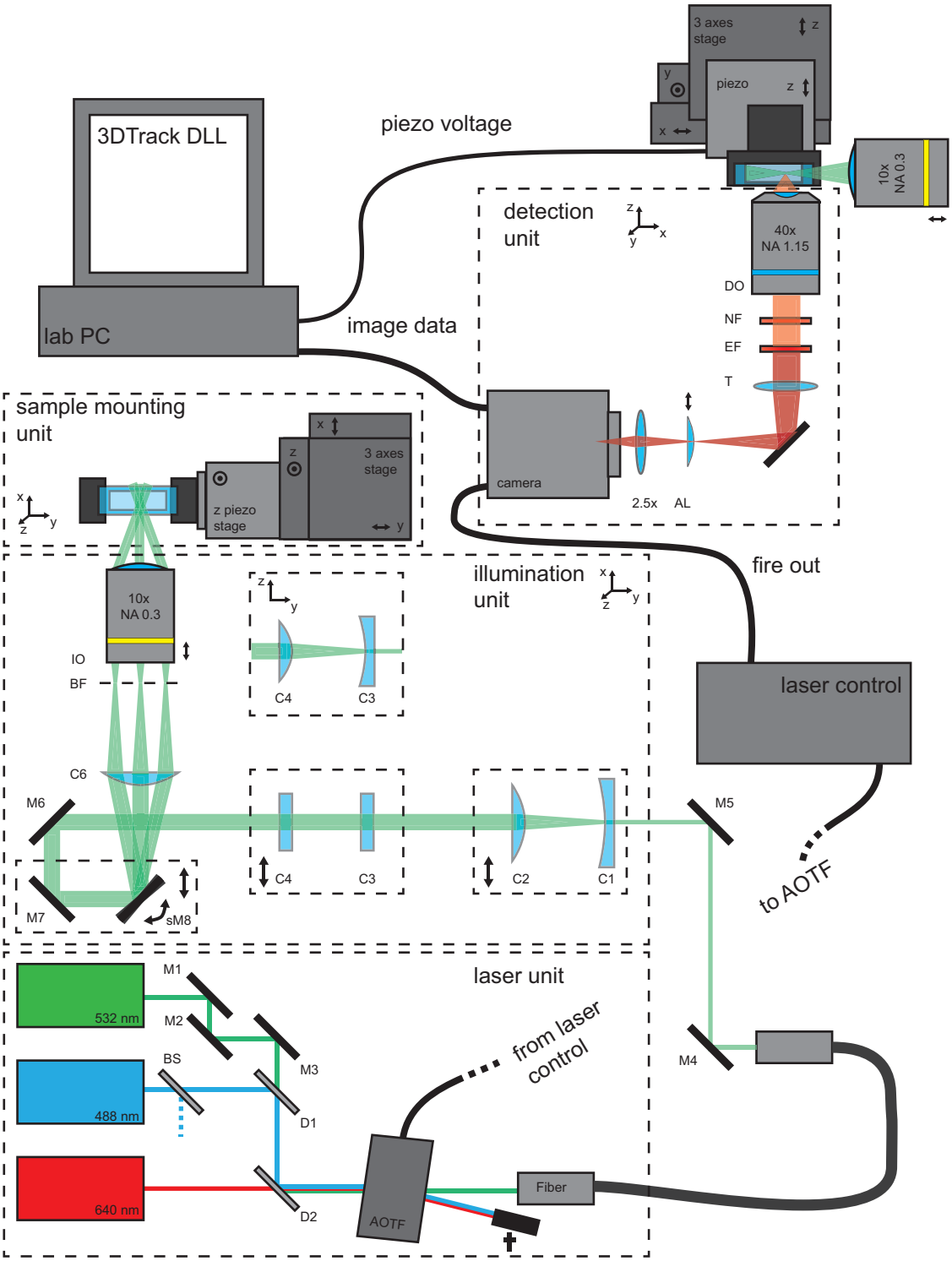

Fig. 3.1: Complete overview of the light sheet microscopy setup. A detailed description of the building units can be found in sec. 3.1.1 - 3.1.5.

3.1) and passed an acousto-optical tunable filter (AOTF), which was used to electronically modulate the illumination intensity and switch between laser lines by selectively guiding light onto an optical fiber.
The AOTF channels could be controlled externally by applying a voltage of 0 - 5 V. A laser control unit manufactured by the electronics workshop of the Institute for Physical and Theoretical Chemistry, University of Bonn, was used to address the AOTF channels and enabled imaging with predefined illumination sequences. All laser lines could also be activated and intensity-modulated manually, both separately or simultaneously.

3.1.2 Illumination unit

All laser light transmitted by the AOTF was coupled into a 0,7 µm diameter single mode optical fiber. The fiber was employed to separate the laser control unit from the rest of the instrument on the one hand and transmit only the TEM_{00} mode on the other hand. Its output was aligned with the illumination optics by mirrors M4 and M5 and passed a beam expanding subunit affecting the beam height as depicted in Fig. 3.2. Initially, the illumination unit contained a cylindrical zoom unit consisting of five cylindrical lenses, which allowed for a $1-7\times$ elongation of the beam profile in one direction [117]. Considering the fact that in practice either a very thin or a very thick light sheet was used, it was later replaced by a simple $5\times$ vertical beam expander (C3, C4). The beam expander could be moved in and out of the beam path to switch between two illumination settings. The lower number of surfaces in the illumination unit led to a reduced amount of back reflections and facilitated maintenance of the setup. Similarly, a $5\times$ horizontal beam expander (C1, C2) could be slid into the beam path to increase the lateral width of the light sheet (Fig. 3.2).
Subsequently, the laser light was guided onto an optical delay line consisting of mirrors M6, M7 and the scanning mirror sM8. The width of the collimated beam was focused by cylindrical lens C6 onto the back focal plane (BF) of the illumination objective (IO) to generate a beam with constant width within the sample. The combination of C6 with a focal length of 150 mm and the IO focal length of 20 mm led to a $7{,}5\times$ reduction of the beam width after the objective.
M7 and sM8 were mounted on a translation stage to facilitate accurate placement of the scanning mirror sM8 in the focal plane of C6. Its scanning axis was perpendicular to the image plane such that the scanning motion was projected into the specimen position by the telescope consisting of C6 and IO. The scanning motion of sM8 was used to pivot the light sheet around the intersection of illumination and detection optical axis in the object field [41]. If activated, the scanning mirror was continuously driven by a sawtooth voltage with negligible reset time and a frequency of 200 Hz. The scan amplitude could be adjusted manually using a

potentiometer. Scanning over the full aperture of the illumination objective resulted in a maximum scanning angle of ±7,5° in the specimen (compare Fig. 3.9) as expected for a NA 0,28 objective. Fig. 3.2 c) shows the improvement in image homogeneity due to reduced shadowing artifacts by using the scanning mirror.

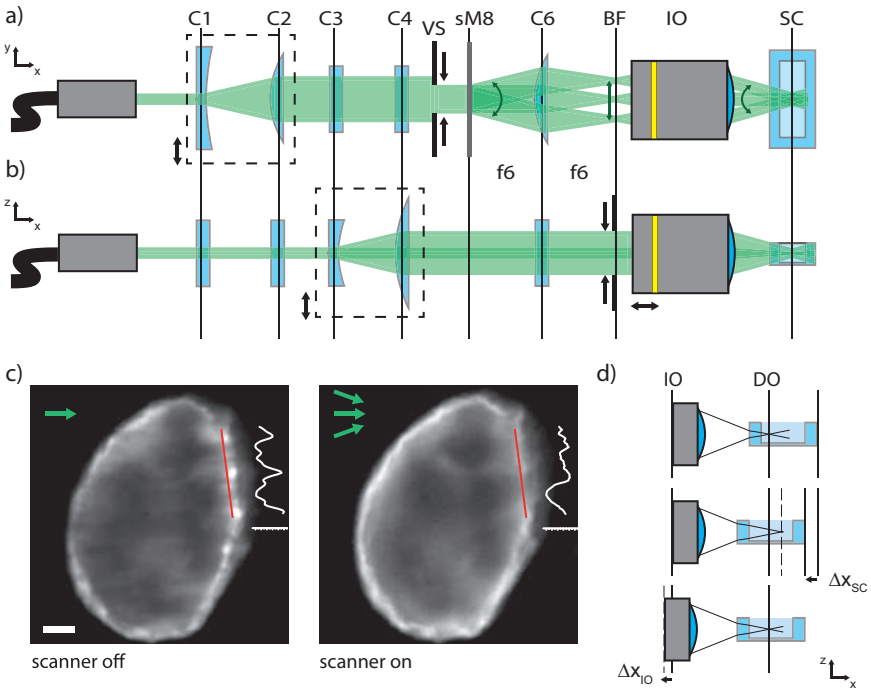

Fig. 3.2: Illumination beam path. **a)** Top view. The width of the light sheet can be adjusted by a 5× cylindrical beam expander (C1,C2) and a slit aperture (VS). **b)** Side view. The height of the light sheet can be adjusted by the cylindrical beam expander (C3,C4) and an aperture in the back focal plane (BF) reducing the effective NA. **c)** Use of the scanning mirror sM8 reduces shadowing artifacts as indicated by intensity profiles (white lines) along the nuclear envelope (red lines). With scanning activated, a more homogeneous illumination is achieved. Arrows indicate direction of illumination. Scale bar 10 µm. **d)** Focal shift occurs when the sample chamber is displaced along the illumination axis. The light sheet focus no longer coincides with the detection axis (DO). It can be compensated for by repositioning the illumination objective (IO) according to eq. 3.1.

The light sheet thickness in the focal plane was governed by the effective illumination NA. It could be reduced by means of an adjustable aperture between C6 and IO to generate a light sheet with reduced sectioning but larger Rayleigh length. At NA 0,28, a diffraction-limited value of ≈ 1µm can theoretically be achieved. Since an air objective was used to focus the illumination light through the sidewall of the sample chamber (see section 3.1.3) into aqueous imaging buffer, spherical aberrations increased the thickness of the illuminated section in practice. The varying

ratio of the path length in air and aqueous medium when focusing to different positions along the illumination axis further led to a shift in the position of the light sheet focus when the sample cuvette was displaced (Fig. 3.2 d)). It could be compensated for by adjusting the position of the illumination objective. From Snell's law it can be derived that a sample chamber displacement of Δx_{SC} required the illumination objective to be moved by

$$\Delta x_{IO} = \left(1 - \frac{n_{Imm}}{n_{Buff}}\right) \cdot \Delta x_{SC} \tag{3.1}$$

where n_{Imm} and n_{Buff} denote the refractive indices of the immersion medium between illumination objective and sample chamber and of the buffer medium inside the sample chamber respectively. For use of an air objective and aqueous medium $n_{Imm} = 1{,}000$, $n_{Buff} = 1{,}333$ and thus $\Delta x_{IO} = 0{,}25 \cdot \Delta x_{SC}$.

3.1.3 Sample mounting unit

The specimen itself was kept in a custom-made sample chamber with an inner volume of 160 µL. It was made of optical grade Suprasil glass and had 2 mm sidewalls and a 170 µm coverslip bottom for use with an inverted microscope. To reduce sample motion due to airflow, it could be sealed with a glass lid and fixated in a metallic sample holder. The sample holder was designed to provide stability, enable quick exchange of the sample and maintain accessibility of the specimen for external manipulation e.g. by microinjection.
The sample holder was magnetically attached to the motorized sample stage consisting of a 3-axis translation stage with large travel range for coarse positioning and a piezo stage for fast and accurate axial displacement of the sample. The piezo stage had a travel range of 100 µm, a positional accuracy of 20 nm and a resonant frequency of 300 Hz at a load of 35 g, corresponding to the weight of the sample holder and a filled cuvette. It was operated in closed loop mode via an appropriate controller.
Not the entire volume of the sample chamber was usable for light sheet microscopy (Fig. 3.3). Constraints were imposed by both, the illumination profile and the detection objective. Both, the light sheet and the detected fluorescence, should only pass through flat glass surfaces but not the edges of the sample chamber. While a slight degradation of the light sheet would only affect the SNR, a distorted detection PSF might affect the accuracy of axial localizations.
The conditions for illumination with a 2 µm FWHM light sheet of 640 nm wavelength and detection with the 40× water immersion objective (NA = 1,15) are indicated in Fig. 3.3. The light sheet focus must be positioned at least 50 µm

above the chamber bottom to avoid the edges of the sample chamber. Specimen of more than 100 µm thickness should not be placed next to the sidewall of the chamber but rather at a distance of at least 100 - 200 µm to allow for undistorted fluorescence detection. Smaller specimen could be placed on a thin layer of transparent substrate (e.g. low percentage agarose) to reside within the optimal volume for both, illumination and detection.
Only small volumes of immersion liquid were applied for use with an immersion objective. Otherwise the immersion spread beyond the sample chamber bottom, crept up its sidewall due to adhesive forces and refracted the light sheet.

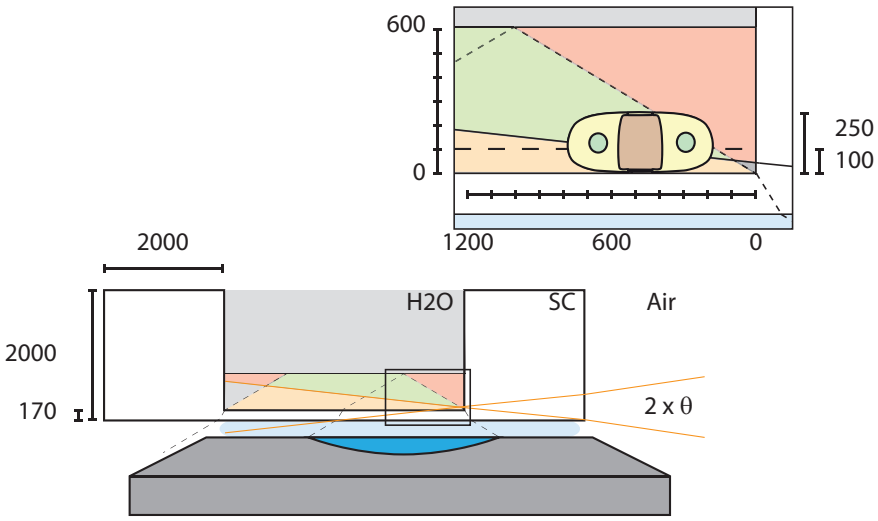

Fig. 3.3: Schematic representation of the sample chamber (SC) drawn to scale. All distances in µm. Dashed lines indicate the collection angle of the detection objective. Green: Neither illumination nor detection affected by sample chamber edges. Orange: Illumination through edge of SC but detection through flat surfaces. Red: Both, illumination and detection affected by sample chamber. Grey: Inaccessible to detection objective.
Magnified view: *C. tentans* salivary gland in SC. Nuclei are located approximately 100 µm from the coverslip bottom of the chamber. If placed at a small distance from the sidewall, nuclei are illuminated by an undistorted light sheet and fluorescence detection is not affected.
Illumination from the right. Parameters: $n_{buff} = 1{,}333$, $n_{SC} = 1{,}458$, $\lambda = 640$ nm, $w_0 = 1{,}86$ µm ($1/e^2$-radius).

3.1.4 Detection unit

Fluorescence was detected in an inverted configuration through the bottom of the sample chamber. The instrument was equipped with three detection objectives

(Tab. A.7). A 10× or a 20× objective was used for characterization measurements and alignment purposes. For tracking experiments, a 40× water immersion objective was employed. Objectives could be positioned electronically by a piezo mount with a travel range of 100 µm or with a manual focus drive. Two independent filter wheels could be used to insert filter cubes or fluorescence filters in the detection path. Since fluorescence detection is decoupled from illumination in light sheet microscopy, a small holder for emission filters was devised to replace the standard filter cubes and omit the beam splitting dichroic mirror. Up to three 1 inch filters could be stacked in it. In the first filter wheel, notch filters were used to specifically block scattered excitation light. The second filter wheel contained additional band pass filters to further reduce photon background (Tab. A.8).
Fluorescence light passing the filter sets was focused by the tube lens (1× or 1,5×) before being deflected to the desired camera port. An additional 2,5× secondary magnification was inserted for experiments using EMCCD cameras to achieve an appropriate pixel size in the images. Due to their smaller physical pixel size this was not necessary for sCMOS cameras. Camera properties are listed in Tab. A.9. The precision mechanics workshop of the Institute for Physical and Theoretical Chemistry, University of Bonn, manufactured a modified C-mount adapter, which enabled effortless insertion of the cylindrical lens C7 for astigmatic imaging.
EMCCD cameras provided high sensitivity in the low photon regime [118] while sCMOS cameras offered higher frame rates at larger image fields. The AOTF could be triggered in such a way that the specimen was only illuminated during the camera chip integration time.
The detection efficiency of the setup can be estimated to be $\lesssim 15\%$ at a wavelength of 650 nm (Tab. 3.1).

Tab. 3.1: Estimated transmission efficiency for the detection path of the instrument at $\lambda = 650$ nm. Values according to manufacturer information and [56].

element	transmission at $\lambda = 650$ nm
coverslip	96%
objective NA 1,15 collection angle	29%
objective transmission	75%
notch filter	90%
bandpass filter	95%
tube lens	96%
mirror	96%
cylindrical lens	96%
camera chip QE	92%
total	15%

3.1.5 Instrument control software

Most of the experiments were conducted using the commercial instrument control software Imspector v5.5 (LaVision BioTec) extended by the *Ultramicroscopy* and *TrackDev* modules. It allowed control of scanning mirror, motorized sample stage including piezo stage and most of the cameras (Ixon DU897, Ixon DV860, pco.edge) from a graphical user interface and ran on a standard lab PC. The Orca Flash 4.0 camera was controlled by Hokawo v1.6 (Hamamatsu Photonics) running on a separate PC.
LaVision BioTec kindly provided a dynamic link library (DLL) interface in their software for on-the-fly analysis of image data during an experiment (*TrackDev* module). Details are described in the following section.

3.2 Feedback loop

The DLL interface was used to implement a feedback loop for 3D SPT. It consisted of three main elements: A cylindrical lens encoding axial information relative to the focal plane in the image data (sec. 1.7.3), a DLL containing code to extract the information and convert it to an output signal (sec. 3.2.1), and a fast piezo stage for repositioning the sample based on the output signal (sec. 3.1.3).
The aim of keeping a particle in focus can be achieved either by adjusting the position of the focal plane, i.e. repositioning the detection objective, or by displacing the particle and thus the sample itself. The latter approach was chosen here since it maintained overlap between the plane of light sheet illumination and the focal plane. Displacing the detection objective via the piezo mount would have been feasible, too, but would have required a simultaneous adaptation of the illumination optics.
Axial information was encoded in an astigmatic PSF (aPSF) and extracted by either of several algorithms (sec. 3.2.1). Based on previously acquired calibration data, an axial position relative to the focal plane could be determined from the PSF shape. Image analysis was performed by a DLL, which was called by the instrument control software immediately after an image had been read out from the camera chip and transferred to PC memory. This process required tens to hundreds of microseconds. Imaging was typically performed at a kinetic cycle time of 16 - 50 ms per frame. The total execution time of the feedback loop should thus not exceed 1 - 2 ms. Therefore, a constant and predictable execution time of the image analysis algorithm was desirable.
The single output value of the DLL returned to the instrument control software was a floating point value corresponding to the voltage, which was to be applied to the piezo stage to bring the particle being tracked back to the focal plane. It was passed on to the piezo stage controller via an RS-232 port.

3.2.1 The tracking DLL

Real-time image analysis and program code for the tracking DLL was written in C++ using Microsoft Visual C++ Express 2010. If the live tracking option was activated in the instrument control software, the DLL was called immediately after an image frame had been transferred to PC memory. A number of parameters were passed to the DLL (Tab. 3.2), amongst them a pointer to the memory address of the image data. This enabled immediate analysis of the image with minimum data transfer overhead.
The general outline of the DLL code is depicted in Fig. 3.4. It can be divided into six separate tasks which are outlined below.

Tab. 3.2: Parameters passed to the tracking DLL and their meaning. * indicates pointer type variables.

type **parameter**	function
*unsigned short** **image**	pointer to image data memory address
int **width**	width of image in pixels
int **height**	height of image in pixels
*double*** **profiles**	pointer to memory address of pre-allocated array profiles
*float*** **timestamp**	pointer to memory address of pre-allocated array timestamp
int **profileLen**	length of arrays, number of frames in experiment
double **advalue**	current voltage reported from stage sensor
double **davalue**	current target voltage for piezo stage
unsigned int **counter**	counter for current image number within experiment
*bool** **imageChange**	indicates if new image data was written to memory

1. Load parameters

The arrays *profiles* and *timestamp* were allocated before the first call to the DLL and had a static memory address such that information could be kept in memory during the course of an experiment. The arrays consisted of up to eight columns and a number of rows determined by the number of images to be taken (*profileLen*). The piezo stage was equipped with a strain gauge sensor, which reported its current position in terms of a voltage to the variable *advalue*. Due to fluctuations and forces induced by loading the stage or mechanical coupling to the detection objective it differed slightly from the voltage *davalue* externally applied to the stage. A *counter* was used to keep track of the current frame index within the experiment.
The DLL could be selected to either run sequentially with, or independently of image acquisition. In the latter case, the next image frame acquisition could already start before DLL execution was terminated to ensure a constant frame rate independent of potential lag times induced by the DLL. If its execution time was of similar length as the kinetic cycle time of the camera, image data might be overwritten during execution of the DLL. To identify such incidents, the Boolean indicator *imageChange* was introduced. It was set to *true* each time image data were transferred to memory and reset to *false* at the beginning of the DLL code.
Before compilation of the DLL, a static path was set, pointing to an ASCII file containing tracking parameters. Its contents could conveniently be adjusted by a graphical user interface written in MATLAB. If the DLL was called for the first time in an experiment (*counter* = 0), all parameters needed for 3D SPT were loaded from the file and placed in the array *timestamp* in PC memory (see Tab. B.1).

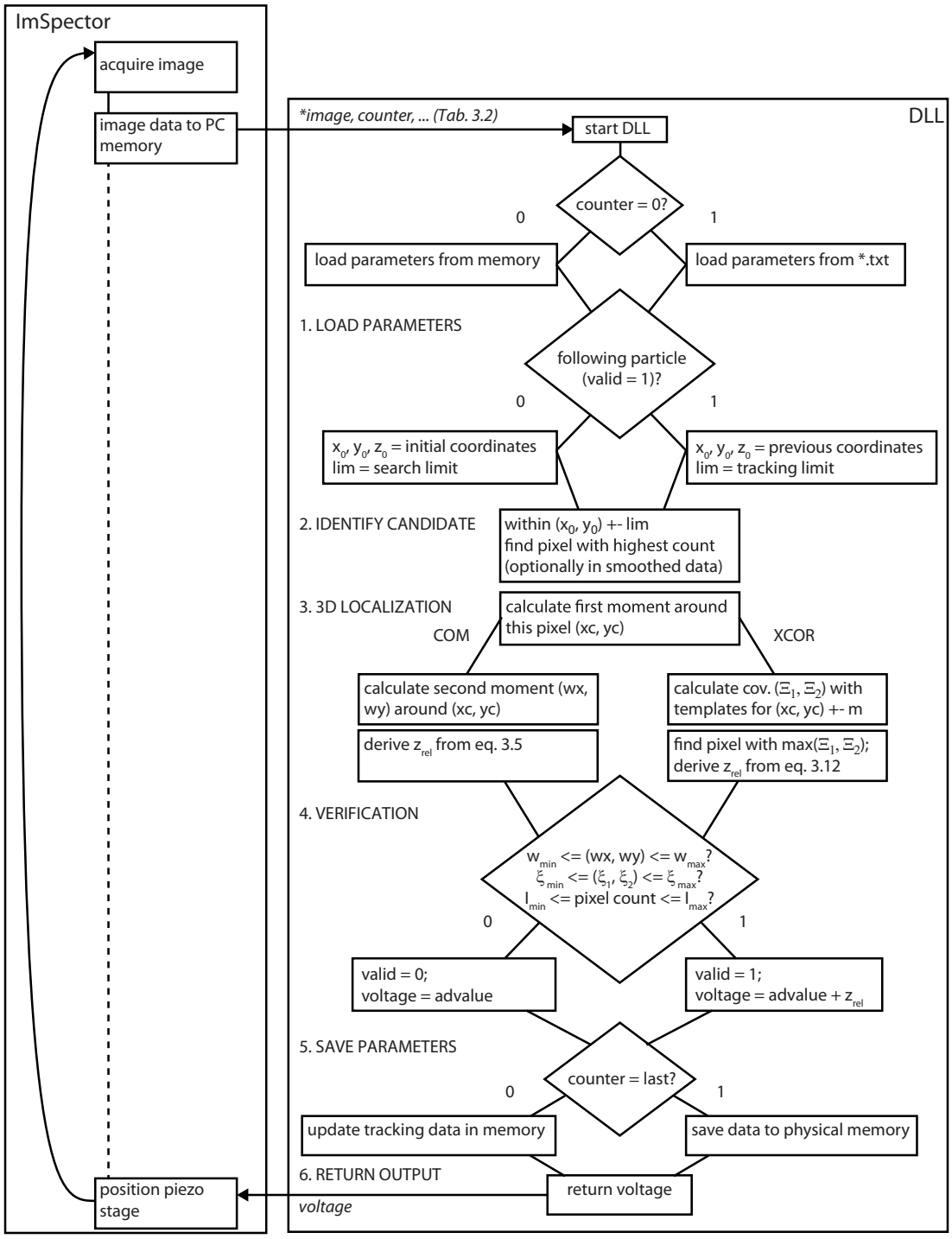

Fig. 3.4: Basic flow chart of the tracking DLL. Image acquisition was controlled by ImSpector instrument control software and the DLL called after an image frame had been transferred from the camera chip to PC memory. Image data were analyzed and the new voltage of the piezo stage returned to ImSpector.

2. Identify a candidate

Particle candidates were identified in two sequential steps based on user-supplied tracking parameters. Assuming sparse emitters with a mutual separation much larger than the average particle displacement between frames, an initial candidate localization was determined by finding the brightest pixel within a region of interest (*search window*) in the image. To avoid picking up noise, image data were smoothed with a 3×3 pixel Gaussian kernel

$$k = \frac{1}{16}\begin{bmatrix} 1 & 2 & 1 \\ 2 & 4 & 2 \\ 1 & 2 & 1 \end{bmatrix} \tag{3.2}$$

during the candidate search. Raw data were not affected by this procedure.
If the algorithm had already latched onto a particle, the search window was centered around its previous localization. The window size was chosen according to the mobility of the particles and allowed for a displacement of a certain number of pixels along each axis between subsequent frames. Usually, a small number $(2-10)$ of missing frames, in which a candidate was not verified, was accepted during live tracking to accommodate for intensity fluctuations and occasional larger displacements. If no particle had been identified within the previous frames, the search window was centered around the initial user-defined coordinates and enlarged to increase the probability of detecting a particle.
Before executing the following localization steps, the candidate was preliminarily verified by estimating the peak height. The background count level $\tilde{I}$ in the vicinity of a candidate at pixel coordinates (x_0, y_0) was estimated by taking the mean value of the four pixels at coordinates $(x_0, y_0) \pm 5$. Only if the count level in the brightest pixel, $I(x_0, y_0)$, exceeded the background level $\tilde{I}$ by a minimum value, the intensity distribution was analyzed more accurately.

3. 3D localization

The *lateral* position (x_c, y_c) of a candidate of sufficient signal level was calculated with sub-pixel accuracy by the first moment (*center of mass*, COM) of the raw intensity distribution:

$$(x_c, y_c) = \sum_{i,j=-m}^{m} \left(I(x_0+i, y_0+j) - I_{bg}\right) \cdot (i,j) \Bigg/ \left(\sum_{i,j=-m}^{m} I(x_0+i, y_0+j) - I_{bg} \right) \tag{3.3}$$

where the indices (i, j) run from $-m$ to m with the value of m stated as a tracking parameter in the ASCII file mentioned above. The background level I_{bg} was

estimated from the image data as $I_{bg} = \min(I(i,j)) + k \cdot \sqrt{\min(I(i,j))}$ here, with an empirically chosen factor k accounting for background noise fluctuations, which critically depended on camera model and EM gain settings.
Subsequently, the *axial* localization of the particle candidate was determined from the shape of the intensity distribution. Astigmatic PSF shapes are most commonly analyzed by fitting an elliptical Gaussian peak (eq. 1.14) to the data [119, 120] and comparing the $1/e^2$-radius along the x- and y-axis, w_x and w_y, to a calibration dataset $\left\{w_x^{cal}(z_{rel}), w_y^{cal}(z_{rel})\right\}$. Both, Gaussian fitting and finding the best match between the measured PSF width and the calibration dataset, involve iterative optimizations. Since the number of iterations before convergence depends on the quality of of the initial parameters and the SNR, the execution time of the DLL cannot be predicted. These conditions are not favorable for real-time applications. Therefore two different algorithms were implemented here to extract axial information from the shape of the PSF. Both of them used previously acquired calibration data for axial localization of the particle relative to the focal plane (z_{rel}).

The first approach (*COM*) relied on the second moment (variance) of the intensity distribution in a subimage to estimate the width of the PSF along both image axes

$$(w_x, w_y)^2 = \sum_{i,j=-m}^{m} (I(x_c - i, y_c - j) - I_{bg}) \cdot (x_c - i, y_c - j)^2 \Bigg/ \left(\sum_{i,j=-m}^{m} I(x_c - i, y_c - j) - I_{bg} \right) \tag{3.4}$$

Only pixels with $I(i,j) > I_{bg}$ were considered. Crucial for the second moment calculation was the correct choice of the subtracted background intensity I_{bg} (see sec. 1.7.1, [79]).
To obviate also the iterative procedures in deriving z_{rel} from (w_x, w_y), either their ratio [121] or their difference [96] were fitted with a linear slope

$$\begin{aligned} \Delta w(z_{rel}) &= w_y(z_{rel}) - w_x(z_{rel}) = m \cdot z_{rel} + b \\ \Leftrightarrow \quad z_{rel} &= (\Delta w(z_{rel}) - b)/m \end{aligned} \tag{3.5}$$

allowing for the direct calculation of z_{rel} from the slope parameters.
The second approach (*XCOR*) relied on the calculation of normalized covariance values between the raw image data and templates extracted from an experimentally acquired PSF. While localization using cross-correlation with entire PSF image stacks has been reported before [54, 78], the approach presented here requires just two PSF images. One template of $(2m+1) \times (2m+1)$ pixel size was extracted from above and one from below the focal plane (Fig. 3.5). From the raw data and

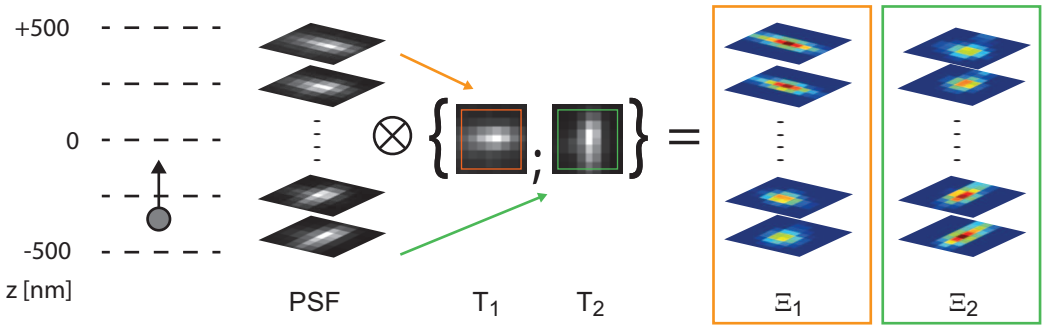

Fig. 3.5: Principle of axial localization by template matching. An image stack of an immobilized fluorescent bead is acquired and templates $T_{1,2}$ extracted. Calculating normalized covariance of the stack with the templates yields covariance images $\Xi_{1,2}$ (Blue: low values. Red: high values.)

each of these templates T_p (p = 1,2), two normalized covariance images Ξ_p were calculated according to

$$\Xi_p(x,y) = \sum_{i,j=-m}^{m} \frac{\Big(I(x+i,y+j) - \bar{I}(x,y)\Big) \cdot \Big(T_p(i,j) - \bar{T}_p\Big)}{\langle I_{xy}\rangle \cdot \langle T_p\rangle} \tag{3.6}$$

where $\bar{T}_p$ and $\bar{I}(x,y)$ are the mean values of the template and the subimage area used for the calculation and

$$\langle I_{xy}\rangle = \sqrt{\sum_{i,j=-m}^{m} I(x+i,y+j)^2} \tag{3.7}$$

$$\langle T_p\rangle = \sqrt{\sum_{i,j=-m}^{m} T_p(i,j)^2} \tag{3.8}$$

denote the root mean square intensities of the subimage and the templates. To speed up the calculation, the template images were normalized to $\bar{T}_p = 0$ and $\langle T_p\rangle = 1$ before the experiments. Normalization and use of covariance instead of mere cross-correlation calculation alleviated bias towards brighter image features and allowed the use of templates and images with different offset intensity [79]. Subsequently, the pixel (x_m, y_m) with the highest average covariance value was identified in an image area of $(2n+1)\times(2n+1)$ pixels centered around the intensity peak (x_c, y_c) (eq. 3.3) according to

$$(x_m, y_m) = \underset{x,y\,\in\,[x_c,y_c\pm n]}{\arg\max} \; frac\Xi_1(x,y) + \Xi_2(x,y)2 \tag{3.9}$$

The values $\xi_p = \Xi_p(x_m, y_m)$ were considered for further calculation of the axial particle localization. While the amplitude of the covariance curves as a function of

z_{rel} depended on SNR (Fig. 3.6 a)) - a higher SNR resulted in higher values due to reduced noise fluctuations -, the normalized metric

$$\chi = \frac{\Delta\xi_p}{\sum_p \xi_p} = \frac{\xi_2 - \xi_1}{\xi_1 + \xi_2} \tag{3.10}$$

was found to be insensitive to SNR (Fig. 3.6 b)) and further provided a linear calibration curve such that

$$\chi(z_{rel}) = m \cdot z_{rel} + b \tag{3.11}$$

$$\Leftrightarrow \quad z_{rel} = \left(\frac{\chi - b}{m}\right) = \left(\frac{\Delta\xi_p}{\sum_p \xi_p} - b\right) \Big/ m \tag{3.12}$$

For reference purposes, a third version of the DLL (*G2D*) was implemented, which used a least squares minimization algorithm to fit an elliptical Gaussian peak (eq. 1.14) to the data. It was not used for actual tracking experiments but only for characterization purposes. Applicability in real experiments was hampered by a comparably long execution time of the algorithm (see below). Furthermore, it depended on the number of iterations before convergence of the algorithm, which, in turn, was strongly affected by SNR and the quality of the initial guesses obtained from the COM algorithm.

4. Candidate verification

After performing 3D localization on a candidate signal with the first moment calculation for lateral and either COM or XCOR for axial localization, the resulting parameters were used to verify once more if the candidate was likely to represent a particle to be tracked. For this purpose, either the values ($w_{x,y}$) determined for the second moment of the intensity distribution or the normalized covariance values ($\xi_{1,2}$) needed to lie above a minimum and below a maximum threshold specified in the tracking parameter file. If the candidate was verified, its center coordinates became the new initial coordinates for the candidate search and the axial localization relative to the focal plane was added to the current piezo stage position to obtain the output value of the DLL.

5. Save parameters

Tracking results were stored in the arrays *profile* and *timestamp* in PC memory during the experiments (see appendix B.1). After the last image in the experiment had been acquired, the arrays were written to ASCII files in physical memory. While one file contained the complete list of tracking parameters (Tab. B.1), the

second one contained a table with the actual real-time tracking results including a system timestamp for each frame, the piezo stage voltage, an indicator for the candidate verification result and its coordinates, as well as PSF shape parameters (peak height and $\xi_{1,2}$ or $w_{x,y}$). An excerpt of such a table is displayed in Tab. 3.3.

Tab. 3.3: Output of the DLL in tracking mode.

frame#	last	time	advalue	davalue	valid	x_c	y_c	ξ_1	ξ_2	I(x_c,y_c)
...	...	...	...	...	...	...	...	...	...	...
12	9	282	4,9115	4,9166	0	43,60	60,33	0,36	0,32	228,75
13	9	298	4,9118	4,9166	0	43,60	60,33	0,27	0,38	235,50
14	9	313	4,9130	4,9078	1	53,90	60,34	0,69	0,72	1050,75
15	14	328	4,9054	4,9034	1	53,23	59,94	0,65	0,66	672,00
16	15	344	4,8996	4,8782	1	52,70	57,97	0,42	0,53	731,25
...	...	...	...	...	...	...	...	...	...	...

6. Return output value

If the particle candidate was verified, the new piezo stage voltage *davalue* was calculated from the axial localization of the particle z_{rel} and the previous stage position *advalue* according to

$$davalue = advalue + z_{rel}\,[\mathrm{V}] \tag{3.13}$$

Otherwise, the return value equaled the current stage position. The new goal voltage was returned to ImSpector and passed on to the piezo stage controller.
The piezo stage was addressed via an E-605 controller. It could be positioned by applying a voltage of 0 - 10 V to the controller. The voltage range translated to the full travel range of the stage of 0 - 100 µm. A PCI-e DAQ card was used to generate the voltage output for the piezo controller. The stage could be positioned manually in the instrument control software or, if live tracking was activated, by the value returned from the tracking DLL.

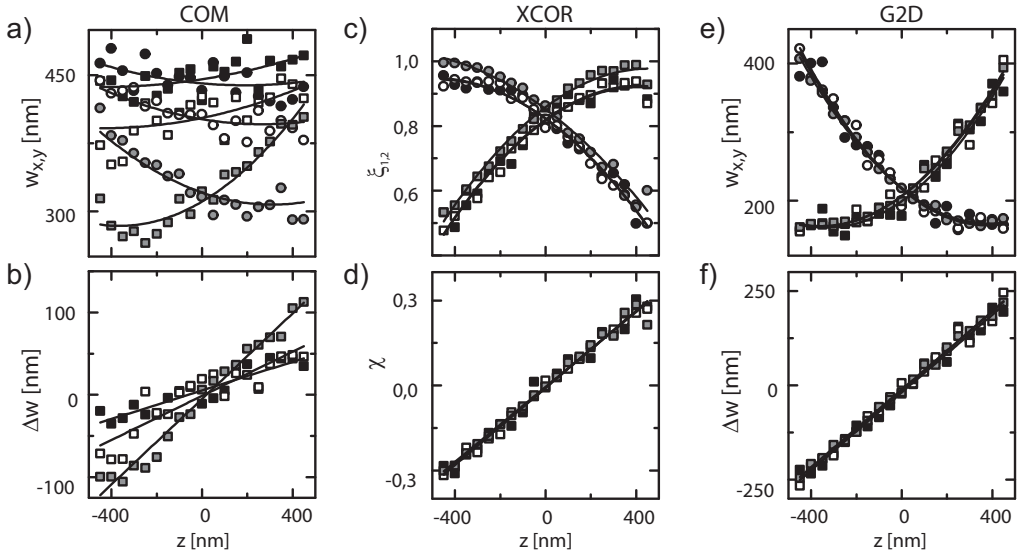

Fig. 3.6: Comparison of different metrics for axial localization. COM, XCOR and G2D were applied to test data sets of SNR = 65 (black symbols), 15 (white symbols) and 6 (gray symbols). **a)** COM: Second moment of the intensity distribution according to eq. 3.4 and **b)** linear estimator Δw (eq. 3.5) were strongly affected by SNR. **c)** XCOR: Similarly, normalized covariance values $\xi_{1,2}$ obtained by template matching were slightly reduced with decreasing SNR. **d)** However, the estimator χ (eq. 3.10) was not affected. **e)** G2D: The absolute values of $w_{x,y}$ obtained from a least squares fit as well as **d)** Δw stayed the same irrespective of SNR.

3.2.2 Characterization of axial localization methods

The performance of all three implementations of the DLL (*COM*, *XCOR*, *G2D*) was tested by calling it from a test environment and feeding it with artificial data generated from real measurements to simulate particle localization at different SNR levels. The raw dataset consisted of an image stack of an immobilized fluorescent bead obtained at a high SNR of approximately 400. From the raw data, the background count level was subtracted and the remaining signal scaled to a smaller in-focus amplitude I_{signal}. In the next step, a constant background of 100 counts was added to the downscaled signal. Shot noise was simulated by drawing random numbers from a Poissonian distribution for each pixel, with the pixel value representing the mean of the respective distribution. Thus, the background noise level was $\sigma_{bg} = \sqrt{100}$ for all images, while SNR values for the images could be determined from SNR $= I_{signal}/\sigma_{bg}$.

Artificial data were generated for SNR $= 4 - 65$. For each condition, the axial localization measures $w_{x,y}(z_{rel})$ and $\xi_{1,2}(z_{rel})$ as well as the linear estimators $\Delta w(z_{rel})$ and $\chi(z_{rel})$ according to eq. 3.5 (COM, G2D) and 3.10 (XCOR) were determined. Results for SNR values of 6, 15 and 65 are summarized in Fig. 3.6.

The parameters obtained from the COM approach were strongly affected by SNR. Both, $w_{x,y}(z_{rel})$ and $\Delta w(z_{rel})$ level off as SNR is reduced (Fig. 3.6 a), b)). Thus, calibration data were only valid for a specific SNR value.
Similarly, the normalized covariance values were slightly reduced at lower SNR. However, eq. 3.10 provided a normalized estimator for axial localizations independent of SNR (Fig. 3.6 c), d)).
Finally, the least squares fitting procedure (G2D) returned the same results for both, $w_{x,y}(z_{rel})$ and $\Delta w(z_{rel})$ irrespective of SNR conditions (Fig. 3.6 e), f)).

Using the same test datasets, the execution times for the different implementations of the DLL were measured. Since individual runs of the DLL required on the order of $10^{-4} - 10^{-5}$ s, it was not possible to directly measure the time for a single execution using C++ functions. Therefore, average execution times were determined for 10^5 repetitive calls. Values presented here were obtained for SNR = 8, a value typical for later SPT experiments.
For COM, the full DLL execution took $t_{CPU} = 35$ µs per signal. Using the XCOR approach increased this value to $t_{CPU} = 75$ - 375 µs. t_{CPU} scaled linearly with the number of pixels contained in each of the templates $(2n + 1)^2$ and the number of image pixels for which the normalized covariance was calculated $(2m + 1)^2$. G2D execution times were on the order of $t_{CPU} = 1200$ µs. Details are summarized in Tab. 3.4. The size of the subimage, to which the fitting algorithm was applied, was the same for both, G2D and COM, and corresponded to the template size in XCOR.
While COM provided the fastest and most simple determination of axial localizations but only worked for high SNR, G2D was accurate for all SNR conditions but slow. XCOR presented a good trade-off between speed and accuracy. It was insensitive to background noise and yielded accurate results with short calculation times.

Tab. 3.4: DLL execution times for SNR = 8. Template size $(2n + 1)^2$. Subimage size $(2m + 1)^2$. $t_{pxl} = t_{CPU} / \left(2 \cdot (2n + 1)^2 \cdot (2m + 1)^2\right)$.

DLL	n [pxl]	m [pxl]	t_{CPU} [µs]	t_{pxl} [µs/pxl]
COM	-	5	35	-
XCOR	4	1	75	0,0515
	4	3	111	0,0510
	5	1	208	0,0513
	5	3	375	0,0620
G2D	-	5	1200	-

3.2.3 Stack acquisition

Instead of tracking particles, the DLL could also be used to acquire image stacks. For this purpose, a different set of parameters was loaded to set the axial step size Δz between image planes, the number of frames to be acquired in each plane n_s, an offset z_0 as well as the direction of the stack (Tab. B.1). The voltage *davalue* returned to the instrument control software was not determined from the image information but calculated according to

$$davalue = z_0 \pm \text{ceil}\,(counter/n_s) \cdot \Delta z \tag{3.14}$$

where *ceil(x)* returns the smallest following integer value. After stack acquisition, the stage position for each image frame was stored in a text file. While stack acquisition was also possible with the motorized sample stage, using the piezo stage provided higher accuracy and enabled registration of tracking data with reference data based on the piezo stage position saved for each frame of the reference stack.

3.3 Post-processing and data handling

The tracking DLL was optimized for fast execution. Full image frames were acquired but only small subimages evaluated for real-time tracking of a single particle. Nevertheless, full image frames were acquired during experiments and contained many more particle localizations than those determined during live tracking. Real-time localizations were discarded during post-processing and all particles tracked again with refined parameters. In this sense, the tracking DLL presented primarily a tool to generate a higher number of long trajectories in SPT datasets (see Fig. 4.13). The longer a trajectory, the more information about the properties and behavior of an individual particle can be extracted and the higher the accuracy of this information [122].
A number of commercial or open source tracking programs are available [77]. The majority of them has been designed for classical 2D SPT. Only recently, groups working on 3D superresolution microscopy have published programs that can use the astigmatic shape of a PSF for 3D localization [123, 124]. Since these programs are still under development and provide only limited access to details of the algorithms, MATLAB-based tools for the different tasks related to 3D SPT experiments were developed. They worked with a standardized data format similar to the one used in [84]. Localizations were organized in tables (Tab. B.2) consecutively listing all localizations in an experiment with columns containing e.g. the frame number and coordinates. Trajectories were listed similarly (Tab. B.3) but with a number assigned to each trajectory as the primary sorting criterion. Thus, the trajectory table started with all localizations of the first trajectory in chronological order, followed by all localizations of the second trajectory, and so forth. Trajectories were numbered in order of occurrence of their first localization. The data format can be readily extended by appending further information in additional columns.

3.3.1 Particle localization and tracking

A graphical user interface was written in MATLAB to test and supply tracking parameters. Particles were localized with sub-pixel resolution in image data and localizations connected to trajectories. Piezo stage positions were extracted from the tracking DLL output files (Tab. 3.3) and added to localizations obtained during post-processing to obtain absolute 3D coordinates for each particle. Both, multi-page .tif files or series of individual image files could be analyzed. In batch mode, the algorithms were applied to a list of files. On a multi-core PC, parallel computing could be used to significantly reduce processing time.
The localization and tracking procedure consisted of three consecutive steps.

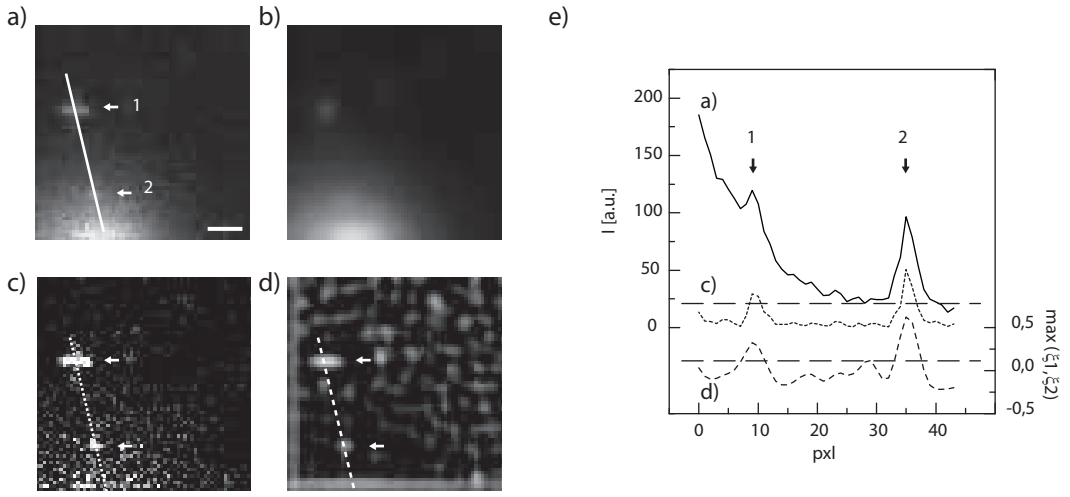

Fig. 3.7: **a)** Raw image with particles obscured by inhomogeneous background. Scale bar 5 µm. **b)** Median filtered background image (radius 4 pixels). **c)** Background-subtracted raw image. **d)** Normalized covariance image calculated from raw data and experimentally acquired PSF image. **e)** Raw data (solid), background subtracted raw data (dotted) and covariance (dashed) intensity profiles along the line indicated in **a), c), d)** (bottom to top). The latter two images allow particle detection based on thresholding (horizontal dashed lines).

1. Candidate identification

Similar to real-time tracking, the first step during post-processing was the identification of particle candidates. It was based on a local maximum search in either intensity or cross-correlation value images. A peak amplitude threshold and a minimum separation between local maxima were imposed as constraints to limit the number of candidates.

The intensity-based approach could optionally be optimized by smoothing the data with a Gaussian kernel (eq. 3.2) for low SNR data and by background subtraction for inhomogeneous background conditions. A median filter was chosen for the latter purpose since it preserved peaks and edges. The background image was calculated by median-filtering with a radius exceeding twice the PSF diameter (Fig. 3.7 c)) and subtracted from the raw data before identifying local maxima.

Normalized covariance calculation did not require any treatment of the raw data (Fig. 3.7 b)) and could be executed using either the experimental templates used during live tracking (sec. 3.2.1) or a Gaussian peak of appropriate width. As in real-time tracking, the normalized covariance was calculated for both templates and the average of the two resulting images used for candidate identification.

2. Candidate verification and sub-pixel particle localization

In a second step, one out of three algorithms could be used to determine sub-pixel *lateral* localizations and verify particle candidates.
Firstly, the first and second moment calculation (COM) introduced in sec. 3.2.1 was fast, but inaccurate and biased [79]. It was thus mostly used for fast previews of the tracking results and was not suited for the evaluation of data with low signal intensities.
Secondly, least squares fitting of a 2D Gaussian peak (G2D) was time-consuming but accurate and most reliable for low signal intensities.
Thirdly, radial center calculation presented a very fast and accurate alternative but has not been thoroughly characterized for astigmatic PSFs. It did further not yield any measures of the PSF shape and was thus suited for lateral but not for axial localization [80].
In all cases, the raw image data were used for particle localization, even if candidates were determined from smoothed data or covariance images. For COM and G2D, the width of the PSF $w_{x,y}$ was used to verify particle candidates. G2D further yielded a peak amplitude I_0, which was also used for this purpose. Lower and upper bounds for all three parameters were part of the tracking parameters supplied by the user. For *axial* localization, either the PSF width determined by COM or G2D or the normalized covariance values were compared to an appropriate calibration dataset obtained with the same method (sec. 3.2.2). All verified candidates were saved in a table format (Tab. B.2).

3. Trajectory assignment

Finally, in a third step, localizations were assigned to trajectories. Since the goal of 3D SPT was to observe individual long trajectories, the particle concentration was usually kept very low. Therefore, a simple nearest neighbor approach was sufficient for connecting localizations to trajectories. Localizations were linked to their nearest predecessor in the previous frame if the displacement did not exceed an upper limit. Each localization could be part of only one trajectory and unambiguous situations (more than one possible predecessor) led to a termination of trajectories. Optionally, the algorithm could tolerate gaps in trajectories, which were filled by linear interpolation between localizations more than one frame apart. Only trajectories exceeding a minimum but not a maximum length were finally appended to the table of trajectories as shown in Tab. B.3.
More elaborate algorithms can be employed to discern crossing trajectories by e.g. minimizing a global cost function or taking additional knowledge about particle properties into account [84].

3.3.2 Data analysis

Tools for trajectory analysis were written in MATLAB and designed to work on data of the format presented in Tab. B.3. For each image series, a separate trajectory table was created. Tables could be pooled for combined analysis of data from several experiments. Parameters like the image pixel size and the time interval between frames needed to be supplied by the user. Trajectories could be filtered spatially or according to their length. From the resulting list of trajectories, jump distance histograms and cumulative squared displacement distributions as well as mean square displacements as a function of time lag could be calculated and saved to MATLAB structure variables. Results were fitted with the appropriate functions (eq. 1.25, eq. 1.26 - 1.28, or eq. 1.31) in either MATLAB or Origin by least squares minimization.
Additional MATLAB tools allowed overlaying trajectory information with image data and also enabled incorporation of reference stack images. Exemplary trajectories presented throughout this work were identified by visual inspection of such image sequences, extracted from the list of trajectories for the corresponding experiment and analyzed in detail.

3.4 Characterization of the instrument

The following sections provide a thorough characterization of the instrument and tracking algorithms by highlighting technical properties of the setup on the one hand and testing its limitations on the other hand.

3.4.1 Laser illumination

Three laser lines were used to illuminate the specimen (Fig. 3.1). Only a fraction of the emitted power did eventually reach the specimen. Table 3.5 summarizes laser powers measured at different positions throughout the illumination beam path. For key components, the transmission efficiency is given.
The glass sidewall of the sample chamber led to a further power loss before the illumination light finally hit the specimen. Due to geometrical constraints this aspect could not be quantified. According to the manufacturer, 92 % transmission is expected.

Tab. 3.5: Transmission efficiency of optical elements in the illumination unit. Δp = 0,1 mW.

	488 nm		532 nm		640 nm	
position	p [mW]	efficiency	p [mW]	efficiency	p [mW]	efficiency
laser emission	110,0		49,0		39,4	
alignment optics	28,0	25%	16,5	34%	34,1	87%
AOTF in	26,7		15,8		34,1	
AOTF out/fiber in	18,9	71%	12,8	81%	32,6	96%
fiber out	9,8	52%	5,8	45%	12,6	39%
objective in	7,8		5,0		10,1	
objective out	5,8	74%	4,2	84%	9,1	90%

The power density at the specimen was controlled using electronics produced by the electronics workshop of the Institute for Physical and Theoretical Chemistry, University of Bonn. Briefly, a voltage of 0 - 10 V was applied to a channel of the AOTF controller to regulate the transmitted power fraction of the respective laser line. The relationship between the applied voltage and the transmitted power fraction was not linear as shown in Fig. 3.8. Since the voltages were controlled via small potentiometers, power densities could only roughly be reproduced. However, qualitatively similar values could be achieved. Voltages could be adjusted with an estimated accuracy of $< \pm 0{,}2$ V for all channels. From the slope of the curves in Fig. 3.8, a relative error of $< 5\%$ can be estimated for the 532 nm and 640 nm laser line and $< 10\%$ for the 488 nm line.

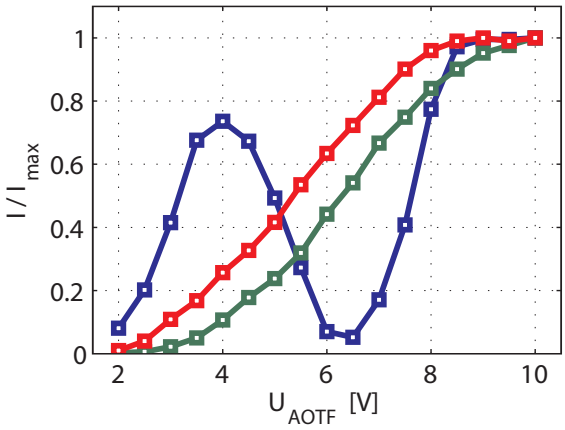

Fig. 3.8: Relative fraction of illumination power reaching the specimen in relation to the voltage applied to the respective AOTF channel for laser lines of 488 nm (blue), 532 nm (green) and 640 nm (red). For the 488 nm line, a secondary maximum was found. Measured data (squares) and interpolation (solid lines).

3.4.2 Light sheet dimensions

The illumination laser power was distributed across the light sheet profile. Its width within the object plane perpendicular to the optical axis of illumination was determined by imaging fluorescent dye in aqueous solution (sec. 2.1.1). Apart from occasional aggregates in the solution, the sample yielded a homogeneous emitter density with image brightness proportional to the illumination power density within the depth of field of the detection objective. Dye saturation did not occur at the power densities achievable in the current configuration of the instrument. Fig. 3.9 displays images of the light sheet acquired with the 10× objective and intensity profiles across the light sheet (Fig. 3.9 a)). The width of the light sheet could be adjusted by a vertical slit aperture (Fig. 3.9 b) - d)). Blocking the light not illuminating the object field helped to avoid excessive photo-bleaching but also led to refraction artifacts evident as stripes in the light sheet image. By inserting a 5× horizontal beam expander, the light sheet width could be increased from 77,1 µm to 348,4 µm (FWHM) to illuminate a larger object field (Fig. 3.9 f)). Using the scanning mirror sM8 (Fig. 3.1) to pivot the light sheet around the image center reduced shadowing artifacts but did not affect the light sheet width (Fig. 3.9 e)).

Another important aspect in light sheet microscopy is the light sheet thickness as discussed in sec. 1.3.4. The thinner the light sheet, the better the optical sectioning and background suppression, but the larger the divergence angle. Both can be adjusted by the effective numerical aperture used for illumination. For imaging of very large objects with low magnification, lenses C3 and C4 were removed from the illumination path. This led to an underfilled illumination aperture and a light

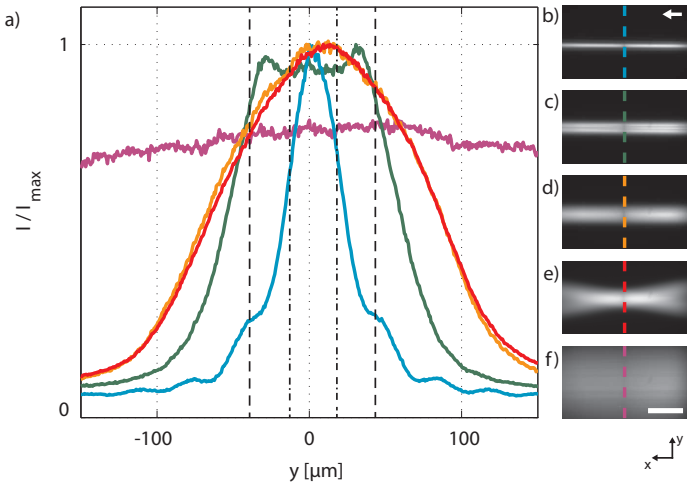

Fig. 3.9: **a)** Width of the light sheet in different configurations. Vertical lines indicate typical fields of view: Ixon DV897 (dashed) and Ixon DU860 (dash-dot), 100× magnification. **b),c)** The width of the light sheet could be reduced by closing a slit aperture. White arrow indicates direction of illumination. **d)** The untruncated light sheet and the light sheet pivoted around the image center (**e)**) had the same width in the center of the object field. **f)** For homogeneous illumination of a larger field of view, a 5× horizontal beam expander was inserted. All values determined for 640 nm illumination. Scale bar, 250 µm.

sheet thickness of 8,7 - 10,8 µm with a Rayleigh length of 358,5 - 408,9 µm (Fig. 3.10 a)) as determined by moving fluorescent beads through the illumination sheet (sec. 2.1.1).
Overfilling the illumination aperture and thus using the full NA resulted in a light sheet thickness of down to 1,7 - 2,2 µm (FWHM) and a Rayleigh length of 11,3 - 28,8 µm depending on the laser line (Fig. 3.10). The object field of the camera slightly exceeded twice the Rayleigh length in some configurations (e.g. object field of 82 µm for Ixon DV897 and 100× magnification). Due to the divergence of the light sheet, optical sectioning and SNR were reduced at the edges of the image. However, practically this did not impede the single molecule detection capability of the instrument.
Chromatic shifts of up to 150 µm occurred between the illumination foci of the various laser lines (Tab. 3.6, Fig. 3.10 b))). They were attributed to the differing beam divergence along the illumination path and aberrations of the singlet lenses in this part of the setup as well as the 2 mm sidewall of the sample chamber.
A better overlap between the foci could be achieved by reducing the distance between lenses C3 and C4 such that the beam became slightly divergent rather than collimated after C4. The additional beam divergence compensated for other chromatic errors. As a result, the chromatic shift was reduced to < 8 µm. This value was smaller than the Rayleigh length of the light sheet (Fig. 3.10 c)).

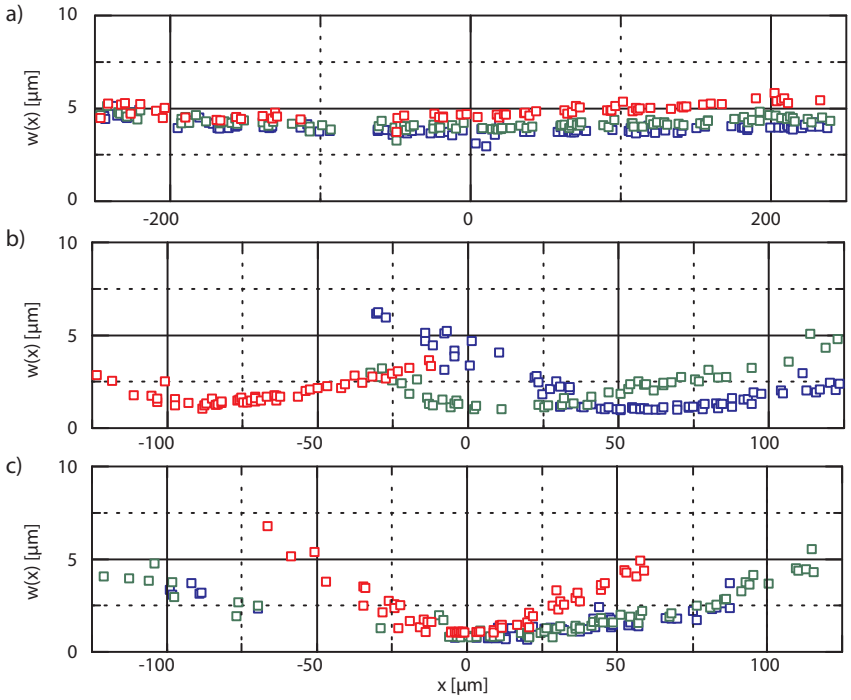

Fig. 3.10: Thickness ($1/e^2$-radius) of the light sheet along the illumination axis in different configurations. **a)** Lenses C3 and C4 removed. **b)** Collimated beam after C4. **c)** Divergent beam after C4. See Tab. 3.6 for residual chromatic errors and light sheet parameters.

Tab. 3.6: Light sheet parameters for different configurations as shown in Fig. 3.10. a) C3 and C4 removed. b) Collimated beam after C4. c) Divergent beam after C4, minimal chromatic shift Δx_0. All parameters and standard errors extracted from fits of eq. 1.1 to data displayed in Fig. 3.10.

configuration	λ_{exc} [nm]	w_0 [µm]	FWHM [µm]	x_R [µm]	Δx_0 [µm]
Fig. 3.10 a)	488	$3{,}69 \pm 0{,}04$	$8{,}7 \pm 0{,}1$	$358{,}5 \pm 9{,}9$	$0{,}0 \pm 5{,}1$
	532	$4{,}04 \pm 0{,}04$	$9{,}5 \pm 0{,}1$	$406{,}7 \pm 9{,}6$	$1{,}7 \pm 6{,}3$
	640	$4{,}57 \pm 0{,}04$	$10{,}8 \pm 0{,}1$	$408{,}9 \pm 17{,}5$	$-111{,}0 \pm 8{,}3$
Fig. 3.10 b)	488	$0{,}91 \pm 0{,}10$	$2{,}1 \pm 0{,}2$	$19{,}2 \pm 2{,}4$	$56{,}4 \pm 1{,}4$
	532	$1{,}11 \pm 0{,}09$	$2{,}6 \pm 0{,}2$	$25{,}0 \pm 2{,}7$	$0{,}0 \pm 1{,}5$
	640	$1{,}37 \pm 0{,}06$	$3{,}2 \pm 0{,}1$	$26{,}7 \pm 1{,}8$	$-97{,}0 \pm 1{,}3$
Fig. 3.10 c)	488	$0{,}88 \pm 0{,}07$	$2{,}1 \pm 0{,}2$	$28{,}8 \pm 2{,}7$	$5{,}6 \pm 2{,}1$
	532	$0{,}74 \pm 0{,}10$	$1{,}7 \pm 0{,}2$	$20{,}4 \pm 3{,}0$	$-1{,}6 \pm 1{,}9$
	640	$0{,}93 \pm 0{,}09$	$2{,}2 \pm 0{,}2$	$11{,}3 \pm 1{,}2$	$0{,}0 \pm 0{,}7$

3.4.3 Detection PSF

The light sheet profile represented the *excitation* PSF of the instrument and led to optical sectioning as well as background suppression. In contrast, the shape of the astigmatic *detection* PSF determined the 3D localization capabilities. Stronger astigmatism leads to a steeper gradient in PSF shape parameters and thus a better axial localization precision on the one hand. On the other hand it results in a larger diameter of the PSF in the effective focal plane, impairing lateral localization precision. The amount of astigmatism introduced by the cylindrical lens in the detection path depended on the refractive power of the lens and its exact position. A larger distance between camera chip and lens resulted in stronger astigmatism. Here, lenses with a focal length of $f = 1000$ mm and $f = 10000$ mm were used. Different types of mounts were developed for convenient placement of the lenses in three different positions immediately above the tube lens ($f = 10000$ mm), in a fixed plane outside the microscope body in the camera C-mount adapter ($f = 10000$ mm), or movable along the detection axis within the camera C-mount adapter and the 2,5× additional magnification ($f = 1000$ mm). The shape of the PSF was strongly affected by the position of the lens and also influenced by the correction ring setting of the 40× detection objective.
In Fig. 3.11 a) - c) the shape of the regular PSF before insertion of the cylindrical lens is characterized. A PSF width of $w_0^{reg} = 183$ nm ($1/e^2$-radius) was determined. The peak height and the width of the PSF were used to identify the focal plane. By sequentially acquiring image stacks of the same multicolor beads with different excitation wavelengths, the amount of chromatic shift in the detection unit could be investigated. Deviations between excitation with different wavelength depended on correction ring settings but were below 200 nm for all configurations (Fig. D.1). However, this observation might partially result from residual sample drift during the acquisition. Chromatic shifts were well below the axial extent of the PSF and the light sheet thickness. Moreover they would only affect results in multi-color 3D localization experiments. Throughout this work, single molecule localization was only performed in a single color channel for each experiment and thus no chromatic corrections applied.
Placing the $f = 1000$ mm cylindrical lens close to the primary image plane between the microscope body and the 2,5× secondary magnification and setting the correction ring to 160 µm coverslip thickness was found to yield the best PSF parameters for accurate 3D tracking. The PSF width in the effective focal plane was slightly increased ($w_0/w_{0,reg} = 1{,}24$). The amount of astigmatism was found to be $a = 812$ nm and similar to the axial extent of the PSF ($w_z = 683$ nm $1/e^2$-radius, Tab. 3.7).
Results for further lens positions are listed in appendix D.

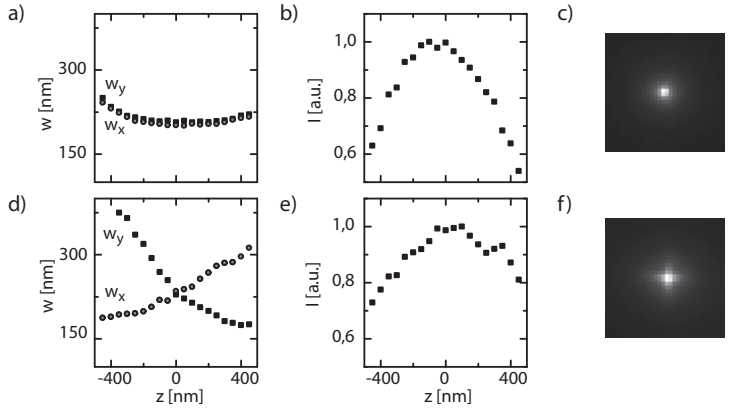

Fig. 3.11: **a)** Width of the regular PSF in x (circles) and y (squares) versus axial position. **b)** Peak height versus axial position indicating the axial extent of the PSF. **c)** Sum projection of the corresponding PSF stack. **d)** For the astigmatic PSF, x and y focal position are axially separated by $a = 812$ nm. **e)** As a consequence, the PSF was broadened axially. **f)** Sum projection of astigmatic PSF stack.

Tab. 3.7: Parameters describing the regular (reg) and astigmatic (ast) PSF shape. c.r.: correction ring setting. a: astigmatism. Additional configurations are characterized in appendix D.

	lens	λ [nm]	c.r. [µm]	$w_{min}^{x/y}$ [nm]	a [nm]	w_0 [nm]	w_0/w_0^{reg}	w_z [nm]
reg	-	640	0.16	183 / 180	39	183	1,00	475
ast	1 m	640	0.16	174 / 207	812	226	1,24	683

3.4.4 Axial detection and tracking range

Unlike in previous works using astigmatic detection for 3D localization [114, 120], a single set of calibration parameters was valid throughout the entire tracking range since a water immersion objective was used and particles were usually tracked in specimen with a refractive index close to that of water. Thus, no refractive index mismatch occurred. Fig. 3.12 b) displays the PSF width determined for several beads detected throughout an image stack covering the full travel range of the piezo stage and a total volume of 82 µm × 82 µm × 100 µm. Axial or lateral position of the beads did not affect the shape of the PSF.
It was thus possible to manually displace an immobilized fluorescent bead and follow its trajectory throughout the full piezo travel range of 100 µm using the same calibration parameters (Fig. 3.12 a)). With a larger travel range, ultimately the objective working distance of 610 µm would become the limiting factor.

The axial tracking range must be distinguished from the axial detection range.

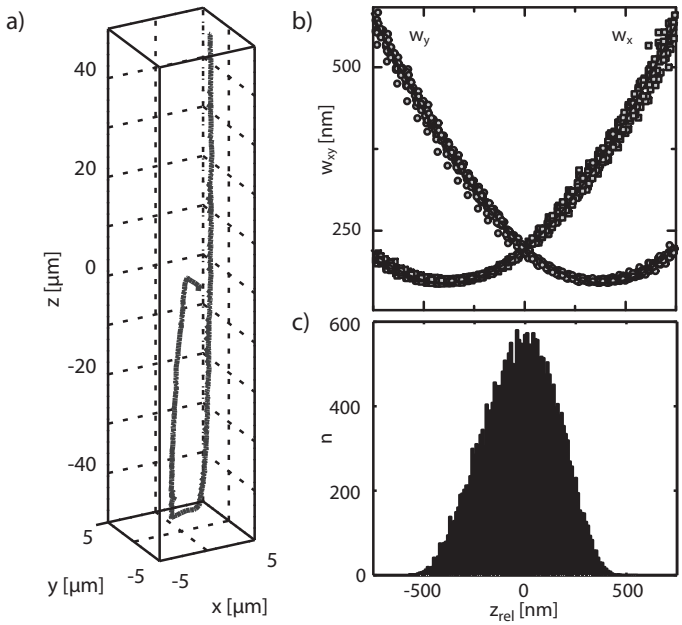

Fig. 3.12: Tracking range and axial detection range. **a)** Trajectory of an immobilized bead manually displaced by ≥ 90 µm. The full travel range of the piezo stage can be used for tracking. **b)** PSF width for $n = 17$ fluorescent beads distributed throughout a volume of 82 µm × 82 µm × 100 µm. **c)** The axial detection range of the setup can be demonstrated by a histogram of axial localizations relative to the focal plane (ATTO647N labeled BR2.1 mRNP in C. tentans salivary gland cell, see section 4.2.4).

The latter describes the axial range around the focal plane, in which single particles can be detected. It results from a combination of decreasing illumination intensity for out-of-focus particles due to the light sheet thickness, depth of field of the detection objective and amount of astigmatism. While bright emitters like fluorescent beads were generally visible over an axial range of several microns, a Gaussian peak was no longer suitable for describing the shape of the PSF at such distances from the focal plane. However, localization based on the diameter of the Airy rings would still be possible for bright emitters [125]. For particles emitting a low number of photons, e.g. single fluorescent dyes, the Airy pattern will typically not be observable. The axial detection range for such particles was determined by histograming the axial localizations of all detected particles in a tracking experiment with the feedback loop turned off (Fig. 3.12 c)). The distribution of axial localizations could be fitted by a Gaussian peak with a width of $w_{ax} = 468 \pm 7$ nm (FWHM).

3.4.5 Axial localization precision

The PSF shape determined the theoretical lateral and axial localization precision. However, the algorithm used to determine the localizations dictates how close experimental values come to the optimal results.
The localization precision was experimentally determined by moving fluorescent beads immobilized in 2% agarose through the focal plane with a step size of 50 nm. 100 frames per stack slice were acquired. Acquisition was repeated at various illumination intensities. In the resulting dataset, particles were localized in each frame using all three *axial* localization schemes presented in sec. 3.2.1 (COM, G2D, XCOR). *Lateral* localization precision values were determined by G2D. The localization precision values for individual beads were determined by calculating the standard deviation of all 100 localizations determined for a slice within the stack (Fig. 3.13 a)). The average number of photons detected per frame was calculated using eq. 2.1. Both, lateral and axial localization precision, are displayed in Fig. 3.13 c) as a function of the number of photons per signal. Only beads located close to the focal plane were considered ($|z_{rel}| \leq 50$ nm).
G2D and XCOR achieved a similar precision over the entire range of 120 to 900 photons per signal, whereas values for COM are twice as high. As expected, lateral localizations were approximately three times more precise than axial localizations.

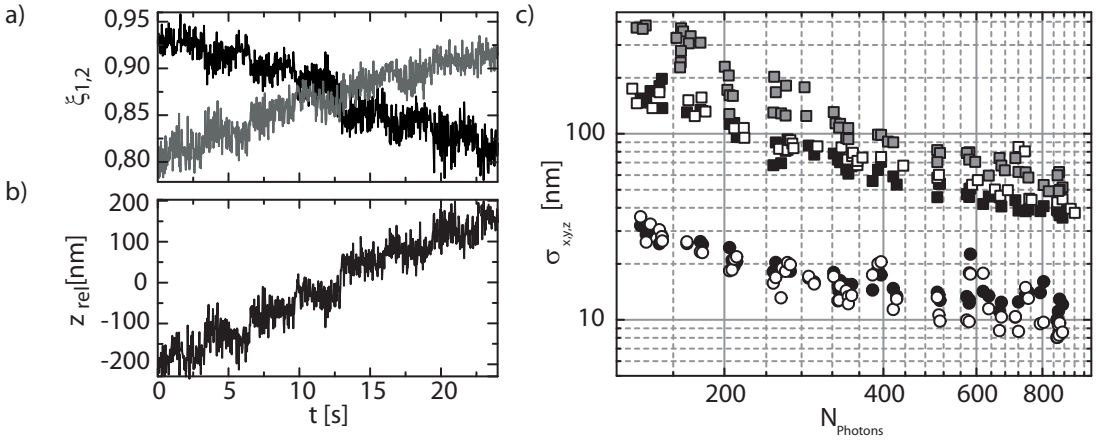

Fig. 3.13: **a)** Normalized covariance values for a bead moved through the focal plane in steps of 50 nm with 100 frames per position as determined by the XCOR method (gray ξ_1, black ξ_2). **b)** Corresponding z coordinates calculated according to eq. 3.12. **c)** Axial localization precision as a function of the number of photons detected for particles with $|z_{rel}| \leq 50$ nm. Experimentally determined values for COM (gray squares), G2D (black squares) and XCOR (white squares). For comparison, the lateral localization precision (G2D) is shown (x - white circles; y - black circles).

3.4.6 Temporal band width

The temporal band width of the method presented here was limited not only by the pure computation time for a 3D localization (Tab. 3.4) and the camera frame rate, but also by the piezo stage response time. According to manufacturer specifications the P-611.ZS piezo stage incorporated in the setup has a resonant frequency of $f_0 \approx 300$ Hz at a load of 35 g. As a rule of thumb, the shortest time for a piezo stage to reach its nominal displacement is $\tau_S \approx 1/(3 \cdot f_0) = 1{,}1$ ms [126]. In practice, the stage was operated in closed loop mode and a controller unit slowed down the expansion of the piezo to prevent overshoot and resonant oscillations. The response time of the piezo stage was experimentally determined as follows: Fluorescent beads were immobilized in 2% agarose and brought to the focal plane. Subsequently, the piezo stage was displaced by 200 nm while imaging at a frame rate of 5,1 kHz by reading out just 36 lines of the Hamamatsu Orca Flash 4.0 chip. The bead displacement resulted in a drop in peak intensity (Fig. 3.14). It was fitted by a logistic decay function with time constant $\tau_S = 1{,}12 \pm 0{,}48$ ms in excellent agreement with expectations.

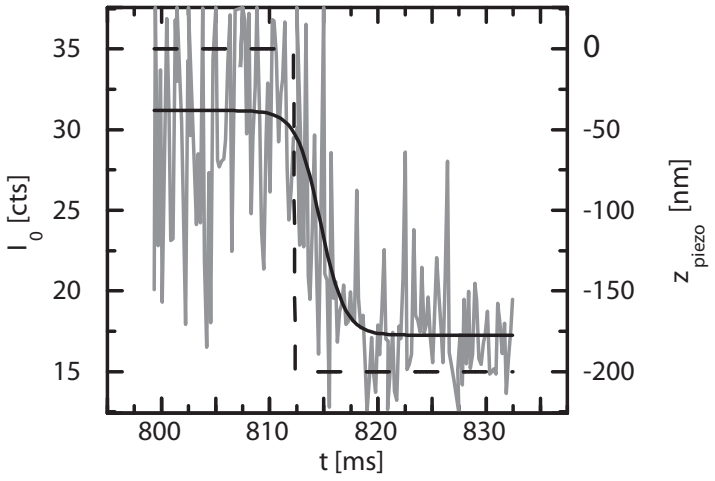

Fig. 3.14: The piezo response time was experimentally determined by observing the drop in peak intensity (gray solid line) upon displacing an immobilized fluorescent bead by 200 nm from the focal plane (piezo position, black dashed line). The intensity change could be fitted by a logistic decay function with time constant $\tau_S = 1{,}12 \pm 0{,}48$ ms (black solid line).

3.4.7 Tracking fluorescent beads in aqueous solution

With the technical aspects of the method characterized, the ability to actively follow diffusive motion was tested by tracking fluorescent beads of various sizes in aqueous solution using the XCOR algorithm. Their diameter ranged from 20 - 500 nm. Exposure times were adjusted according to particle mobility (Tab. 3.8) and the pco.edge camera was used for all experiments to achieve a sufficiently high frame rate. 3D particle trajectories exceeding the static axial detection range by orders of magnitude could be recorded for all types of beads and mobilities. Diffusion coefficients determined from jump distance histograms D_{exp} were in the expected range but did not always agree with theoretical expectations D_{th} according to eq. 1.20. For 20 nm and 100 nm beads, an analysis of the bulk dataset required at least two mobility components D_{exp}, one of which was close to the expected value, whereas the other was either too high (100 nm beads) or too low (20 nm beads). In the latter case this may result from a polydisperse size distribution due to aggregation of particles or swelling of the polymer beads in aqueous buffer leading to a larger hydrodynamic radius.

For each type of beads, a long trajectory was selected and analyzed separately. JD histograms for these trajectories are shown in Fig. 3.15 and were fitted with an unimodal distribution (D_{trj}). In contrast to the bulk data, using a bimodal distribution was not justified by a significantly improved fit. This indicates that the populations in the bulk data analysis resulted from different particle types rather than transitions of single particles between different mobility states.

Tab. 3.8: Tracking results for beads in aqueous solution. Diffusion coefficients for trajectories displayed in Fig. 3.15 (D_{trj}) are compared to results from pooling all trajectories acquired under the same conditions (D_{exp}) and theoretical expectations calculated from eq. 1.20 (D_{th}). $\eta = 0{,}95$ cP, $T = 297$ K.

beads	t_{exp}[ms]	$n_j(n_{trj})$	$D_{th}[\frac{\mu m^2}{s}]$	$D_{exp}[\frac{\mu m^2}{s}]$	$D_{trj}[\frac{\mu m^2}{s}]$
500nm	16,11	17703 (41)	0,453	$0{,}501 \pm 0{,}005$	$0{,}502 \pm 0{,}014$
100nm	5,08	4966 (134)	2,27	$D_1 = 2{,}47 \pm 0{,}03(67\%)$ $D_2 = 6{,}42 \pm 1{,}70(33\%)$	$2{,}58 \pm 0{,}12$
20nm	2,05	54855 (4241)	11,3	$D_1 = 4{,}91 \pm 0{,}42(35\%)$ $D_2 = 10{,}6 \pm 0{,}6(65\%)$	$9{,}4 \pm 0{,}8$

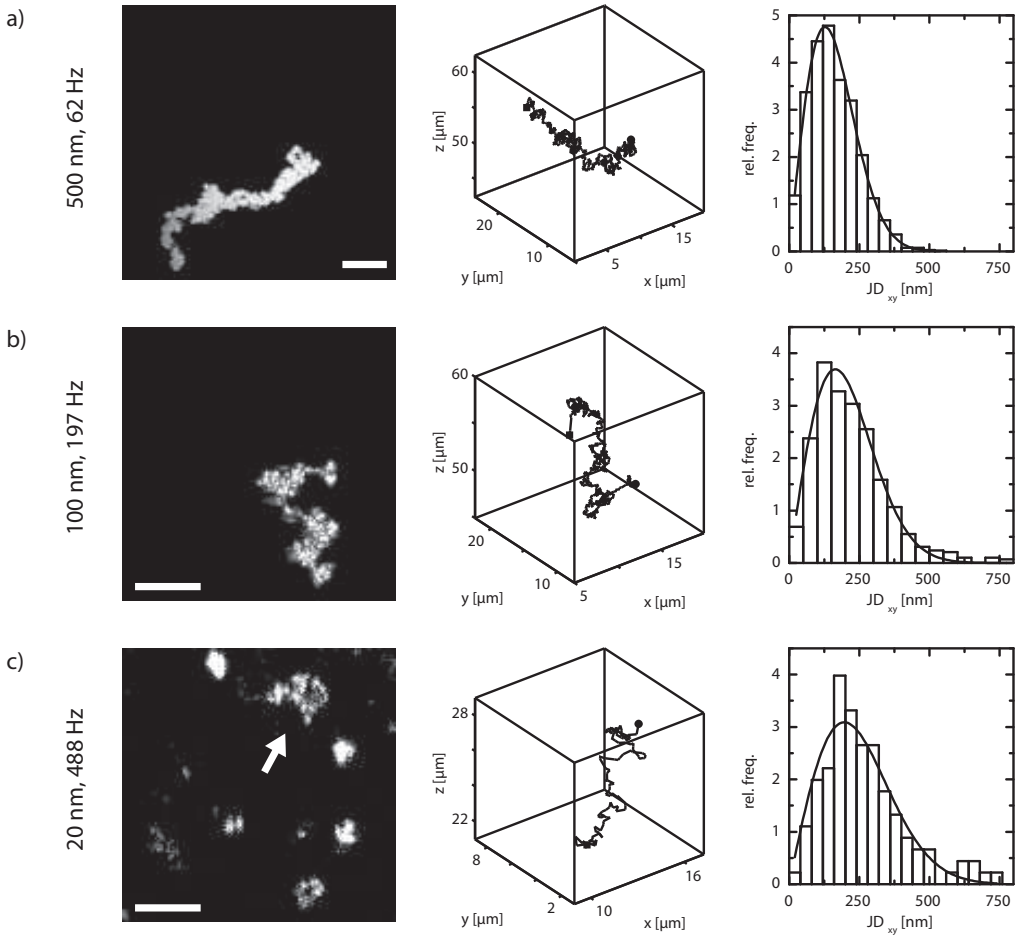

Fig. 3.15: Tracking of fluorescent beads. Exemplary data for fluorescent beads of different diameters are shown. Notably, all trajectories exceeded the axial detection range for static tracking by at least one order of magnitude. Left column: Maximum intensity projection of image frames containing a selected trajectory. Scale bars, 5 µm. Center column: 3D plots of the reconstructed single particle trajectories. Right column: Jump distance histograms (xy) for the trajectories shown here and least squares fit of eq. 1.27. **a)** 500 nm beads diffused slowly in aqueous solution and could be tracked at 62 Hz. The trajectory displayed here consisted of 1668 localizations corresponding to 27 s observation time. **b)** 100 nm beads required faster frame rates for reliable tracking due to their higher mobility. Trajectory of 581 positions acquired at 197 Hz frame rate reflecting an observation time of 3 s. **c)** Even smaller 20 nm beads could be tracked at 200 Hz but reliable tracking required up to 487 Hz frame rate. Trajectory of 114 positions corresponding to 0,25 s observation time.

3.4.8 Tracking at varying signal levels

To demonstrate the capability of tracking particles over a large range of signal-to-noise levels without any modifications to the algorithms or calibration parameters, a fluorescent particle was tracked with the XCOR algorithm in aqueous solution while manually varying the illumination intensity. The number of photons detected from the particle ranged from less than 100 up to more than 10000 per frame of 21 ms (Fig. 3.16).

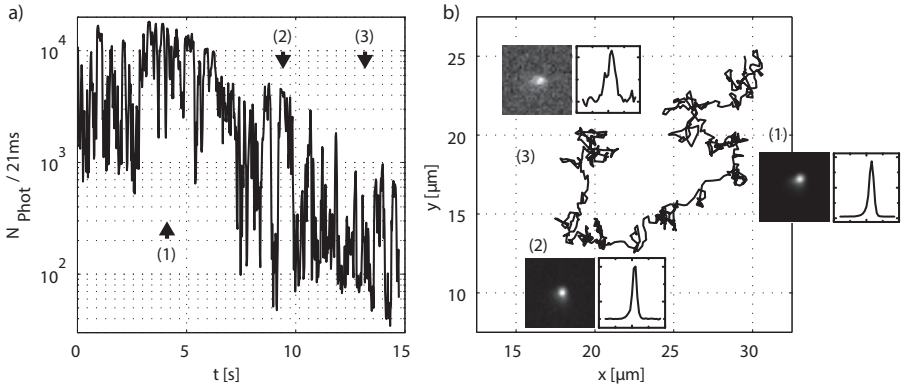

Fig. 3.16: **a)** Number of photons detected per frame of 21 ms throughout the course of the trajectory shown in **b)**. Exemplary PSF images and intensity profiles through the center of the peak are shown.

3.4.9 High frequency tracking in aqueous solution

In a further experiment, fluorescent beads were tracked in aqueous solution at different frame rates with the XCOR algorithm. Using the pco.edge camera, exposure times down to 1,12 ms were achieved, corresponding to the highest possible frame rate for this camera at an image field of 65×65 pixels or $10{,}6 \times 10{,}6$ µm^2 and equaled the piezo response time (sec. 3.4.6). Since exposure times were no more much longer than the piezo response time, the position of the piezo stage could not be assumed to be constant throughout the exposure time anymore. Therefore, axial localizations may have been tampered with motion artifacts. Nevertheless, the instrument was still able to follow the particles. An exemplary trajectory of 925 localizations in 1,04 s is displayed in Fig. 3.17. 2D jump distance and mean square displacement analysis yielded a diffusion coefficient of $D_{JD} = 0{,}54 \pm 0{,}01$ µm^2/s and $D_{MSD} = 0{,}51 \pm 0{,}01$ µm^2/s respectively.
Thus, taking together DLL execution time, piezo response and camera frame rate, the minimum temporal resolution of the method presented here was estimated to be $t_{min} \geq 1{,}1$ ms.

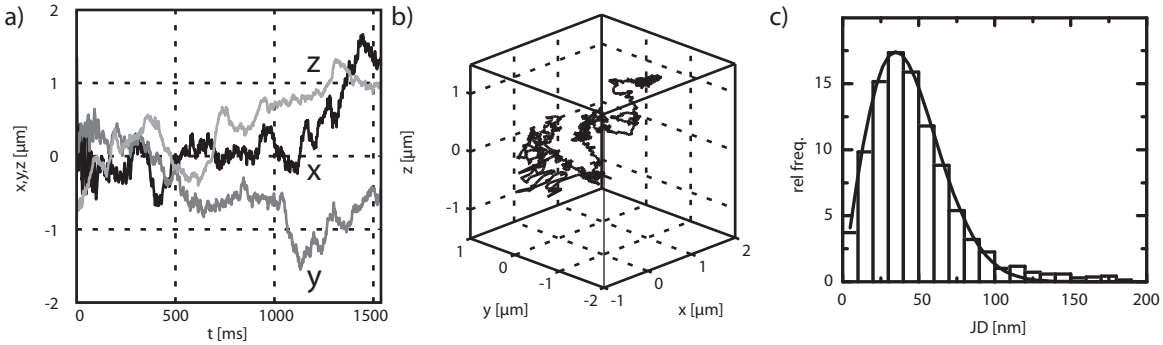

Fig. 3.17: Real-time 3D tracking at very high frame rates. **a)** x (black), y (dark gray) and z (light gray) coordinates of a fluorescent particle in aqueous solution were recorded with 1,12 ms time interval. The axial range of the full trajectory displayed in **b)** exceeds the static axial detection range of the instrument. **c)** 2D jump distance histogram of the trajectory and unimodal fit.

4 Results

4.1 Lipid tracking in GUV membranes

First experimental results were obtained in the biochemical model system of GUVs. Due to their size of several dozen microns diameter, light sheet microscopy was favorable tool for imaging the vesicles. Low amounts of fluorescently labeled lipids were incorporated in the lipid bilayer for single molecule observations. Changing the composition of the lipid bilayer enabled control of lipid mobility in the membrane.
Since lipids were stably incorporated in the GUV membrane, their motion was confined to a spherical surface. Thus, it is immediately clear that recording 2D localizations would not reveal the true particle motion. Since fluorescence was detected from below, the top of a GUV appeared as a nearly flat surface with diffusion occurring in the object plane. However, imaging in areas, in which the GUV surface was inclined with respect to the focal plane, required 3D localizations to analyze the particle motion. On the other hand, the motion had only two degrees of freedom since it was confined to a surface. Thus, particle displacements were calculated from 3D Cartesian coordinates but analyzed using the 2D equations (eq. 1.24, 1.27).
Errors introduced by using Euclidean distances rather than the arc length of the displacements were negligible as long as displacements were much smaller than the GUV radius of 20 - 40 µm.
Background noise in GUV experiments due to unspecific fluorescence signal was minimal ($\sigma_{bg} \approx 1{,}0$ photons/pixel s.d.). By tracking lipids in the upper half of the vesicles, interactions with the solid substrate were avoided.

4.1.1 Single fluorophore observation

GUVs consisting of 90 mol% DPPC and 10 mol% cholesterol were found in the liquid crystal gel phase with minimal lipid mobility at room temperature. The low amount of cholesterol did not disturb the order of the lipid bilayer but facilitated GUV preparation. A fraction of $10^{-6} - 10^{-7}$ mol% Atto647 labeled DPPE was incorporated in the membrane. Fluorescently labeled lipids were well separated spatially due to their low concentration. They were imaged at full laser power with the feedback loop deactivated and $t_{cyc} = 32{,}5$ ms kinetic cycle time to determine the total number of photons detectable from individual dyes before bleaching and verify the presence of lipids carrying only a single dye molecule.
Indeed, typical single step bleaching behavior could be observed (Fig. 4.1). Lipid mobility was negligible and fluorescent particles as well as the entire vesicles remained in a stable position throughout the total experiment duration of 62 s. Single particle localizations were identified in the image data and the number of counts

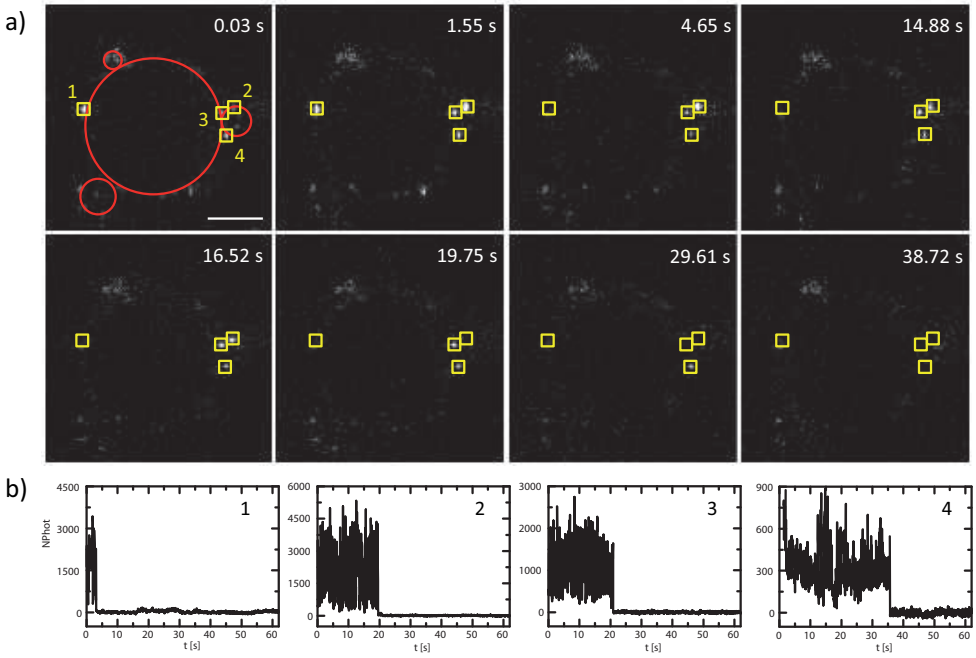

Fig. 4.1: Single step photobleaching. **a)** Frames extracted from a time series of 62 s. Vesicle perimeters are indicated by red circles, emitter localizations by yellow squares. Scale bar 10 µm. **b)** Background-subtracted intensity traces extracted from the regions marked in **a)**. Single fluorophore bleaching steps could be readily identified. Total numbers of photons detected per molecule were (1): $1{,}8 \cdot 10^5$, (2): $1{,}2 \cdot 10^6$, (3): $7{,}6 \cdot 10^5$ and (4): $4{,}2 \cdot 10^5$.

within an area of 11×11 pixel or 1,76 µm $\times$ 1,76 µm around the particle extracted from the time series. Only intensity traces unambiguously showing single step bleaching were selected and considered for the following analysis. The background count level was estimated from the mean intensity after bleaching and subtracted from the intensity trace. Signal counts were converted to photon numbers according to eq. 2.1. On average, $\left\langle \bar{N} \right\rangle = (4{,}7 \pm 0{,}5) \cdot 10^5$ photons per molecule could be detected ($n = 70$ molecules on 16 GUVs). This value was surprisingly high compared to previous reports [57, 127]. However, it is known that the medium surrounding the dye molecule plays a crucial role for its photophysical properties and can e.g. enhance emitter blinking or reduce photobleaching [57, 59]. Here, fluorescent labels were attached to the headgroups of the DPPE lipids and completely surrounded by aqueous buffer irrespective of the phase state of the membrane. The high number of photons detected might thus be attributed to the sugar solutions surrounding the GUV membrane. Another aspect, which can influence the number of photons emitted before bleaching, is the illumination power density. For some fluorescent dyes, a non-linear relationship has been reported with higher power density leading to a lower number of photons emitted [127]. While the exact power density for each

single experiment was difficult to determine due to the inhomogeneous intensity distribution within the light sheet, it can be stated that power densities in subsequent experiments never exceeded the values used here.

4.1.2 Tracking of lipids with low mobility

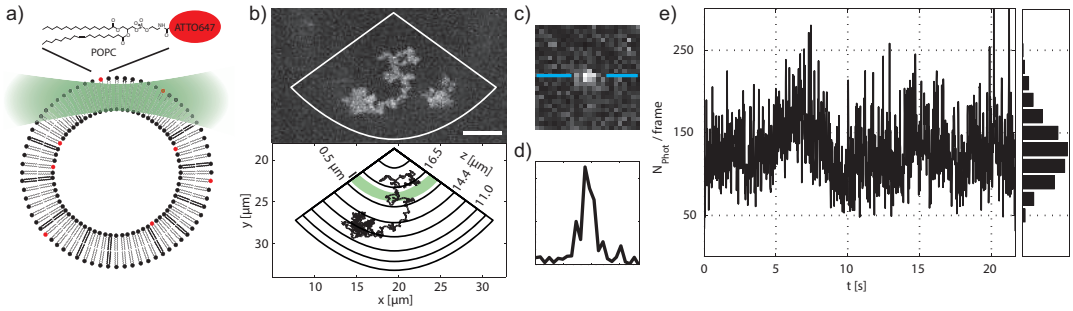

Fig. 4.2: Tracking of POPE-Atto647 in DPPC-cholesterol (50:50) GUVs. **a)** Labeled lipids were incorporated in the GUV bilayer. **b)** Maximum intensity projection of 1354 frames and polar plot representation of the trajectory. Green: Axial detection range without feedback tracking. Scale bar 5 µm. **c)** Typical signal and **d)** intensity profile through the center of the peak. **e)** Number of photons detected per frame.

The amount of cholesterol in the membrane was increased to form GUVs with a composition of 50 mol% DPPC and 50 mol% cholesterol. This prevented the DPPC lipids from arranging in the liquid crystalline phase and thus increased the disorder in the membrane and its fluidity. $10^{-6} - 10^{-7}$ mol% POPE-Atto647 were incorporated in the membrane.
Lipid diffusion within the bilayer was observed with $t_{cyc} = 16$ ms and tracked using the XCOR algorithm. It was possible to follow the random motion of individual lipids and observe trajectories consisting of several hundred localizations. Fig. 4.2 displays one exemplary trajectory containing 1354 localizations corresponding to 21,7 s observation time. The trajectory spanned more than 5 µm in all spatial dimensions. Without feedback tracking, only a small fraction of the localizations could have been obtained since detection would have been limited to an axial range of $\leq$ 0,5 µm as indicated by the green area in the polar plot representation of the trajectory (Fig. 4.2 b)). The exceptionally low background due to light sheet illumination allowed for accurate localization and real-time tracking at just $\langle N \rangle = 130 \pm 38$ photons detected per frame (Fig. 4.2 c)-e)). Local variations in the excitation power density led to low frequency fluctuations in the photon detection rate (Fig. 4.2 e)). The total number of photons detected for this trajectory was $\bar{N} = 1{,}76 \cdot 10^5$, consistent with the results obtained from immobile lipids labeled with the same dye (see sec. 4.1.1).

To determine the diffusion coefficient of the lipid, the MSD was calculated from 3D coordinates and fitted with eq. 1.24. A diffusion coefficient of $D = 0{,}82 \pm 0{,}02$ µm^2/s was obtained from the data (Fig. 4.3 b)). Since the GUV had a radius of ≈ 20 µm and displacements were ≤ 1 µm, artifacts due to the membrane curvature were not observed.

4.1.3 Tracking of lipids with high mobility

The same POPE-Atto647 lipids displayed a significantly higher mobility in GUVs consisting of 100% POPC. Images were acquired at $t_{cyc} = 18{,}2$ ms. On average, $\langle N \rangle = 229$ photons/frame were detected from each dye molecule. A MSD analysis of the exemplary trajectory shown in Fig. 4.3 a) (327 localizations, 5,9 s) yielded a diffusion coefficient of $D = 4{,}2 \pm 0{,}1$ µm^2/s. As expected, the linear shape of the MSD curve indicated Brownian motion of the lipids in the membrane.
A comparison of MSD plots for all three types of GUV (Fig. 4.3 b)) highlights the varying mobility of individual lipids depending on the GUV composition. Diffusion coefficients of $D = 4{,}2 \pm 0{,}1$ µm^2/s and $D = 0{,}82 \pm 0{,}02$ µm^2/s were obtained for the GUVs of POPC and DPPC-cholesterol (50:50) composition respectively. For the quasi-immobile lipids in the DPPC-cholesterol (90:10) GUVs, $D \leq 0{,}007 \pm 0{,}001$ µm^2/s was found.

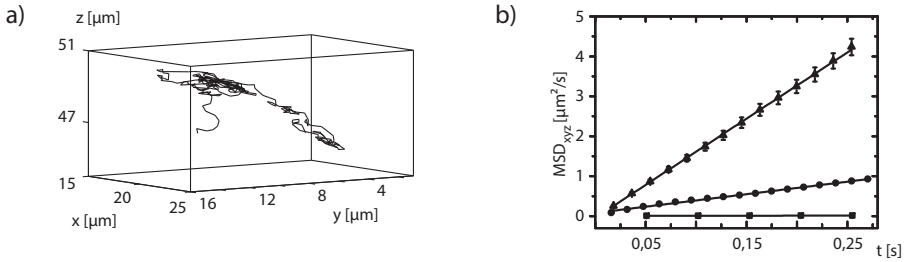

Fig. 4.3: **a)** Trajectory of a POPE-Atto647 molecule in the membrane of a POPC (100%) GUV. 327 localizations in 5,9 s. **b)** MSD$_{xyz}$ plots for the various GUV compositions (squares - DPPC-cholesterol (90:10), circles - DPPC-cholesterol (50:50), triangles - 100% POPC).

4.2 3D SPT in *C. tentans* salivary gland cell nuclei

Diffusion coefficients of BR2.1 mRNPs in *C. tentans* salivary gland cell nuclei were in a similar range as those found for lipids in the GUV membrane in the previous section [109]. However, the background intensity due to autofluorescence and scattered light was higher in biological specimen than in the biochemical model system. Thus, according to eq. 1.18, a higher number of photons had to be detected per signal to achieve the same SNR and a sufficient localization precision. Typically, σ_{bg} = 2-3 photons/pxl (s.d.) was found in the nucleoplasm. Higher values were determined in the cytoplasm as well as where the dense polytene chromosomes introduced aberrations in fluorescence detection and scattered excitation light (see Fig. 4.11).
Reference stainings of DNA and the nuclear envelope were achieved as described in sec. 2.1.6. SYTOX Green bound to DNA and could thus be used to label the polytene chromosome bundles, whereas NTF2-AlexaFluor546 transiently bound to NPCs, resulting in a rim staining of the nuclear envelope. Both, polytene chromosomes and the nucleolus, were found to be devoid of NTF2. At higher concentrations, they could thus be identified as dark areas within the nucleus in the NTF2 detection channel.
As a proof of principle for the applicability of astigmatic 3D SPT *in vivo*, bright fluorescent beads were tracked in *C. tentans* salivary gland cell nuclei (sec. 4.2.1). Furthermore, the characteristics of single particle detection in *C. tentans* salivary gland cell nuclei were investigated. Bleaching kinetics and experimental localization precision values were determined (sec. 3.4).
Subsequently, mRNA and rRNA particles were tracked in *C. tentans* salivary gland cell nuclei. The resulting trajectories with hundreds of localizations per particle allowed for an analysis of mRNA and rRNA trafficking on a single particle basis as well as comparison of individual particle behavior to the ensemble average. Statistical analysis of the trajectories revealed dwell times in a state of low mobility.

4.2.1 Intranuclear tracking of fluorescent beads

In a first *in vivo* experiment, bright fluorescent beads were tracked inside the nuclei of *C. tentans* salivary gland cells. The results presented in this section have been published previously [121].
20 nm diameter red fluorescent beads were microinjected into the nucleoplasm. NTF2-AlexaFluor532 was coinjected to label the nuclear envelope. Using the COM algorithm, individual beads were tracked at t_{cyc} = 51 ms. Trajectories could be obtained throughout the entire nucleus at a sample depth of 120 - 190 µm. Individual

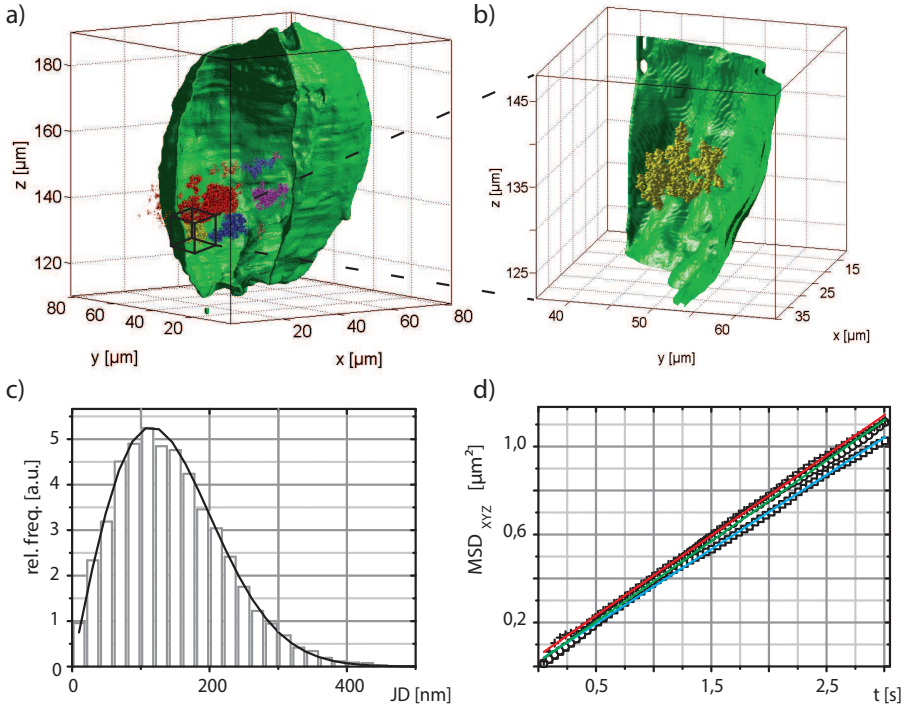

Fig. 4.4: Fluorescent bead trajectories inside a *C. tentans* salivary gland cell nucleus. **a)** Surface rendering of nuclear envelope (green) and particle localizations of five trajectories (colored). **b)** Individual trajectories spanned more than 10 µm in all spatial dimensions. **c)** A jump distance analysis of the trajectory shown in **b)** yielded an unimodal distribution. **d)** 1D MSD plots along x (blue), y (green) and z (red) yielded similar results and agreed with each other.

trajectories consisted of several thousand localizations and spanned $(10\ \mu m)^3$ during several minutes observation time (Fig. 4.4).
On average, $\langle N \rangle = 2130$ photons/frame could be detected from the beads loaded with a high number of fluorescent dye molecules. An analysis of five trajectories indicated Brownian motion with diffusion coefficients of $D = 0{,}18$ - $0{,}25\ \mu m^2/s$ for the individual particles. This variation may be due to different hydrodynamic radii of the particles or inhomogeneities in the viscosity of the nucleoplasm. An analysis of the 1D mean square displacement along x, y and z of a single trajectory comprising more than 4400 localizations (> 220 s observation time) yielded similar diffusion coefficients for each dimension, indicating spatially isotropic Brownian motion (Fig. 4.4 d)). In particular, no systematic deviations between axial and lateral coordinates were introduced by feedback tracking.
The successful application of the method proved the capability to perform 3D tracking of single particles deep inside living tissue with PSF engineering approaches.

4.2.2 Single molecule observation in *C. tentans*

For mRNA and rRNA tracking experiments, oligonucleotides labeled with three Atto647N or Atto647 dye molecules respectively (Tab. A.2) were microinjected into *C. tentans* salivary gland cell nuclei. Typically, 200 - 500 photons per signal were detected from particles labeled with either of the oligonucleotides. The higher number of fluorophores per label allowed the use of lower excitation power densities to achieve a similar photon count rate as compared to labeling with a single fluorophore. Due to the lower laser irradiance, the amount of scattered light and autofluorescence contributing to the fluorescence background was reduced, leading to an increase in SNR and a prolongation of the observation time for labeled particles. The oligonucleotides had a high affinity to their target and were applied in a substochiometric concentration as compared to their target. Thus, unspecific fluorescence background resulting from unbound labels was generally low.
In this section, the emission properties of the labeled particles as well as the resulting localization precision shall be characterized and the detectability of transitions between mobility states demonstrated.

PSF shape deep inside living tissue

In addition to the bead tracking experiments, the applicability of PSF engineering approaches for 3D SPT in biological specimen was further emphasized by a direct comparison of the PSF shape in a low percentage agarose calibration sample to its counterpart inside a *C. tentans* salivary gland cell nucleus. While calibration datasets were obtained from fluorescent beads immobilized in agarose, the biological specimen may introduce additional aberrations, distort the PSF shape and thus impede axial localization.
A z-stack of a *C. tentans* salivary gland cell after intranuclear microinjection of fluorescently labeled oligonucleotides was acquired. By imaging with a kinetic cycle time of $t_{cyc} = 16$ ms, an axial range of 0,6 - 1,0 µm covering a sufficient part of the PSF could be imaged in 0,2 - 0,3 s. Some mRNPs presumably bound to NPCs were found to be immobilized at the nuclear envelope on these timescales and could thus be used to measure the PSF within the specimen.
The PSF obtained from this experiment was compared to a PSF acquired in a sample of fluorescent beads (0,2 µm diameter) embedded in 2% agarose as used for obtaining calibration datasets (Fig. 4.5 a)).
While the SNR was reduced from 400 for the bead to 10-20 for the mRNP due to the smaller number of photons detected per frame, the shape of the PSF remained fairly similar. This was confirmed by plotting the corresponding normalized covariance curves and comparing the relative axial position of the respective particle to the stage position during stack acquisition (Fig. 4.5 b), c)). The lower SNR led

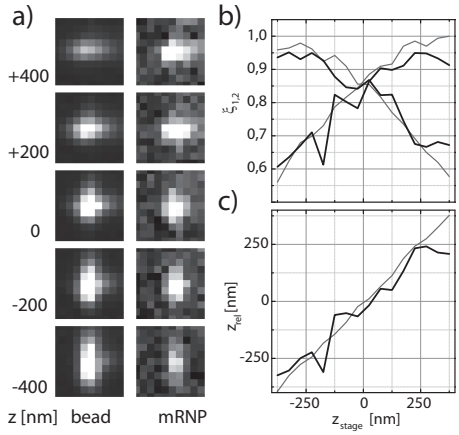

Fig. 4.5: a) Comparison of the PSF obtained from a fluorescent bead in agarose and a mRNP at the nuclear envelope of a *C. tentans* salivary gland cell. **b)** Both yield similar normalized covariance curves and **c)** accurately reproduce the linear stage motion during stack acquisition (bead: gray, mRNP: black).

to stronger fluctuations in the values obtained for the mRNP, but the normalized covariance values as well as the axial position agreed with expectations from the calibration dataset in both cases.
It can thus be concluded that specimen aberrations do not hamper 3D localization by PSF engineering in *C. tentans* salivary gland cell nuclei.

Experimental localization precision

Similarly, the localization precision for particles in *C. tentans* salivary gland cell nuclei could be evaluated using rRNA particles. Immobilization of the particles was frequently observed within the nucleolus and lasted longer than mRNP immobilization at the nuclear envelope. Experimental data from a trajectory of 1118 localizations are shown in Fig. 4.6. A slight linear drift along the y- and z-axis of 7,1 nm/s and -7,4 nm/s respectively occurred over the 17,9 s observation time, whereas the x-position was nearly constant with a drift of 0,9 nm/s. Without drift correction, an experimental localization precision of ($\sigma_x = 31 \pm 7$ nm, $\sigma_y = 59 \pm 9$ nm, $\sigma_z = 114 \pm 19$ nm) was determined by calculating the standard deviation of 11 non-overlapping blocks of 100 consecutive localizations along the trajectory. Real-time tracking was activated during data acquisition and focused on the particle.
Over the course of the trajectory, an average number of $\langle N \rangle = 237$ photons/frame were detected. With a background standard deviation of $\sigma_{bg} = 2{,}6$ photons per pixel, theoretical localization precisions of $\sigma_x^{th} = 26 \pm 6$ nm and $\sigma_y^{th} = 38 \pm 8$ nm (mean $\pm$ s.d.) were determined from eq. 1.18. Whereas the value for σ_x agreed with

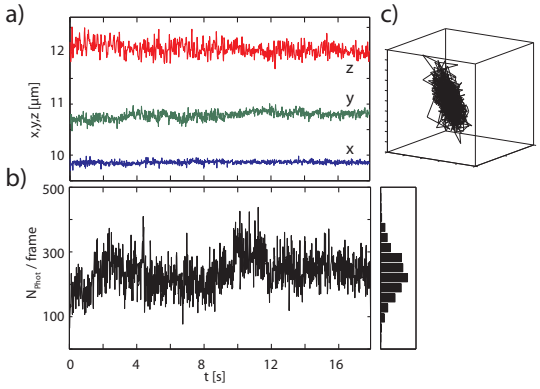

Fig. 4.6: **a)** The intranuclear localization precision was experimentally determined from an immobilized particle. **b)** $\bar{N} = 237$ photons/frame were detected. **c)** During the 17,9 s observation time, slight drift along x and z occurred.

experimental results, the value measured for σ_y was above theoretical expectations. This may in part be due to residual motion of the particle along this direction. The axial localization precision could not be calculated theoretically.
During tracking experiments presented in the following sections, the standard deviation of the background intensity was in a similar range as during the experiment presented here, but photon counts from particles were usually $20 - 100\%$ higher.

Photostability of Atto647N

To determine the number of photons detectable from a labeled mRNP, photobleaching experiments were conducted. Oligonucleotides carrying three Atto647N dye molecules (Tab. A.2) were microinjected into the nucleoplasm of *C. tentans* salivary gland cells at a concentration much higher than for tracking experiments. They bound not only to mRNPs in the nucleoplasm but also to nascent mRNAs virtually immobilized at the BR2 transcription site (Fig. 4.7 a)).
From an area within the transcription site, the total fluorescence intensity was extracted as a function of time under constant laser irradiation. Intensity traces for different excitation power densities J were fitted by an exponential decay function (Fig. 4.7 b)). As expected, the decay constant τ_{bleach} showed a dependency on the excitation power density (Fig. 4.7 c)). Since a unimodal exponential decay was fitted to the data, τ_{bleach} corresponded to the mean time before bleaching.
The photon detection rate from single oligonucleotides at $J \approx 0{,}5$ kW/cm^2 was determined from the distribution of photon counts per signal in tracking experiments and found to be $\langle N \rangle \approx 300$ photons/frame at a kinetic cycle time of $t_{cyc} = 16$ ms.

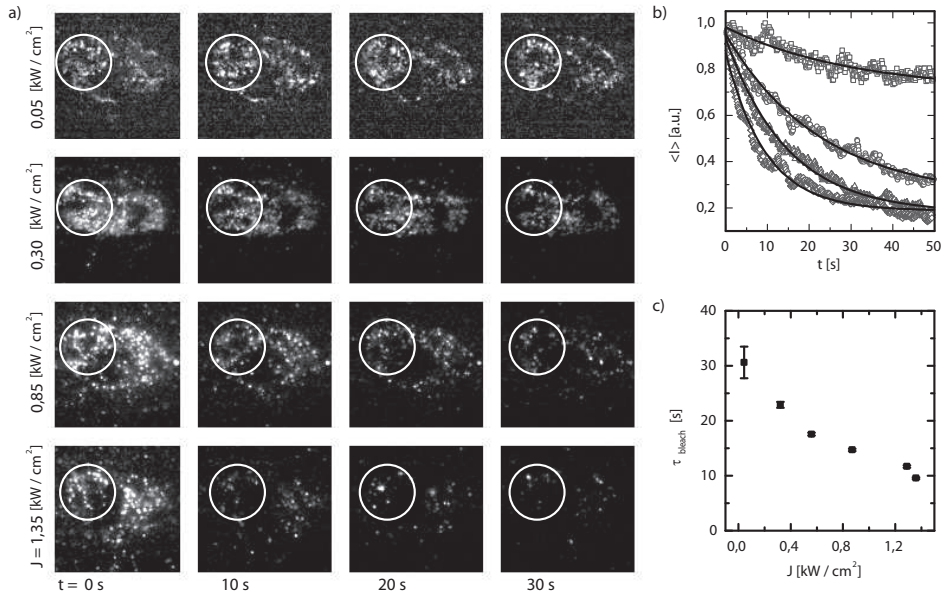

Fig. 4.7: Photobleaching of Atto647N. **a)** Frames extracted from image sequences of 50 s duration and acquired with different excitation power densities in different axial planes of the same *C. tentans* salivary gland cell nucleus. From a region containing oligonucleotides immobilized at the BR transcription site (white circles), intensity traces displayed in **b)** were extracted. All traces were fit by an exponential decay function. **c)** Decay constant as a function of excitation power density J.

From

$$\bar{N} = \frac{\langle N \rangle}{t_{cyc}} \cdot \tau_{bleach} \tag{4.1}$$

the expectation value for the total number of photons detectable from each mRNP can be estimated. With $\tau_{bleach}(J) = 10\,\mathrm{s}$ and the values stated above, $\bar{N} \approx 2 \times 10^5$ photons per oligonucleotide carrying three Atto647N dye molecules.

Photobleaching during feedback tracking

A trajectory of a BR2.1 mRNP labeled with such an oligonucleotide is displayed in Fig. 4.8. It was recorded at $t_{cyc} = 20{,}3$ ms in the nucleoplasm *C. tentans* salivary gland cell using the XCOR algorithm. Over the 4,7 s course of the trajectory, 232 localizations of the particle were obtained. The mRNP was observed over an axial range of $\Delta z > 5$ µm, more than one order of magnitude larger than the axial detection range. On average, $\langle N \rangle = 368$ photons/frame were detected from this mRNP, resulting in a total number of $\bar{N} = 0{,}85 \cdot 10^5$ photons.
After 4,1 s the photon count rate dropped to a value of approximately $\frac{1}{2}\langle N \rangle$. This

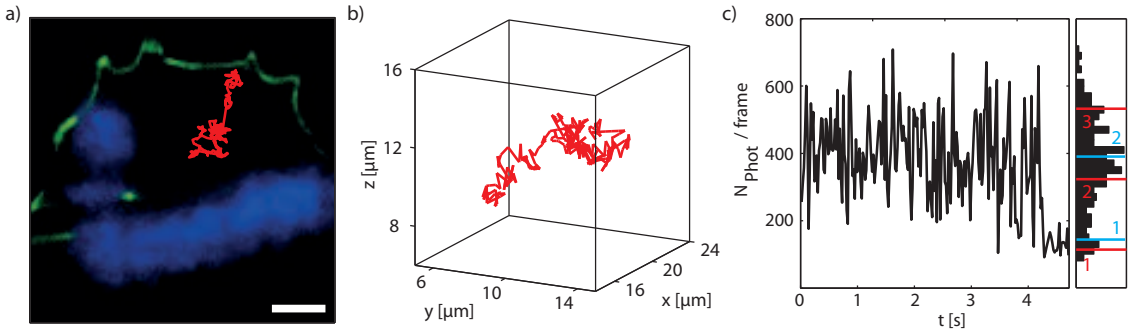

Fig. 4.8: BR2-mRNP diffusion in the nucleoplasm of a *C. tentans* salivary gland cell nucleus. **a)** Overlay image reconstructed from two reference stacks acquired before the tracking experiment. Green: Nuclear envelope (NTF2-AlexaFluor546 staining). Blue: Polytene chromosomes (Sytox Green staining). Red: Trajectory plot. Scale bar 5 µm. **b)** 3D reconstruction of the trajectory. **c)** On average, $\langle N \rangle = 368$ photons/frame were detected. The reduced photon detection rate after 4,1 s may result from bleaching of one of the fluorophores. From the photon count histogram, it cannot be identified if two (blue lines) or three fluorophores (red lines) contributed to the signal.

might indicate bleaching of one or two of the three dye molecules attached to the mRNP. Both interpretations, either a single bleaching event after 4,1 s reducing the number of photons detected per frame from 400 to slightly below 200 ($2 \rightarrow 1$) or transitions between states of 1 to 3 emitting fluorophores ($3 \leftrightarrow 2 \leftrightarrow 1$) with average photon count levels of 540, 360 and 180 photons/frame would be in agreement with the recorded histogram (Fig. 4.8 c)).
The total number of photons detected, $\bar{N} = 0{,}85 \cdot 10^5$ photons, is smaller than the value calculated from eq. 4.1 but of the same order. Photobleaching is an independent stochastic process for all of the three dye molecules. During tracking, already bleaching of a single dye molecule can cause the brightness of the particle to drop below the detection threshold for tracking. Bleaching steps could usually not be identified in the trajectories.

Trajectory length distribution

As previously mentioned, the 3D feedback tracking approach presented here can expand the information gained from standard tracking experiments by detection of trajectories with significantly increased duration. This becomes evident if the trajectory length distribution after the post-processing evaluation is compared between a standard, static and a feedback tracking dataset (Fig. 4.9). Both contain a high number of short trajectories which are usually analyzed in an ensemble evaluation. The length of the short trajectories followed the same distribution for both

datasets and could be approximated by an exponential decay curve with time constant $\tau = 180$ ms. The feedback tracking dataset, however, contained trajectories with exceptionally high numbers of localizations, which were not present in the standard dataset. These trajectories enabled the comparison of individual particles to the entire trajectory ensemble. In contrast to the mere mobility fractions, transitions between these states are much more likely to be directly observed and identified in such long trajectories. In this regard, long trajectories obtained by feedback tracking can carry additional information as compared to common ensembles of short trajectories.

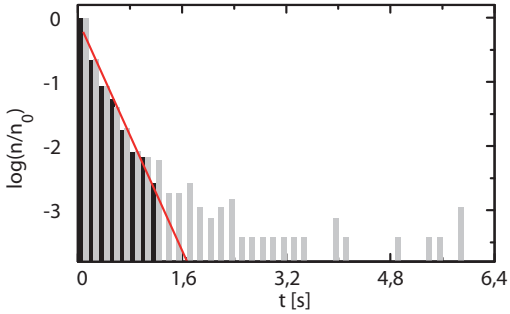

Fig. 4.9: Trajectory length distribution histogram (binning 80 ms). Normalized values for a static 2D (black) and a dynamic 3D experiment (gray) performed on the same sample. Both distributions could be described by the same exponential fit (red line). However, the 3D dataset contained a fraction of trajectories with extremely long duration, which were not present in the 2D dataset.

4.2.3 State transitions and dwell time analysis in long trajectories

An example for such transitions between states of different mobility was observed while tracking ribosomal RNA (rRNA) particles (rRNPs). Oligonucleotides targeting the 28s subunit of the rRNA were microinjected into *C. tentans* salivary gland cell nuclei. The oligonucleotides carried three Atto647 dye molecules. NTF2-AlexaFluor546 was co-injected to fluorescently label the nuclear envelope and identify the nucleolus by its negative image contrast. Particles were tracked using the XCOR algorithm at a kinetic cycle time of $t_{cyc} = 16{,}5$ ms. Immobilization events were observed not only in the nucleolus but also throughout the nucleoplasm whereas a presumably freely diffusing component of high mobility was the most frequent fraction in the nucleoplasm.
Fig. 4.10 shows an exemplary trajectory of 221 localizations. The particle was initially in a mobile state and diffused in the nucleoplasm. Subsequently it traveled along the nucleolus and its motion was halted at two sites on the outer edge of the

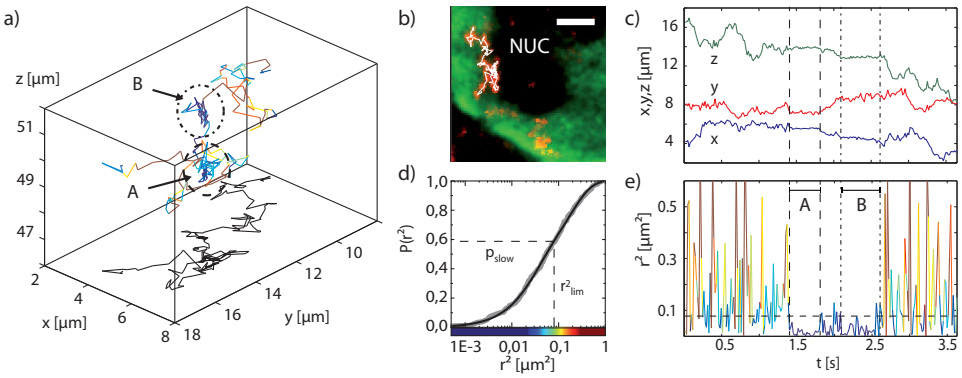

Fig. 4.10: rRNA mobility at the nucleolus. **a)** 3D plot of an rRNA trajectory. See **d)** for color-code. Immobilization events A and B are marked. **b)** Overlay of reference signal (NTF2-AlexaFluor546, green), rRNA signal maximum intensity projection (red) and 2D projection of the trajectory (white). NUC: nucleolus. Scale bar, 2 µm. **c)** x (blue), y (green) and z (red) coordinate as a function of time. **d)** Cumulative squared jump distance distribution (gray) and two component fit (black). **e)** Squared lateral jump distances as a function of time. Color-coded according to **d)**. For both dwell times, $p < 10^{-4}$.

nucleolus before it returned to the mobile state.

While the dwell times were readily identified by visual inspection of the image sequence or by plotting the squared displacement $r^2(t)$ as a function of time and setting a threshold r^2_{lim} (Fig. 4.10 e)), their significance could be confirmed by an analysis according to sec. 2.1.7. Since lateral localizations had better localization precision, only lateral coordinates were analyzed here.

From $r^2_{lim} = 0{,}080\ \mu m^2$ and the cumulative distribution of squared displacements, $P(r^2)$, it was found that a relative fraction of $p_{slow} = P(r^2_{lim}) = 0{,}5773$ of the squared displacements were smaller than r^2_{lim} (Fig. 4.10 d)). The dwell times in the immobile state indicated in Fig. 4.10 c) and d) had durations of $k_A = 26$ and $k_B = 28$ frames or 429 ms and 462 ms respectively. According to eq. 2.17, the probabilities to observe dwell times below r^2_{lim} of duration k_A and k_B if the squared displacements were drawn randomly from the distribution $P(r^2)$ are $p(k_A) = 5{,}2 \cdot 10^{-5}$ and $p(k_B) = 1{,}7 \cdot 10^{-5}$ respectively. Thus, both dwell times show highly significant deviations from stochastic behavior with p-values $p(k_A)$ and $p(k_B)$.

A fit to the cumulative squared jump distance distribution (Fig. 4.10 d)) yielded two components of $D_1 = 0{,}41 \pm 0{,}01\ \mu m^2/s$ $(41 \pm 1\%)$ and $D_2 = 2{,}87 \pm 0{,}04\ \mu m^2/s$ $(59 \pm 1\%)$. However, during the phases of immobilization, particle motion was reduced almost to the limit of localization precision. During the first dwell time, localizations scattered with $\sigma_x = 68$ nm, $\sigma_y = 82$ nm, $\sigma_z = 115$ nm (s.d.) or approximately twice the values found for the experimental localization precision (see Fig. 4.6). From these values, an immobile fraction with residual diffusion coefficient $D_{immobile} = (\sigma_x^2 + \sigma_y^2)/(4\Delta t) \approx 0{,}07\ \mu m^2/s$ would be expected. This degree

of immobilization is not accurately reflected by the value of D_1. However, using a three component model did not significantly improve the goodness of fit and was thus not justified.

4.2.4 Ensemble analysis of mRNP trajectories

With the scope of single particle tracking in *C. tentans* salivary gland cell nuclei defined by the experiments presented above, BR2.1 mRNP mobility could be studied in detail. In the following sections, intranuclear BR2.1 mRNP trafficking shall first be analyzed on the basis of a classical trajectory ensemble. Subsequently, exemplary long trajectories obtained by real-time 3D SPT shall be analyzed and related to the ensemble data.
To characterize the mobility of BR2.1 mRNPs in general, a jump distance analysis was employed. A dataset of 21533 particle displacements in 1243 trajectories was recorded in a single nucleus. 40000 frames were acquired at a kinetic cycle time of $t_{cyc} = 20{,}3$ ms and with 3D SPT (XCOR) activated. To gain additional insight, two subsets were extracted from the full dataset by spatial filtering. The first one contained only trajectories, which were separated from both, polytene chromosomes and the nuclear envelope, by several microns. The second one contained trajectories in closer proximity to the nuclear envelope. The position of both, a polytene chromosome (PC) and the cytoplasm (CYT) was identified in an average projection of all frames in the series smoothed by a Gaussian kernel. The average background count level was 1120 counts in the nucleoplasm, 1140 counts at the PC position and 1180 counts in the cytoplasm, enabling discrimination of these cellular features (Fig. 4.11 a)). The background noise in single unfiltered frames was $\sigma_{bg} = 102$ counts and typical mRNA signals had an amplitude of $1000 - 1500$ counts above background. Subset regions were chosen to not overlap with the polytene chromosome or the cytoplasm.

Tab. 4.1: Ensemble jump distance analysis and spatially refined analysis of mobility fractions. NP: Nucleoplasm. NE: Nuclear envelope. n_{disp}: Number of displacements. n_{trj}: Number of trajectories. $D_1^{ens} = 0{,}046$ µm^2/s, $D_2^{ens} = 0{,}26$ µm^2/s, $D_3^{ens} = 1{,}37$ µm^2/s, $D_4^{ens} = 4{,}4$ µm^2/s.

data	n_{disp}	n_{trj}	$a_1\,(D_1^{ens})$	$a_2\,(D_2^{ens})$	$a_3\,(D_3^{ens})$	$a_4\,(D_4^{ens})$
NP	14877	760	$0{,}0 \pm 0{,}3\%$	$1{,}8 \pm 0{,}8\%$	$76{,}9 \pm 3{,}4\%$	$21{,}9 \pm 3{,}7\%$
NE	6656	483	$3{,}5 \pm 0{,}7\%$	$34{,}0 \pm 0{,}9\%$	$43{,}1 \pm 2{,}8\%$	$19{,}3 \pm 2{,}6\%$
all	21533	1243	$0{,}7 \pm 0{,}4\%$	$11{,}6 \pm 0{,}8\%$	$66{,}2 \pm 3{,}2\%$	$21{,}4 \pm 3{,}3\%$

A global fit to jump distance histograms of both subsets revealed spatial variations in mRNP mobility. Since lateral localizations had better localization precision,

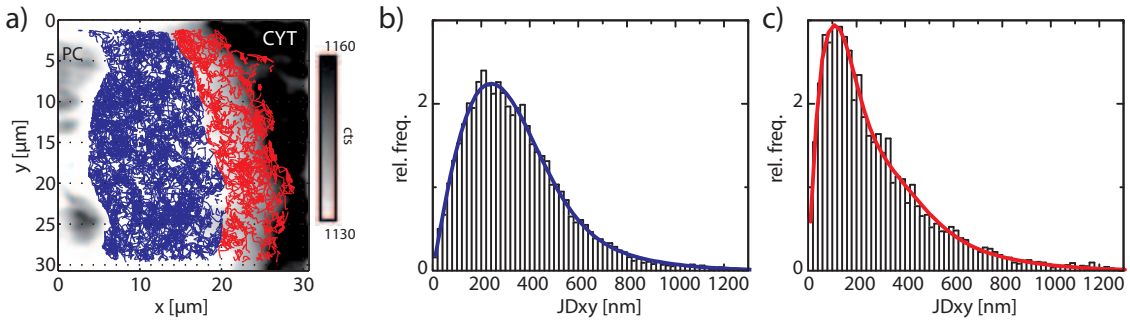

Fig. 4.11: Global fit results for mRNA mobility in a single nucleus. **a)** Trajectories were split into subsets representing particles in the nucleoplasm (blue) or in proximity of the nuclear envelope (red) and plotted on top of an average projection of the series (see main text). **b)** Lateral jump distance distribution of the nucleoplasm subset and **c)** the nuclear envelope subset. Both histograms were fitted with the same set of diffusion coefficients (Tab. 4.1).

only lateral coordinates were analyzed here. Trajectories containing at least five localizations were included in the analysis. Four components were required to accurately reproduce the jump distance distributions in the nucleoplasm subset, the nuclear envelope subset and the complete dataset. Their amplitude varied significantly between particles in the nucleoplasm and at the nuclear envelope. Results are summarized in Tab. 4.1. A very slow fraction of $D_1^{ens} = 0{,}046 \pm 0{,}009$ µm^2/s found at the nuclear envelope but not in the nucleoplasm was attributed to immobile particles. A fraction of low mobility $D_2^{ens} = 0{,}26 \pm 0{,}01$ µm^2/s was also almost exclusively found at the nuclear envelope but not in the nucleoplasm. The third, more mobile component with a diffusion coefficient $D_3^{ens} = 1{,}37 \pm 0{,}05$ µm^2/s accounted for the largest fraction in both subsets. Finally, the fourth population with a very high diffusion coefficient of $D_4^{ens} = 4{,}4 \pm 0{,}5$ µm^2/s was equally abundant in both subsets and attributed to unspecific signals of unbound oligonucleotides.
Similar values for the diffusion coefficients were also found in previous reports under PBS incubation (0,015 µm^2/s, 0,24 µm^2/s, 0,7 µm^2/s and 4,0 µm^2/s; Tab. 2 in [9]) and under incubation with hemolymph (0,001 µm^2/s, 0,5 µm^2/s and 1,4 µm^2/s; Tab 3.6 in [109]).

4.2.5 Single trajectory analysis of mRNP trafficking

Long trajectories obtained by 3D feedback tracking allowed for a more detailed analysis of intranuclear mRNA trafficking. A number of exemplary trajectories selected from feedback tracking datasets are presented in the following sections to highlight the additional insight gained from the analysis of long trajectories.

1. Mobility variations between individual mRNPs in the nucleoplasm

Fig. 4.12 displays one particularly long trajectory from the same nucleus. 769 observations were obtained resulting in an observation time of 15,6 s at a temporal resolution of $t_{cyc} = 20{,}3$ ms. The axial extent of the trajectory ($\Delta z = 8{,}4$ µm) exceeded the static axial detection range by more than one order of magnitude. An average of $\langle N \rangle = 265$ photons/frame were detected throughout the trajectory, resulting in a total number of $\bar{N} = 2{,}03 \cdot 10^5$ photons detected from the particle. This is in agreement with the results presented in sec. 4.2.2 (eq. 4.1).

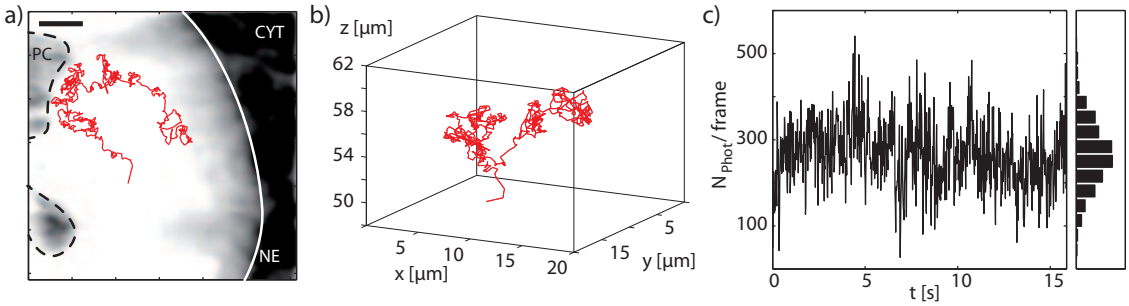

Fig. 4.12: BR2-mRNP diffusion in the nucleoplasm of a *C. tentans* salivary gland cell nucleus. **a)** Overlay trajectory data and reference data as in Fig. 4.11. Scale bar 5 µm. **b)** 3D reconstruction of the trajectory. **c)** Number of photons detected per signal over the course of the trajectory.

In the same dataset, ten trajectories comprising more than 200 localizations each were found (Fig. 4.13 a)). Their characteristics are listed in Tab. 4.2. As discussed above, the average total number of $(0{,}9 \pm 0{,}5) \cdot 10^5$ photons detected per labeled particle was lower than what could be expected from photobleaching experiments, presumably because particles were already lost after bleaching of one or two dye molecules.

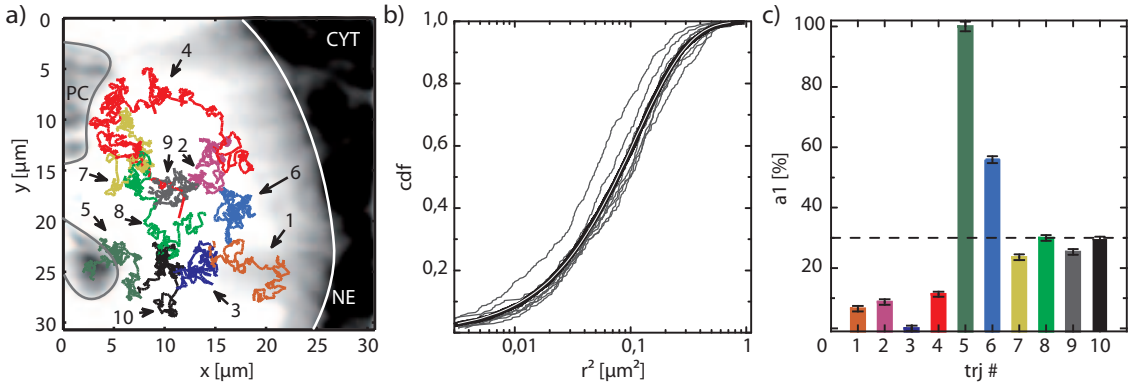

Fig. 4.13: Analysis of ten trajectories with $n_{loc} > 200$. **a)** Distribution of trajectories listed in Tab. 4.2. Numbers indicate trajectory indices. **b)** Cumulative jump distance plots for all trajectories (gray) and fit to the pooled data of all trajectories (black). **c)** Relative fraction of the slower component in each of the trajectories as determined by a global fit with $D_1 = 0{,}85 \pm 0{,}01$ µm^2/s and $D_2 = 1{,}69 \pm 0{,}01$ µm^2/s. Individual results deviate strongly from the result for the pooled data $a_1 = 30{,}0 \pm 0{,}9\%$ (dashed line).

Tab. 4.2: Analysis of long trajectories from a single nucleus. n_{loc}: number of localizations, Δt: trajectory duration, $\bar{N}$: total number of photons detected, a_1: fraction of D_1.

#	n_{loc}	Δt [s]	$\bar{N}$[10^5photons]	a_1[%]
1	216	4,4	0,6	$6{,}5 \pm 0{,}9$
2	242	4,9	0,5	$8{,}7 \pm 0{,}9$
3	210	4,3	0,5	$0{,}0 \pm 0{,}9$
4	769	15,6	2,0	$11{,}3 \pm 0{,}8$
5	385	7,8	1,4	$100{,}0 \pm 1{,}6$
6	348	7,1	0,7	$55{,}9 \pm 1{,}1$
7	253	5,1	0,5	$29{,}9 \pm 1{,}0$
8	362	7,4	0,7	$23{,}6 \pm 0{,}9$
9	246	5,0	0,6	$25{,}3 \pm 1{,}0$
10	309	6,3	1,0	$29{,}4 \pm 1{,}0$
all	3340	∅ 6,8	∅ $0{,}9 \pm 0{,}5$	$30{,}0 \pm 0{,}9$

Cumulative jump distance distributions for all trajectories (Fig. 4.13 b)) were fitted globally with a two component model yielding diffusion coefficients $D_1 = 0{,}85 \pm 0{,}01$ µm^2/s and $D_2 = 1{,}69 \pm 0{,}01$ µm^2/s. A unimodal was not sufficient to describe the data whereas a three component model resulted in two fractions of the same diffusion coefficient.

Notably, the fraction a_1 of the slower component varied from 0% to 100% with a value of $30{,}0 \pm 0{,}9\%$ obtained for the pooled data of all ten trajectories (Fig. 4.13 c)). The high value of $a_1 = 100{,}0 \pm 1{,}6\%$ found for trajectory # 5 may be

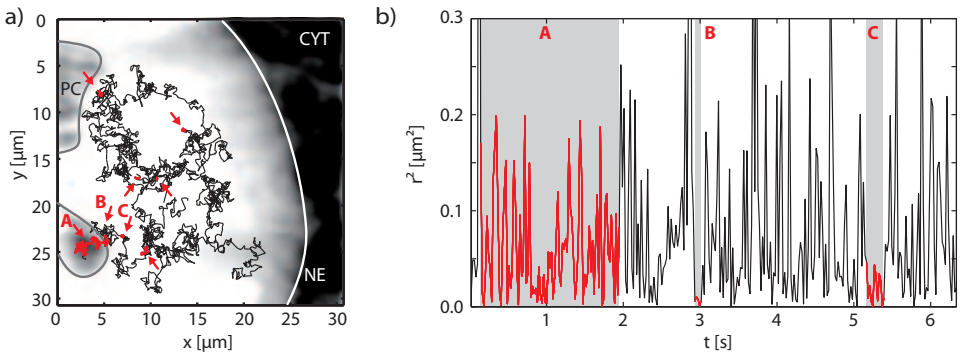

Fig. 4.14: BR2.1 mRNP states of low mobility. **a)** An analysis individually conducted for all ten trajectories shown in Fig. 4.13 (black) yielded a few significant dwell times in a state of lower mobility (red). **b)** Squared displacement as a function of time for trajectory # 5. A long phase of low mobility (A) was identified in the first 2 s of the trajectory while it overlapped with a polytene chromosome. Two additional short phases of low mobility occurred while the particle was diffusing through the nucleoplasm (B,C).

attributed to unspecific interactions with the polytene chromosome reducing the mobility of the particle. All other trajectories were well separated from both, the polytene chromosome and the nuclear envelope.
A search for dwell times in a state of low mobility over the entire range of threshold values $0 \leq r^2_{lim} \leq \max(r^2)$ in each trajectory supported this hypothesis. Each of the dwell times marked in Fig. 4.14 a) represents a sequence of short jump distances with a probability $p < 0{,}05$ to result from a stochastic process described by the jump distance distribution of the respective trajectory (eq. 2.17). Dwell times were characterized by the absence of large particle displacements. While a few stochastically significant events of 100 - 300 ms duration were found throughout the nucleoplasm in some of the trajectories, one prominent phase of 1,6 s duration was identified where trajectory # 5 overlapped with the position of the polytene chromosome (Fig. 4.14). These observations are in agreement with previous findings postulating transitions between states of different mobility on very short timescales [18, 109].

2. mRNP immobilization close to the nuclear envelope

In further experiments, mRNP trajectories were recorded close to the nuclear envelope. Particles were again tracked with the XCOR algorithm and with a kinetic cycle time of $t_{cyc} = 16{,}5$ ms. Fig. 4.15 shows a trajectory recorded at a distance of approximately 2 µm from the nuclear envelope and 10 µm from a polytene chromosome. It comprised $n_{loc} = 114$ localizations during 1,9 s.
A fit to the cumulative squared jump distance distribution (Fig. 4.16 c)) yielded

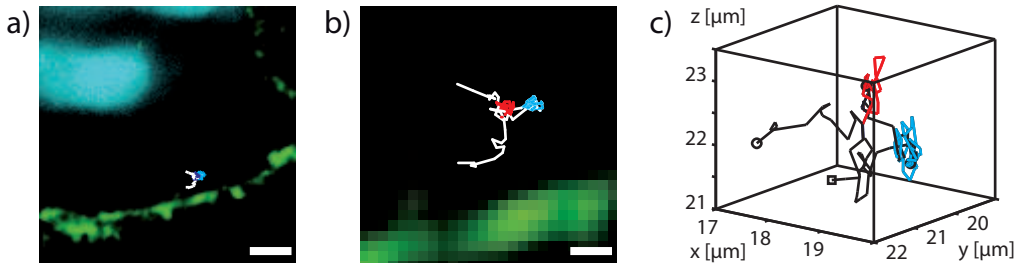

Fig. 4.15: **a)** Overlay of reference information (green: nuclear envelope, cyan: polytene chromosomes) and 2D projection of trajectory data. Scale bar 5 µm. **b)** Magnified view. Colored portions of the trajectory were found to display a mobility much lower than the average value. Scale bar: 1 µm. **c)** 3D plot of the trajectory with states of low mobility indicated (see Fig. 4.16). A circle indicates the first and a square the last localization.

an immobile component $D_1 = 0{,}025 \pm 0{,}005$ µm^2/s with a relative fraction of 14,2 ± 1,3% and a component $D_2 = 0{,}38 \pm 0{,}01$ µm^2/s of low mobility with a relative fraction of 85,8 ± 1,1%, resembling the first two components $D_1^{ens} = 0{,}046$ µm^2/s and $D_2^{ens} = 0{,}26$ µm^2/s of the ensemble analysis (Tab. 4.1).
While mRNPs in the nucleoplasm displayed a relatively high and uniform mobility, diffusive motion was interrupted by phases of extremely low mobility in this trajectory. The particle seemed to be immobilized in two places. To determine dwell times at the putative immobilization sites, the squared displacement of the particle was plotted as a function of time. Again, due to the smaller localization precision, only lateral displacements were considered. The duration was determined, for which the squared displacement stayed below a threshold of $r_{lim}^2 = 0{,}047$ µm^2. Dwell times of $k_1 = 18$ and $k_2 = 49$ frames or 297 ms and 809 ms respectively were found (Fig. 4.16 a)).
To test if such immobilization events can be expected to occur in jump distance sequences randomly drawn from the experimental jump distance distribution, a Bernoulli trial analysis according to sec. 2.1.7 was employed. A fraction of $p_{short} = P(r_{lim}^2) = 0{,}8319$ of the $n' = 113$ squared displacements was smaller than r_{lim}^2. From eq. 2.17, p-values of $p(k_1, n', p_{short}) = 0{,}5001$ and $p(k_2, n', p_{short}) = 0{,}0014$ were calculated. The p-values stated here indicate how likely it is to observe sequences of k_1 and k_2 consecutive jump distances $r^2 < r_{lim}^2$ if the n' jump distances are drawn randomly from the experimentally determined distribution $P(r^2)$ for this one trajectory.
While $k_1 = 18$ appeared to be an immobilization event by visual inspection, it was statistically not significant but would occur in every second sequence of jump distances drawn from $P(r^2)$. In contrast, the second dwell time with $k_2 = 49$ can be considered a statistically very significant event since it would occur in less than two out of 1000 of such sequences.
It is important to note that $P(r^2)$ was determined from the trajectory itself. The

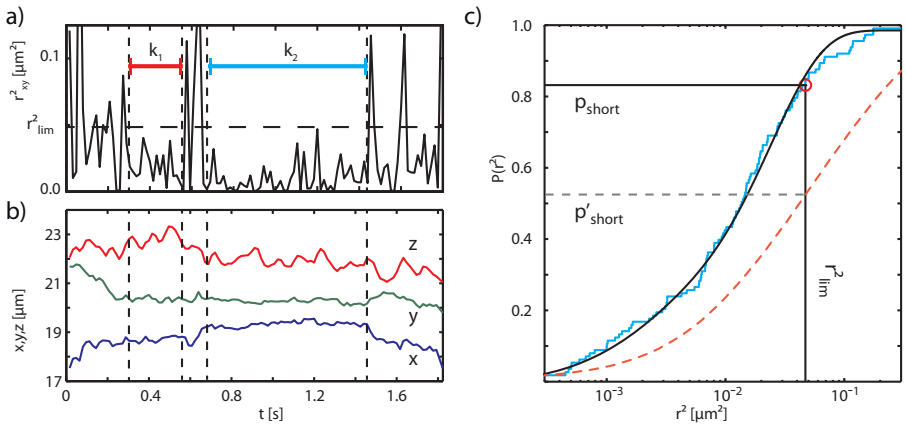

Fig. 4.16: Verification of dwell times in Fig. 4.15. **a)** Squared 2D jump distance as a function of time. Dashed lines delimit a short (red) and a longer (blue) dwell time below a threshold r^2_{lim} indicating reduced mobility of the particle. **b)** x (blue), y (green) and z (red) coordinate as a function of time. **c)** Cumulative distribution of squared jump distances of the nuclear envelope ensemble (red dashed, Fig. 4.11) as well as the single trajectory (blue, Fig. 4.15) and two component fit (black).

dwell time k_2 makes up almost half of the trajectory duration. Thus, short displacements contribute a large fraction $p_{short} = 0{,}8319$ to the distribution $P(r^2)$. In the dataset of the entire nuclear envelope ensemble (Fig. 4.11 c)) with squared jump distance distribution $P'(r^2)$, the relative frequency of displacements $r^2 < r^2_{lim}$ is only $p'_{short} = P'(r^2_{lim}) = 0{,}52$ as indicated in Fig. 4.16 c). If the ensemble distribution $P'(r^2)$ was representative of the trajectory analyzed here, dwell times of duration k_1 and k_2 would occur in less than one out of 10000 randomly drawn jump distance sequences. Both events would thus be considered highly significant with p-values $\leq 10^{-4}$.

3. Reduced mobility along the nuclear envelope

Similar non-uniform motion was also observed for mRNPs even closer to the NE. The trajectory displayed in Fig. 4.17 stayed within a distance of $\leq 1{,}5$ µm from the NE except for a short period of 2,6 s during the 15,4 s observation time ($n_{loc} = 933$, $t_{cyc} = 16{,}5$ ms).
The cumulative squared jump distance distribution for this trajectory was best fitted by a bimodal distribution yielding $D_1 = 0{,}27 \pm 0{,}01$ µm^2/s ($93{,}7 \pm 0{,}7\%$) and $D_2 = 1{,}61 \pm 0{,}24$ µm^2/s ($6{,}3 \pm 0{,}7\%$) (Fig. 4.17 c)). The diffusion coefficients agreed within the uncertainty of the fit results with the components D_2^{ens} and D_3^{ens} of the ensemble analysis (Tab. 4.1).

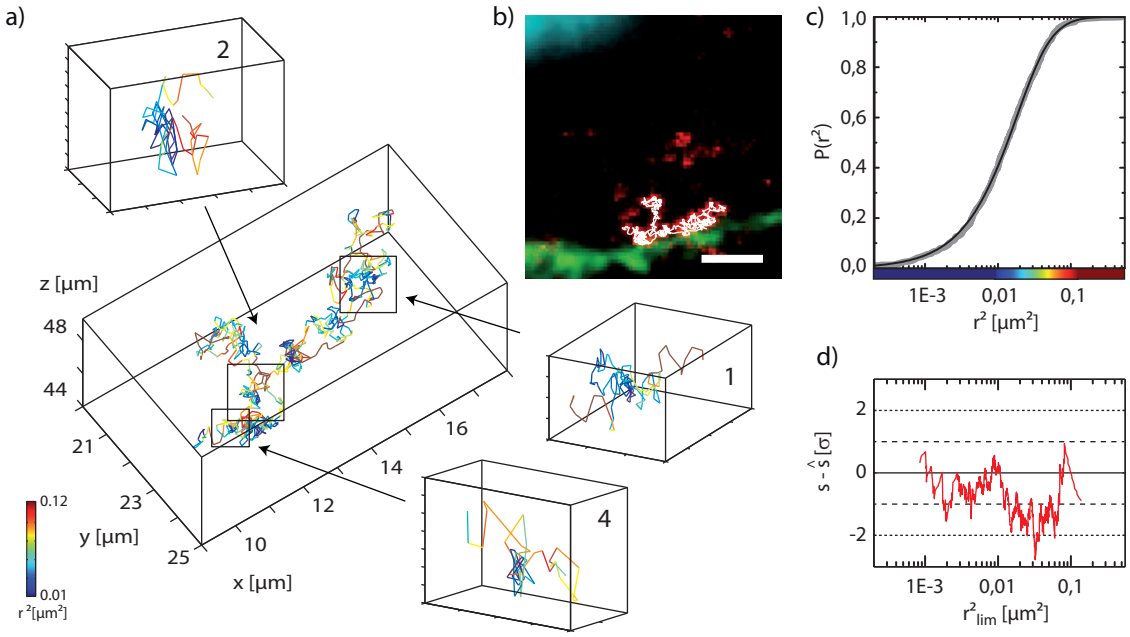

Fig. 4.17: Long trajectory at the nuclear envelope. **a)** 3D plot of the trajectory color-coded according to the squared displacement. Blue indicates low, red high mobility. Exemplary dwell time events as numbered in Fig. 4.18 and Tab. 4.3 are highlighted. **b)** Overlay of reference information (green: NE, cyan: PC) and 2D projection of the trajectory. Scale bar, 5 µm. **c)** Cumulative distribution of squared jump distances (gray) and bimodal fit (black). Colorbar corresponds to color code in **a)**. **d)** Deviation of the experimental transition probability s from the expectation value of a Bernoulli trial $\hat{s}$ in units of the theoretical standard deviation of the Bernoulli trial as a function of r^2_{lim}.

In this trajectory, periods of immobilization were not as evident from visual inspection of the image sequence as in the trajectory analyzed in Fig. 4.15 and 4.16, presumably because both components had a diffusion coefficient much larger than the immobile fraction found in previous experiments ($D_1^{ens} = 0{,}046$ µm^2/s).
By setting a threshold r^2_{lim}, two populations of either short or long jump distances are defined. An analysis of the transition frequency s between these two populations yields insight on the detectability of dwell times in either of the populations. A transition is defined as a short jump distance $r^2 \leq r^2_{lim}$ followed by a long jump distance $r^2 > r^2_{lim}$ or vice versa. If retention in one of the states occurs on timescales of the temporal resolution of the experiment, it becomes more likely to observe consecutive jump distances belonging to the same population. Thus, the transition frequency s between the two populations will be reduced with respect to the value $\hat{s}$ expected for a sequence of squared jump distances randomly drawn from $P(r^2)$ according to eq. 2.15.
Fig. 4.17 d) displays the deviation of the experimentally observed value s from the expectation value $\hat{s}$ in units of the standard deviation $\sigma_{\hat{s}}$ of the expectation value as

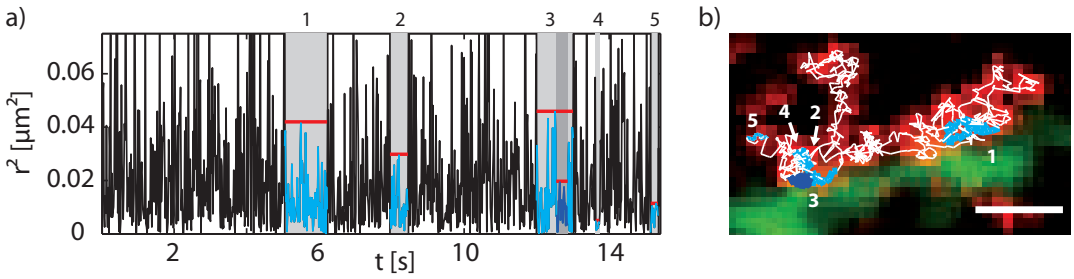

Fig. 4.18: BR2.1 mRNP dwell times at the nuclear envelope. **a)** Squared particle displacement as a function of time. Dwell times significantly deviating from stochastic behavior are highlighted (gray areas and blue plot). Threshold values r^2_{lim} for each of the dwell times are indicated (red). **b)** Overlay of NE position (green), maximum intensity projection of mRNP signal (red) and 2D projection of trajectory data. Scale bar, 2 µm.

a function of the threshold value r^2_{lim}. Over a range of r^2_{lim} = 0,01 - 0,08 µm^2, the deviation from random behavior is larger than one, and for some values of r^2_{lim} even larger than two standard deviations. Since $\hat{s}$ follows a binomial distribution and can be approximated by a normal distribution for large values of n' according to the central limit theorem, a value of $s - \hat{s} \leq -1{,}6 \cdot \sigma_{\hat{s}}$ shows that a value lower than s can be found in $< 5\%$ of jump distance sequences randomly drawn from $P(r^2)$. The deviation from stochastic behavior is thus denoted significant. For $s - \hat{s} \leq -2 \cdot \sigma_{\hat{s}}$, this probability is reduced to $< 2{,}3\%$. The low experimentally observed transition frequency s indicates that the order of jump distances does most likely not result from a stochastic process.

In a more detailed analysis, all significant dwell times were extracted over the entire range of possible values for r^2_{lim} instead of choosing a single empirical value. The relative fraction $p_{short} = P(r^2_{lim})$ of $r^2 \leq r^2_{lim}$, was determined from the squared jump distance distribution of the trajectory itself (Fig. 4.17 c)). Results are displayed in Fig. 4.18 a) and summarized in Tab. 4.3. Five significant dwell times in a state of low mobility with p-values $< 0{,}05$ were identified throughout the tra-

Tab. 4.3: Parameters of the dwell times identified in Fig. 4.17. #: number of event, Δt: duration, r^2_{lim}: threshold, p: significance of dwell time below r^2_{lim}.

#	Δt[s]	r^2_{lim}[µm^2]	p
1	1,180	0,0420	0,0024
2	0,512	0,0298	0,0476
3	1,023	0,0459	0,0396
3a	0,330	0,0197	0,0386
4	0,116	0,0050	0,0260
5	0,215	0,0114	0,0183

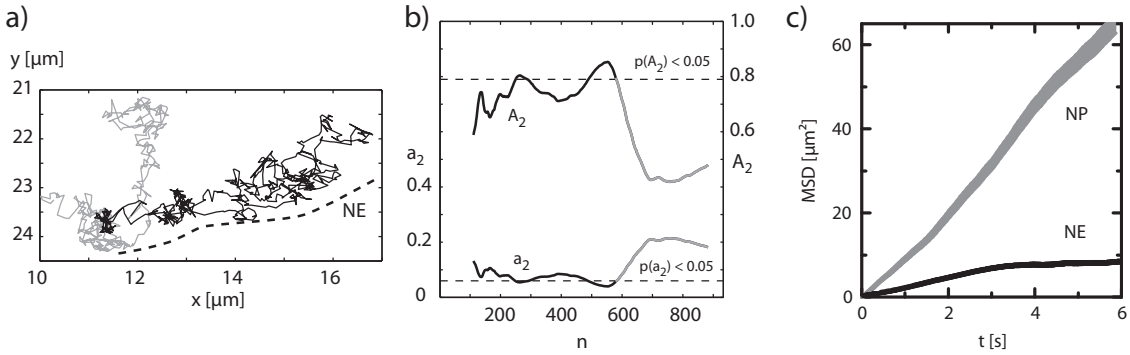

Fig. 4.19: Asymmetric diffusion at the nuclear envelope. **a)** The trajectory described in Fig. 4.17 traveled along the nuclear envelope (dashed line, NE) for more than 500 frames (black) before it separated from the NE temporarily (gray). **b)** Asymmetry parameters a_2 and A_2 from the start of the trajectory up to frame n. For the part of the trajectory highlighted in **a)** ($n < 550$), both indicate an irregular shape of the trajectory with significance $\min(p(a_2)) < 0{,}024$ and $\min(p(A_2)) < 0{,}012$ according to [128]. **c)** 2D MSD plots (± s.e.m. boundaries) for the trajectories presented in Fig. 4.12 (nucleoplasm, NP, gray) and Fig. 4.17 (nuclear envelope, NE, black). At the nuclear envelope, the mRNP mobility was greatly reduced as compared to the nucleoplasm. At the nuclear envelope, diffusion appeared to be confined.

jectory. Their duration ranged from 0,116 s to 1,180 s. In one case (#3a), a dwell time was already contained in a longer dwell time identified at a higher threshold. Except for the last event, all dwell times of low mobility were found in parts of the trajectory facing the nuclear envelope (Fig. 4.18 b)). Statistically significant dwell times in a state of higher mobility ($r^2 > r_{lim}^2$) could not be detected. This may either indicate that dwell times in the more mobile state are not long enough to be detected or that they are frequently interrupted by single shorter displacements.

Notably the particle observed in Fig. 4.17 traveled mostly along the nuclear envelope rather than randomly through the nucleoplasm. From the radius of gyration tensor of the trajectory, the principal radii of gyration, R_1^2 and R_2^2 can be determined [128]. They yield asymmetry parameters

$$a_2 = \frac{R_2^2}{R_1^2} \tag{4.2}$$

$$A_2 = \frac{(R_1^2 - R_2^2)^2}{(R_1^2 + R_2^2)} \tag{4.3}$$

Circular symmetric trajectories result in $a_2 = 1$ and $A_2 = 0$, whereas linear trajectories yield $a_2 = 0$ and $A_2 = 1$. In Fig. 4.19 b), both measures are shown as a function of the number of frames from the start of the trajectory. Up to the point where the trajectory branches away from the nuclear envelope (frame 550), both parameters indicate a highly irregular trajectory shape. By evaluating a_2 and A_2,

the shape of the trajectory was compared to the expectation value for free diffusion. Significance levels $p < 0{,}05$ for both parameters (Tab. 2 in [128]) are shown. An evaluation of the first 550 frames of the trajectory yielded minimal p-values $p(a_2) < 0{,}024$ and $p(A_2) < 0{,}012$. These values show that it is very unlikely to observe a trajectory of this shape for freely diffusing particles. More than 97,6% or 98,8% of all freely diffusing particles would display a more symmetric trajectory.
Furthermore, the asymmetry of the trajectory is also evident from an MSD plot (Fig. 4.19 c)). The shape of the MSD plot for the trajectory analyzed here indicates a confinement of the mRNP motion. In contrast, for the trajectory presented in Fig. 4.12 (nucleoplasm) a higher and linear slope was found.

4.2.6 Spatial variation of mRNP mobility in the nucleus

The ultimate destination of mRNPs is to reach the cytoplasm and serve as templates for protein translation. However, previous experiments have shown that mRNA export through NPCs in the nuclear envelope is a rare event. In many cases, the interaction between mRNP and NPC is of transient nature and does not lead to an export of the mRNA from the nucleus [10]. Dwell times of BR2.1 mRNPs at NPCs occur on time scales of several dozen to hundreds of milliseconds. They might thus account for the retention events observed at the nuclear envelope.

Comparing the exemplary trajectories from the nucleoplasm (Fig. 4.13) and the nuclear envelope (Fig. 4.17) as well as the results of the ensemble analysis (Tab. 4.1), it is evident that mRNP mobility is substantially reduced in the vicinity of the nuclear envelope. Diffusion in the nucleoplasm was dominated by two components of relatively high mobility. In contrast, trajectories in the vicinity of the nuclear envelope showed evidence of retention in states of low mobility (Fig. 4.17) or even immobilization (Fig. 4.16). Results are summarized in Tab. 4.4. Notably, most of the mobility components found for the exemplary trajectories agreed with results from the ensemble analysis (Tab. 4.1) although data were fitted independently and with different models. All components of the ensemble analysis were retrieved during the analysis of individual trajectories except for the ubiquitous very fast component D_4^{ens} attributed to unbound oligonucleotides. This was probably due to the fact that the more rapid diffusion of this fraction increased the chance of losing particles during real-time tracking and thus resulted in shorter trajectories.
The lower mobility at the nuclear envelope might result from interactions with intranuclear structures keeping mRNPs close to the nuclear envelope even when they were not bound to NPCs (Fig. 4.19). Restricting particle motion to a 2D surface, i.e. the nuclear envelope, would dramatically increase the chance for mRNPs to find an NPC on this surface. In contrast to the 3D case, random motion is spatially

Tab. 4.4: Comparison between individual trajectories and ensemble mobilities found in this work and previous results from other reports. NP: nucleoplasm. NE: nuclear envelope.

data	Fig.	immobile	low mobility	high mobility
NP ensemble	4.11	$(0{,}0 \pm 0{,}3\%)$	$(1{,}8 \pm 0{,}8\%)$	$(76{,}9 \pm 3{,}4\%)$
		$0{,}046 \pm 0{,}009\ \mu m^2/s$	$0{,}26 \pm 0{,}01\ \mu m^2/s$	$1{,}37 \pm 0{,}05\ \mu m^2/s$
NE ensemble		$(3{,}5 \pm 0{,}7\%)$	$(34{,}0 \pm 0{,}9\%)$	$(43{,}1 \pm 2{,}8\%)$
NP single	4.13	-	$0{,}85 \pm 0{,}01\ \mu m^2/s$	$1{,}69 \pm 0{,}01\ \mu m^2/s$
			$(30{,}0 \pm 0{,}9\%)$	$(70{,}0 \pm 0{,}9\%)$
NE single short	4.15	$0{,}025 \pm 0{,}005\ \mu m^2/s$	$0{,}38 \pm 0{,}01\ \mu m^2/s$	-
		$(14{,}2 \pm 1{,}3\%)$	$(85{,}8 \pm 1{,}1\%)$	
NE single long	4.17	-	$0{,}27 \pm 0{,}01\ \mu m^2/s$	$1{,}61 \pm 0{,}24\ \mu m^2/s$
			$(93{,}7 \pm 0{,}7\%)$	$(6{,}3 \pm 0{,}7\%)$
Tab. 2, [9]		$0{,}015\ \mu m^2/s$	$0{,}24\ \mu m^2/s$; $0{,}64\ \mu m^2/s$	-
Tab. 3.6, [109]		$0{,}001\ \mu m^2/s$	$0{,}5\ \mu m^2/s$	$1{,}4\ \mu m^2/s$

confined in 1D or 2D systems. Confining particle motion to 1D or 2D, a principle known as *the reduction of dimensionality*, has been shown to facilitate protein interaction by locating the interaction partners to a 2D membrane instead of free 3D space [129] and is also found in the dynamics of transcription factors which undergo transitions between free 3D diffusion and 1D motion along a DNA strand [130].

5 Discussion

During the course of this work, a light sheet microscope capable of 3D SPT in a feedback loop was developed and accompanying algorithms implemented to enable real-time tracking with low photon counts. The setup was thoroughly characterized regarding temporal resolution and spatial accuracy using various test samples.
The technique was first applied to track lipids in an *in vitro* model system for free-standing lipid bilayers, namely giant unilamellar vesicles of various compositions. Due to the high sensitivity of the method, a single fluorescent label was sufficient for several hundred observations of individual lipids.
Subsequently, experiments were performed in an *in vivo* model system. Both, mRNA and rRNA particles were tracked inside *C. tentans* salivary gland cell nuclei. The exceptionally long trajectories obtained by feedback tracking enabled analysis of complex mobility patterns based on individual particles, identification of dwell times in mobility states and comparison of individual particle behavior to the ensemble average.

5.1 The light sheet microscope

In light sheet illumination, the divergent nature of Gaussian beams results in a trade-off between optical sectioning and the size of the object field, over which sectioning is achieved. With high NA illumination objectives, a light sheet thickness below 1 µm can be achieved [52] at the cost of a strong beam divergence and a short Rayleigh length. Here, a slightly thicker light sheet was employed to achieve optical sectioning across a larger object field. The light sheet was tailored to a thickness of 2 µm, resulting in a Rayleigh length of approximately 20 µm (sec. 3.4.2). This value corresponds to the typical radius of a *C. tentans* salivary gland cell nucleus (15 - 30 µm) and is slightly larger than half of the object field upon imaging with the Ixon DU860 camera and 100× magnification (15,4 µm). Further, the light sheet width perpendicular to the illumination and detection axis exceeded the size of the object field by far. Positioning the light sheet focus in the image center thus resulted in a homogeneously illuminated image.
The wavelength-dependent beam divergence as well as the use of singlet lenses in the illumination path led to a chromatic shift larger than the Rayleigh length between the light sheet foci of different wavelength. It was corrected for by reducing the distance between the lenses of a cylindrical beam expander in the illumination path. This resulted in a slightly divergent beam incident on the illumination objective but reduced the mutual separation between the foci of different wavelength to values far below the Rayleigh length. For fluorescence detection, a long working distance water immersion objective was chosen. It provided an NA of 1,15 suitable for single molecule detection in combination with an exceptionally long working distance of 610 µm. Large axial displacements of the sample chamber were possible

without further corrections since no refractive index mismatch occurred.
Even though the light sheet thickness was approximately twice as large as the detection objective depth of field, the background signal was significantly reduced as compared to epi-illumination widefield microscopy and single molecule observation deep inside extended specimen could readily be achieved.

5.2 Astigmatic detection for 3D localization

3D particle localizations can be determined by a number of different approaches. The most widely used methods - orbital scanning, multifocal plane detection and PSF engineering - were presented in sec. 1.7.3. Although they generally achieve similar localization precision [131], each of them has unique advantages and disadvantages. Major differences arise in the requirements towards instrument design and image post-processing.
Splitting the fluorescence signal in two images as in bifocal plane microscopy enables effortless acquisition of regular widefield images but reduces the number of photons contributing to the signal in each of the images. The separation between the focal planes governs the axial localization precision [78]. For lateral localization, images can be added up to compensate for the reduced number of photons in each of them. However, the effect of detector noise is amplified by a factor corresponding to the number of images acquired. Precise correction for alignment errors between the images is crucial for the recombination of the signals but usually requires computational transformation of the images [94].
In multifocal plane microscopy [93], $9 - 25$ focal planes are imaged simultaneously by a combination of phase shifting elements in the detection path. Each of these very costly elements is corrected for only one specific wavelength. Although single particle observation has been reported, the emitted photons were split into an even higher number of subimages than in bifocal plane microscopy. Single particle tracking data acquired with the instrument were published but trajectories did not cover more than half of the axial detection range of the instrument. Presumably, photobleaching was a problem since only 1/9 of the photons collected by the detection objective contributed to form one of the subimages. Further losses of $\approx 35\%$ are introduced by the phase elements. Replacing the cylindrical lens with an estimated transmission of 96% by such phase elements with 65% transmission and using this technique for single lipid tracking at the same photon emission rate as determined in sec. 4.1.2 (130 photons per signal) would have resulted in no more than $130 \cdot \frac{0{,}65}{0{,}96} \cdot \frac{1}{9} \approx 10$ photons contributing to the signal in each of the image planes.
In contrast, PSF engineering approaches encode 3D localizations in a single image

frame by imprinting a phase pattern in the fluorescence wavefront and thus distorting the shape of the PSF.
One specific phase pattern leads to a PSF with the shape of a double helix. Spatial light modulators, which have previously been used to generate the DH-PSF, introduce a light loss of ≥ 35 % [95]. Using a specifically designed phase plate may reduce this value to ≈ 5 % but the nature of the resulting PSF still requires a separate detection channel for the acquisition of reference images and thus detection with two cameras. A major advantage of the DH-PSF is its uniform localization precision over a large axial range [132].
Astigmatic detection for 3D localization does also rely on distortions of the PSF shape. By inserting a cylindrical lens [14] or a deformable mirror [96] in the detection path, the PSF is elongated to an elliptical shape for particles at an axial distance from the effective focal plane. Its diameter is slightly increased within the effective focal plane, which affects the localization precision (eq. 1.17). The elliptical PSF shape leads to an anisotropic localization precision ($\sigma_x \neq \sigma_y$) for particles not located in the focal plane ($z_{rel} \neq 0$) [131].
The large size of the *C. tentans* salivary gland cells investigated here required the use of light sheet microscopy to achieve a high SNR for single particles. In principle, either of the 3D localization techniques could be combined with light sheet microscopy. However, the fact that in multifocal plane microscopy all focal planes distributed over an axial range of 2 - 4 µm in object space need to be illuminated simultaneously and homogeneously contradicts the idea of achieving high single particle SNR by using optically sectioned light sheet illumination. Furthermore, the limited number of fluorescence photons available from each labeled particle had to be used as efficiently as possible to enable the acquisition of trajectories with a high number of localizations. Hence, splitting the photons into several image planes was unfavorable.
Here, astigmatic detection was chosen to achieve 3D localization. While both, the double-helix and the astigmatic PSF, provide 3D information in a single image frame, the distortions in the astigmatic PSF were only minor in a sense that regular widefield imaging of continuous structures (e.g. the nuclear envelope) was possible with the cylindrical lens in place. Images were slightly blurred as compared to regular detection because the area of the PSF was increased by a factor $w_{ast}^2/w_0^2 \approx 1{,}5$ in the effective focal plane during astigmatic imaging (Fig. 3.11).
Due to the larger PSF width, fluorescence photons from a single particle were spread over a larger area. This was compensated for by acquiring images with the Ixon DU860 camera and 100× magnification (40× objective and 2,5× secondary magnification), resulting in an object pixel size of 240 nm for mRNA and rRNA tracking experiments. Although this value is fairly large for single particle localization experiments, it does comply with the Nyquist-Shannon criterion for the increased PSF width and an emission wavelength in the near infrared ($\lambda_{em} \geq 650$ nm).
Since particles were kept close to the focal plane ($z_{rel} \leq 250$ nm, Fig. 3.12) during

feedback tracking, only small differences occurred between the PSF width along x and y, w_x and w_y. Both values differed by less than a factor of 1,5 across the axial detection range (Fig. 3.11).
The axial localization precision depended on the separation between the focal planes in x and y (the amount of astigmatism) [78]. The focal length of the cylindrical lens was chosen and the lens positioned such that the amount of astigmatism was slightly smaller than the detection objective depth of field. A higher amount of astigmatism would have allowed for higher axial localization precision but on the downside also resulted in stronger aberrations and an increased PSF width in the effective focal plane accompanied by a loss in lateral localization precision.

5.3 Implementation of a feedback loop

During real-time tracking, the 3D information encoded in the image frames had to be rapidly extracted and converted to a feedback signal. To this end, efficient image analysis algorithms were combined with a fast piezo stage to follow single particles by displacing the entire sample chamber. The image analysis code was implemented in terms of a DLL written in C++ (sec. 3.2.1). Since only one particle at a time was tracked by the real-time algorithm, its lateral position could be coarsely detected by simply finding a local intensity maximum in the vicinity of a previous particle localization. Axial localization required the analysis of the PSF shape as discussed in sec. 5.4 and comparison to a calibration dataset. The output of the DLL corresponded to the axial localization of a specific particle in terms of a sample stage voltage.
An interface connecting the ImSpector microscope control software with the DLL was developed in collaboration with LaVision BioTec GmbH (Bielefeld). While image analysis, 3D localization and tracking data storage were performed within the DLL, the piezo stage was addressed by ImSpector based on the return value of the DLL. The feedback loop was closed by rapidly displacing the stage and thus repositioning the sample before acquisition of the next image frame.
Alternatively, both, the light sheet and the detection objective position, could have been adjusted after each image frame [16]. This approach was not implemented here since it would have required the displacement of not only one but two mechanical elements and complicated the illumination beam path.

5.4 A novel axial localization procedure

The technical goal during real-time tracking was to keep an individual particle of interest close to the focal plane by displacing the sample stage axially. Due to the large object field, repositioning the sample stage laterally was not required. The primary task of the real-time tracking DLL was thus, to extract 3D positional information on a single particle from the image data as quickly as possible.
Axial information was encoded in the astigmatic PSF shape. As discussed in sec. 3.2.1, it can be analyzed by different algorithms.
Calculation of the moments of the intensity distribution required the least computational effort and provided results within a few dozen microseconds but was very susceptible to errors introduced by background noise and failed for low SNR.
Least squares fitting of an elliptical Gaussian peak to the data is the most common approach and yielded a high localization precision over a large SNR range [79]. Accurate estimates of the PSF width as needed for axial localization were given by the standard deviations of the peak along the x- and y-axis. However, the iterative nature of least squares optimizations was unfavorable for real-time tracking. The number of iterations before convergence of the fit depended strongly upon the quality of initial parameter guesses and increased with lower SNR, resulting in computation times of more than 1 ms per fit under typical conditions.
To tackle this problem, a novel axial localization procedure was devised (sec. 3.2.1). Axial localization based on normalized covariance calculation provided a similar localization precision as least squares fitting but in a fraction of the computation time and with constant computational effort, independent of the experimental data. While cross-correlation of image data with 3D image stacks of the PSF has been used in previous publications for particle localization [54], the approach presented here requires just two axially separated images of the PSF to interpolate axial localizations over a range of several hundred nanometers.
Further, a linear metric independent of SNR was found, which enables axial localization based on two constant parameters determined by the shape of the PSF and the choice of templates. This innovation was crucial for enabling for the first time feedback tracking of biomolecules labeled with small fluorophores. All other previously known axial localization procedures required either a much higher number of photons per signal [121] or computation times too long for real-time applications.
The method developed here does not rely on an analytical model of the PSF shape. Any continuous, axially asymmetric deformation of the PSF could in principal be used for 3D localization with the cross-correlation approach if the templates are extracted from an experimentally acquired PSF [54].

5.5 Real-time tracking and post-processing

The real-time tracking procedure must be distinguished from particle localization and tracking during post-processing. While the real-time tracking algorithm was developed to follow a bright signal with emphasis on the axial dimension, all particle signals contained in the image data were localized during post-processing with high accuracy in all three spatial dimensions.
During real-time tracking, lateral localization was achieved by calculating the first moment of the intensity distribution in a signal, i.e. its centroid. For axial localization, the normalized covariance calculation was employed as discussed above. Since the 3D coordinates of only one signal per frame were determined, crossing trajectories could not be noticed and the algorithm might switch between trajectories if the particle density is too high.
During post-processing, particle candidates were identified by either of two methods (sec. 3.3.1). Under homogeneous background intensity conditions, Gaussian smoothing and a search for local intensity maxima allowed for a reliable identification of candidates. However, a inhomogeneous background intensities led to a high number of false candidates or completely prevented particles from being identified with this approach. Identification based on cross-correlation with templates of the experimentally acquired PSF proved to be more reliable under all conditions.
Lateral coordinates for particle candidates in the image data were determined by least squares fitting of an elliptical Gaussian peak. Axial localizations were obtained by normalized covariance calculation. Candidates were verified if the PSF width, the peak intensity and the normalized covariance values stayed within upper and lower bounds.
Other algorithms, in particular maximum likelihood estimators, are able to yield the theoretically optimal localization precision possible as determined from the Cramer-Rao-bound [81]. Since their computation time for a single localization exceeds that of a least squares fit even in accelerated implementations [133], such algorithms are not suited for fast real-time tracking with currently available computer hardware. Moreover, an algorithm working with an astigmatic PSF model for 3D localization has not been published yet, leaving this method applicable only to 2D particle localization.
The localizations of all verified candidates were assigned to trajectories. Modern particle tracking algorithms are capable of dealing with very high particle densities and intersecting trajectories. They optimize tracking results can by including *a priori* knowledge about the particles (e.g. particle velocity or directionality of trajectories) in the analysis [85] or by defining appropriate cost functions and using probabilistic methods [84].
Here, a basic nearest neighbor approach was chosen to connect localizations to trajectories. In contrast to the real-time tracking algorithm, which was not able

to detect intersecting trajectories, the post-processing code ended trajectories if ambiguous situations occurred. To avoid such events, the concentration of fluorescently labeled particles in the specimen needed to be extremely low. Typically, values in the picomolar range were used. If the particle density was found to be too high, the sample was pre-bleached by laser irradiation until a suitable concentration was reached.

5.6 Characteristics and limitations of the setup

Tracking range and axial detection range

Since depth-dependent distortions to the astigmatic PSF [114, 120] were avoided by use of a water immersion objective, calibration datasets were valid throughout the full accessible sample volume (Fig. 3.12 b)). Thus, the axial tracking range in the current configuration of the instrument was limited by the piezo stage travel range of 100 µm. The ultimate limit would be the detection objective working distance of 610 µm. In practice, the piezo travel range was never fully used since trajectories were either limited laterally by the object field (fluorescent beads in solution) or by photobleaching (lipids, mRNA, rRNA). The axial detection range of $w_{ax} = 468$ nm was experimentally determined by localizing mRNPs in a *C. tentans* salivary gland cell nucleus (Fig. 3.12). It was slightly lower than the detection objective depth of field and the amount of astigmatism. Brighter signals may result in a higher axial detection range.

Particle mobility and temporal resolution

In sec. 3.4.6, the response time of the piezo stage for a displacement of 200 nm was estimated to be $\tau_S = 1{,}12$ ms. A kinetic cycle time of the same duration was achieved during real-time tracking by reading out only a small fraction of the pco.edge camera chip. Assuming that tracking is initiated with a particle of interest in focus, its axial displacement within the temporal resolution may not exceed $\frac{1}{2}w_{ax}$ to successfully follow the particle. According to eq. 1.21 and 1.26, 1D axial particle displacements Δz within a time interval Δt and with diffusion coefficient D follow a normal distribution with standard deviation $\sigma_{1D}^2 = 2\,D\Delta t$. Thus, 68,3% of all 1D displacements will be smaller than σ_{1D}, 95,5% smaller than $2 \cdot \sigma_{1D}$ and so forth.
An upper limit for the diffusion coefficient D_{max} of particles to be tracked with the

instrument presented in this report can thus be estimated by setting

$$\Delta z = n \cdot \sigma_{1D} \leq \frac{w_{ax}}{2} \tag{5.1}$$

$$\Leftrightarrow \quad n \cdot \sqrt{2\, D_{max}\, \Delta t} \leq \frac{w_{ax}}{2} \tag{5.2}$$

$$\Leftrightarrow \quad D_{max} \leq \frac{w_{ax}^2}{8 \cdot \Delta t \cdot n^2} \tag{5.3}$$

where n determines the probability, with which the particle stays within the axial detection range. Smaller diffusion coefficients reduce the distance particles travel between frames and thus increase the probability of the particle to stay within the axial detection range. One should note, that in order to acquire trajectories of several hundred localizations, typical particle displacements must be *much* smaller than the axial detection range to also accommodate for the less frequent larger displacements. For occasions, in which a particle being tracked was not detectable in one image frame but reappeared in a successive frame, a *wait*-parameter was introduced in the real-time tracking algorithm (Tab. B.1). It allowed the algorithm to wait for a number of frames before searching for a new particle to follow. Such interrupted trajectories can be cured during post-processing by either making the particle verification process less restrictive than during real-time tracking or by allowing for gaps in trajectories.

A number of relevant parameter combinations for eq. 5.3 are given in Tab. 5.1. The highest possible diffusion coefficient $D_{max} = 22{,}8\ \mu m^2/s$ results from $n = 1$ and $\Delta t = \tau_S$. For mRNP tracking experiments, a typical kinetic cycle time was $t_{cyc} = \Delta t = 16$ ms. Thus, $D_{max} = 1{,}7\ \mu m^2/s$ for $n = 1$ and $D_{max} = 0{,}4\ \mu m^2/s$ for $n = 2$ can be calculated. Diffusion coefficients for mRNPs were in this range (Tab. 4.4). However, the effect of the *wait*-parameter was not included in these estimations and should slightly increase D_{max}.

For the beads with a radius of 20 nm in aqueous solution, a diffusion coefficient of $D = 9{,}4\ \mu m^2/s$ was observed with $t_{cyc} = 2{,}05$ ms temporal resolution - slightly below the theoretical expectation of $11{,}3\ \mu m^2/s$ at a viscosity of $\eta = 0{,}95$ cP and

Tab. 5.1: Maximum traceable diffusion coefficient D_{max} for typical cycle times t_{cyc} according to eq. 5.3. n: confidence interval in units of σ. D_{exp}: experimentally determined diffusion coefficient in applications. $w_{ax} = 468$ nm.

t_{cyc} [ms]	n	D_{max} [$\mu m^2/s$]	application	D_{exp} [$\mu m^2/s$]
1,12	1	22,8	max. value	-
2,05	1	13,4	20 nm beads	9,4
16,0	1	1,7	mRNPs	0,2 - 1,7
16,0	2	0,4		

$T = 297$ K. This represents the highest diffusion coefficient experimentally observed in this report.
The temporal resolution of 3D SPT depended not only on the piezo settling time and the kinetic cycle time of the camera, but also on the execution time of the tracking DLL (t_{CPU}). It was determined for different implementations of the real-time tracking DLL by repeated execution of the code in a test environment, simulating conditions during real experiments. For the most frequently used XCOR algorithm $t_{CPU} \leq 0{,}5$ ms per frame was found, depending on the size of the templates and the subimage evaluated for tracking (Tab. 3.4). Since most tracking experiments were conducted at 16 - 20 ms per frame, the feedback mechanism consisting of particle localization and piezo stage displacement consumed less than 10% of the kinetic cycle time.

Localization precision

The precision of the localization algorithms as a function of the number of photons per signal was characterized by repeatedly localizing fluorescent beads immobilized in an agarose gel. The standard deviation of the distribution of localizations yields the experimental localization precision (sec. 3.4.5). In contrast to theoretical descriptions of the localization precision presented in sec. 1.6, experimental results include artifacts resulting from vibrations or instabilities inherent to the setup.
However, such data can only be obtained from test samples and not from the actual particles of interest during tracking experiments. Their mobility prohibits the acquisition of hundreds of localizations of a single particle in one and the same position. Thus, to estimate the localization precision during tracking experiments, both aspects, theoretical expectations and experimentally determined results for immobile particles, need to be considered.
Interactions between mRNPs and intranuclear structures or NPCs in the nuclear envelope did not lead to immobilization for a sufficient time to obtain more than $20-30$ localizations of an individual particle in a presumably constant position. In contrast, rRNPs were observed to attach to binding sites in the nucleolus for several seconds and up to minutes. The standard deviation of localizations obtained during such events was in the range of 30 - 50 nm laterally and 100 - 120 nm axially at typical photon count numbers and thus slightly higher than theoretical predictions (sec. 4.2.2). The deviation may be due to residual motion of the particle. Particle motion with diffusion coefficient D during the exposure time t_{exp} increases the original PSF width w_0 according to eq. 1.19. Under typical conditions during mRNP tracking, the relative increase of the PSF width should amount to $10-30\%$. This translates to an increase of $5-15\%$ in localization precision, which approximately scales with $\sqrt{w}$ (eq. 1.18).

Sample preparation

Since long trajectories were to be acquired, the particle density was reduced to particularly low values. Typically, particles traveled less than $d_{max} = 1$ µm between subsequent frames. Their mutual separation must be larger than $2 \cdot d_{max}$ to prevent the real-time algorithm from jumping from particle to particle. This would correspond to a concentration of $c_{max} \leq 1/(2 \cdot d_{max})^3 \approx 150$ pM. However, since particles were mobile, they needed to be present in the specimen in much lower concentrations. Typically, less than 50 particles were visible in a single image frame corresponding to a detection volume of approximately $31 \times 31 \times 1$ µm^3. Thus, final concentrations within the specimen were $c_{typ} < 1$ pM.
To achieve such low values, special attention was paid to sample preparation and labeling strategies. In lipid tracking experiments, labeled lipids were incorporated in extremely low fractions of 10^{-7} mol%. For tracking of biomolecules in *C. tentans*, highly specific oligonucleotides with a high affinity were injected in low concentrations. Since exact concentrations in this regime are difficult to achieve, usually multiple cells were injected with varying amounts of injection solution.

5.7 Single lipid tracking

Imaging single fluorophores, and even more so tracking mobile molecules carrying single fluorophores in three dimensions, is very challenging since only a limited number of photons can be detected from them. A large fraction of the fluorophores may already bleach while the microscope is brought to its best configuration (e.g. finding the focus). In this regard, GUVs presented a convenient model system to test the single fluorophore tracking capability of the method presented here. Lipids carrying a single fluorophore could readily be incorporated during GUV formation with concentrations ranging from bright continuous membrane stainings to sparse single molecule conditions. Background fluorescence was minimal such that the photon budget could be used very efficiently. Since only a fraction of the GUV surface resided within the illumination light sheet at a given time, labeled lipids constantly diffused in and out of this area from a large reservoir. Additionally, the conditions in the surrounding medium seemed to favor stability of the ATTO647 fluorophores used here (sec. 4.1.1). In experiments with labeled lipids incorporated in a quasi-crystalline membrane, several 10^5 photons per fluorophore could be detected.
Depending on the GUV composition, lipids were either immobilized in the membrane or had a diffusion coefficient of up to 4,2 µm^2/s (sec. 4.1.3). 3D SPT experiments in a membrane of higher fluidity were conducted at down to 130 photons per signal (sec. 4.1.2). With the trade-off between the number of photons detected

and localization precision in mind, this approached the smallest possible value. A lower photon count rate would have reduced the axial localization precision to values similar to the axial detection range and thus prohibited feedback tracking. Resulting trajectories could be expected to be on the order of 10^3 localizations as estimated from the photon numbers, which was confirmed by experimental results. Thus, even at this remarkably low number of photons detected, trajectories ended due to the finite photon budget.

5.8 Tracking fluorescent beads in living tissue

Applicability of the method in biological specimen was demonstrated by tracking fluorescent beads in *C. tentans* salivary gland cell nuclei [121]. Trajectories could be acquired throughout the entire nucleus up to 200 µm above the coverslip (sec. 4.2.1). This unique sample depth could only be achieved by the adaptation of light sheet microscopy for SPT. The high number of photons detected per frame ($\langle N \rangle = 2130$ photons/frame) resulted in an extremely high SNR (≈ 30) and allowed for use of the simple center of mass axial localization algorithm. Beads could readily be tracked throughout a large part of the nucleus. Trajectories with durations of several minutes and thousands of localizations were acquired to achieve axial tracking ranges of more than 10 µm, unprecedented in biological specimen.
As expected, tracking was more prone to failure if particles were located above polytene chromosomes since the latter strongly scattered excitation light and introduced aberrations severely compromising the PSF shape. However, in parts of the nucleus devoid of chromatin and especially in the lower half of the nucleus, undistorted PSFs could be observed (Fig. 4.4, Fig. 4.5).

5.9 Single particle tracking in *C. tentans* salivary gland cell nuclei

SPT experiments in *C. tentans* salivary gland cell nuclei were more challenging than in GUVs mostly due to fluorescence background conditions. Its standard deviation was found to be about two to three times larger in the nucleoplasm as compared to the GUV membrane and even higher in the cytoplasm. Additionally, scattering particles and autofluorescent structures contributed to an inhomogeneous background intensity distribution. Thus, the SNR for a given number of photons per signal was severely reduced. Vice versa, the number of photons detected had to be increased to achieve a similar localization precision as compared to lipid tracking experiments. This was achieved not only by a higher illumination intensity, which,

in a first approximation, would also proportionally increase the background intensity, but by adding more fluorophores to the oligonucleotides used for labeling the BR2.1 mRNPs. Mass spectrometry results obtained by J. Rinne and A. Heckel (University of Frankfurt) indicated a labeling ratio of 3:1.
Further, the semi-transparent salivary gland tissue had an impact on the illumination light sheet passing tens of microns through the cytoplasm before reaching the nucleus. Scattering and refraction reduced the optical sectioning capability as previously observed in other light sheet microscopy applications [41].

Model selection

Most of the jump distance distributions presented here required a model with more than one mobility component. A higher number of components will always return a more accurate fit to any data distribution but may not necessarily yield more insight into the data. Here, models were selected by optimizing both, the χ^2 error of the fit and the shape of the residuals while using a minimum number of components. In some cases, introducing an additional component led to two components with the same diffusion coefficient. Notably, similar diffusion coefficients were found in independent evaluations of different mRNP tracking experiments. Nevertheless, the diffusion coefficients stated throughout this report are essentially a way to parametrize the distributions of jump distances observed in the respective experiments. As demonstrated in Fig. 4.13, diffusion coefficients usually represent a mobility distribution rather than yielding absolute measures of particle displacements.

rRNA tracking

Applying the technique to follow the motion of individual rRNA particles (sec. 4.2.3) enabled the direct visualization of transitions between states of very different mobility. While free diffusion of an exemplary particle in the nucleoplasm occurred at a diffusion coefficients of $D = 2{,}87\ \mu m^2/s$, interactions with the outer edge of the nucleolus led to phases of virtual immobilization.

mRNA trajectory characteristics

Regardless of the challenging conditions, mRNP trajectories spanning an axial range of 5-10 µm with a duration of 4 - 8 s (Tab. 4.2) could regularly be acquired in the nucleoplasm. Some trajectories lasted for more than 15 s (sec. 4.2.5). Typically, 300 - 500 photons/frame were detected from a single mRNP, accumulating

to a total number of $10^4 - 10^5$ photons per trajectory. Assuming a transmission efficiency of $\leq 15\%$ for the entire microscope and three fluorophores per oligonucleotide at a labeling ratio of a single oligonucleotide per mRNP, $10^5 - 10^6$ photons were *emitted* per individual Atto647N fluorophore before photobleaching. This is in the range of previously reported values [127]. Thus, again the photon budget of the fluorescent label was the limiting factor for trajectory duration. In previous reports, the highest number of localizations in a single BR2.1 mRNP trajectory was around twenty [9]. Compared to this value, observation times for individual particles could be increased by more than one order of magnitude. The axial range of the trajectories was similar to values reported by others for fluorescent beads [16] or QD-labeled receptors [134] using feedback tracking approaches, but, with the method presented here, was for the first time achieved for biomolecules labeled with small fluorophores.

mRNA mobility states

Intranuclear trafficking of BR2.1 mRNPs was studied in detail on the basis of individual particles. Notably, particle mobility did not only vary significantly between glands or nuclei as previously reported [109] but already between areas within the same nucleus (Fig. 4.11) and even between individual mRNPs (Fig. 4.13). Measurements were conducted on salivary glands incubated in a solution of 10% hemolymph in PBS. Diffusion coefficients found for BR2.1 mRNPs were relatively high but in the range of previous reports [109].
Trajectories in the nucleoplasm were obtained well separated from polytene chromosomes or the nuclear envelope. Since the particles were expected to have a spherical shape and similar sizes, one possible explanation for differences between individual particles might be interactions with intranuclear structures [18, 19, 109]. During visual inspection of trajectories, phases of reduced mobility seemed to alternate with more mobile phases. Mobility of individual mRNPs in the nucleoplasm was not sufficiently described by a unimodal model but required at least two mobility components $D_1 = 0{,}85\ \mu m^2/s$ and $D_2 = 1{,}69\ \mu m^2/s$.
A detailed analysis of trajectories obtained by feedback tracking revealed a small number of short periods, during which particle mobility was unexpectedly low (Fig. 4.14).
Switching between states of different mobility was more evident for mRNPs close to the nuclear envelope (sec. 4.2.5). From the jump distance distribution of a single trajectory, two mobility components of $D_1 = 0{,}27\ \mu m^2/s$ and $D_2 = 1{,}61\ \mu m^2/s$ were obtained. A rigorous statistical analysis indicated that the temporal sequence of jump distances did not occur in a random order. Results point towards a retention, which favored the particle to remain in a state of either high or low mobility

instead of randomly transitioning between mobility states on the timescales investigated here. By further analysis, several statistically significant dwell times in a state of low mobility could be identified in exemplary trajectories (Fig. 4.16, Fig. 4.18). The analysis of this trajectory strongly indicates transient reductions of BR2.1 mRNP mobility in close proximity of the nuclear envelope. They may be explained by interactions of the mRNP with NPCs in the nuclear envelope and potentially indicate abrogated nucleocytoplasmic transport events.
However, virtually immobile states of mRNPs were also observed at a distance of up to 2 µm from the nuclear envelope (Fig. 4.18). In conjunction with the conspicuous asymmetry of the trajectory presented in Fig. 4.19, mRNPs seem to be prevented from diffusing back into the nucleoplasm once they have reached the nuclear envelope. It is known that mRNPs bind to fibrils forming a basket on the nucleoplasmic side of NPCs, enter the basket and are exported through the central channel of the NPCs [135]. The fibrils extend 100 nm or more into the nucleoplasm and interaction is initiated by binding of mRNPs to the tip of these fibrils. One possible explanation for the observed mobility pattern would be that mRNPs travel along the tips of the fibrils from NPC to NPC, before finding a pore mediating the nucleocytoplasmic transport event. Binding of mRNPs to NPCs could be blocked by incubation of the salivary glands with the transcription inhibitors DRB or actinomycin D, which also suppress mRNP accumulation at the nuclear envelope [135], to test this hypothesis.
Other reports suggest a scaffold structure in the vicinity of the nuclear envelope, which plays a role in guiding cargo towards NPCs and the formation of interchromatin channels in other cell types. Such a structure might also exist in *C. tentans* salivary gland cells and reduce the mobility of large particles by transient interactions with a loose meshwork of fibrillar extensions of NPCs, reaching several hundred nanometers into the nucleoplasm [136].
BR mRNPs are furthermore known to transiently bind to a fibrous intranuclear network [18, 135]. If BR mRNPs were indeed found to be slowed down already at a distance from the nuclear envelope greater than the length of fibrils associated with NPCs, this could explain the immobilization observed in Fig. 4.16.
In the experiments presented here, the position of the nuclear envelope was determined only once every few minutes. To increase the accuracy in measuring the separation between mRNP and nuclear envelope, it would be desirable to either detect its position simultaneously in a separate channel or interleaved with the mRNP detection channel. This could be achieved by alternating the excitation wavelength between frames, doubling the acquisition frame rate and running the real-time tracking algorithm on every second frame.
In any case, the unprecedented length of the trajectories obtained by 3D feedback tracking and the possibility to analyze mobility patterns on the basis of individual particles paves the way for a more detailed investigation of mRNP trafficking data than previously possible.

5.10 Conclusions and outlook

In the work presented here, a light sheet microscope capable of 3D single particle tracking in a feedback loop was developed. This was achieved by implementing real-time image analysis code and using image information to reposition the sample stage in a fraction of the kinetic cycle time. A novel axial localization scheme based on cross-correlation template matching expanded the applicability of the method to the low photon regime and enabled 3D localization within less than 1 ms.
Single lipids in a GUV membrane could be observed for more than 20 s, opening up new possibilities for studying processes like aggregation, pore formation or phase transitions in free-standing model membranes. For the first time, real-time feedback tracking of single emitters became feasible. Furthermore, BR2.1 mRNA and rRNA particles were followed in *C. tentans* salivary gland cell nuclei with observation times per particle prolonged by more than one order of magnitude as compared to tracking without a feedback mechanism. A rigorous statistical analysis proved the presence of transitions between different mobility states and enabled the detection of multiple retention times in a state of low mobility in single trajectories.
Since not only trajectories of individual particles but full image frames are acquired, the technique can be regarded as an extension to classical 2D SPT experiments. The high number of short trajectories typically contained in SPT datasets are appended by 3D spatial information for each trajectory on the one hand and by a number of exceptionally long trajectories on the other hand. The latter allow for comparison of individual particle behavior to the ensemble average. This can facilitate the assignment of mobility components found in the ensemble analysis to specific states of the particles under investigation. Furthermore, the long observation times allow kinetic aspects of the trajectories like transition rates or patterns in the temporal sequence of mobility states to be examined.
Characteristics and limitations of the setup were investigated in detail using various methods and test samples. The full potential of the setup, especially regarding axial tracking range and temporal resolution, has by far not been exhausted yet. The large tracking range of the piezo stage and the ability to detect single particles dozens of microns within the sample could be of use for the observation of transport phenomena in larger specimen like fruit fly or zebrafish embryos. Not only single molecules, but also viruses [15] or small vesicles could be tracked [137] to study interactions with the specimen.
Using adaptive optics in the detection arm to correct for sample aberrations might enable single particle detection with an even higher photon efficiency and deeper within the specimen [96] whereas simultaneous multi-color detection would be desirable to obviate any alignment problems resulting from residual sample drift.
Faster computer hardware should enable the use of more sophisticated algorithms for real-time 3D particle localization in the near future. This could also reduce the

number of photons required for an accurate localization and thus further extend the duration of individual trajectories [138] or enable tracking of fluorescent proteins. It might even be possible to execute the image analysis code right on the FPGA chip inherent to sCMOS cameras, obviating any delays due to data transfer from the camera to PC memory [139].
The method developed here presents a valuable extension to the single particle tracking toolbox and paves the way for a deeper understanding of the intracellular mobility and interactions between proteins and RNA particles in living cells.

A Appendix - Materials

In the following sections, biochemical materials including fluorescent labels and the components of the setup are listed.

A.1 Fluorescent probes

Tab. A.1: List of fluorescent dyes and beads. Extinction coefficient and quantum yield (QY) are given for dyes used in single molecule experiments. n.a., not available.

dye	company	λ_{ex} [nm] / λ_{em} [nm]	$\epsilon(\lambda_{ex})$ $[cm^1 M^{-1}]$	QY
SYTOX green	Invitrogen	504 / 524	n.a.	n.a.
AlexaFluor 546	Invitrogen	561 / 572	104000	0,79
AlexaFluor 647	Invitrogen	650 / 671	239000	0,33
Atto647	ATTO-TEC	645 / 670	120000	0,20
Atto647N	ATTO-TEC	646 / 670	150000	0,65
TetraSpeck 0,1/0,2/0,5 µm	Invitrogen	365 / 430	n.a.	n.a.
		505 / 515		
		560 / 580		
		660 / 680		
FluoroSphere 0,02µm crimson	Invitrogen	620 / 645	n.a.	n.a.

A.2 Fluorescently labeled oligonucleotides

Fluorescently labeled oligonucleotides were kindly synthesized and provided by J. Rinne and Dr. A. Heckel, University of Frankfurt.

Tab. A.2: List of fluorescently labeled oligonucleotides. c: stock concentration. $\bar{T}$ = dT(NH_2). See e.g. [9, 109].

name	label	c [μM]	target
BR2.1 mRNA 3×	3× Atto647N	50	*C. tentans* BR2.1 mRNA
sequence: 5′-H_2N-CUU GGC $\bar{T}$UG C$\bar{T}$G UGU $\bar{T}$UG CUU GG$\bar{T}$ UUG C-(NH_2)-3′			
rRNA 3×	3× Atto647	50	rRNA 28s subunit
sequence: 5′-H_2N-CAU UCG AAU AUU UGC $\bar{T}$AC UAC CAC CAA GAU CUG-(NH_2)-3′			

A.3 Light sheet microscopy setup

In the following tables, the components used to assemble the light sheet microscopy setup are listed.

Tab. A.3: Lasers used for fluorescence excitation.

laser	company	λ [nm]	power [mW]
Sapphire-100	Coherent	488	100
LasNova GLK 3250 T01	Lasos	532	50
Cube 640-40C	Coherent	640	40

Tab. A.4: Components of the laser and illumination units depicted in Fig. 3.1.

label	element	cat. no.	company
M1-M7	dielectric mirror	10D20ER.2	Newport
sM8	scanning mirror	GVS011	Thorlabs
DC1	dichroic mirror	XF2077 500DRLP	Omega Optical
DC2	dichroic mirror	580DCLP	Omega Optical
C1	cylindrical lens f = -22.2 mm	LK1006L1	Thorlabs
C2	cylindrical lens f = 150 mm	LJ1934L1	Thorlabs
C3	cylindrical lens f = -20 mm	LK1085L1	Thorlabs
C4	cylindrical lens f = 130 mm	LJ1640L1	Thorlabs
C6	cylindrical lens f = 150 mm	LJ1934L1	Thorlabs
AL	cylindrical lens f = 1 m	LJ1516RM	Thorlabs
	cylindrical lens f = 10 m	SCX-50.8-5000.0-C	CVI Melles Griot
AOTF	acousto-optical tunable filter	TF-525-250-6-3-GH18A	Gooch&Housego
Fiber	0,7mm optical single-mode fiber	kineFlex	PointSource

Tab. A.5: Components of sample mounting unit and stage control.

label	element	cat. no.	company
SC	sample cuvette	105-044-V2-40	Hellma
z piezo	piezo stage	P-611.ZS	Physik Instrumente
–	z piezo controller	E-625	Physik Instrumente
3 axes	3x linear stage	M-112.12S	Physik Instrumente
–	DAQ card	ME4660	Meilhaus

Tab. A.6: Configuration of the commercial microscope body.

label	description	company
microscope body	TI-Eclipse with secondary filter wheel	Nikon Instruments
T	1.0x tube lens	Nikon Instruments
	1.5x intermediate magnification tube lens	Nikon Instruments
2.5x	secondary magnification	Nikon Instruments
PIFOC	P-721 piezo objective mount	Physik Instrumente

Tab. A.7: List of objectives used for light sheet illumination and fluorescence detection. wd: working distance.

objective	company	NA	wd [mm]	usage
10x Plan Apo LWD	Mitutoyo	0,28	33,5	illumination
10x CFI Plan Fluor	Nikon	0,30	16,0	detection
20x CFI Plan Fluor	Nikon	0,50	2,1	detection
40x CFI Apo LWD λS	Nikon	1,15	0,6	detection

Tab. A.8: List of optical filters.

filter	cat. no.	company	usage
laser line notch	NF01-488/532/640U-23.7-D	Semrock	block scattered excitation light
emission	z532/640m	Chroma	fluorescence double band pass 532/640 nm excitation
emission	HQ 535/50 M (GFP-B)	Nikon	fluoerescence band pass 488 nm excitation

Tab. A.9: List of cameras used for fluorescence detection. a, physical pixel size. fps, maximum frame rate at full image field. QE, quantum efficiency at 650 nm.

camera, company	type	chip	a [µm]	fps [Hz]	QE	ADU $[\frac{cts}{e^-}]$
Ixon DV860 BV, Andor	EMCCD	128 x 128	24,0	500	92%	18.0
Ixon DU897 BV, Andor	EMCCD	512 x 512	16,0	32	92%	11.8
pco.edge, PCO	sCMOS	2560 x 2160	6,5	100	54%	0.458
Orca Flash 4.0, Hamamatsu	sCMOS	2048 x 2048	6,5	100	72%	0.458

B Appendix - Data organization

B.1 DLL arrays

profiles:		zcurr	zrel	znew	xpos	ypos	CC1	CC2	sgLevel
		0	1	2	3	4	5	6	7
double	0	...	...	...	...	...	...	...	...
(8 bytes)	1								
	.								
	.								
	.								
	N								...

timestamps:		time	valid	last	-	-	tmpl1	tmpl2	params
		0	1	2	3	4	5	6	7
float	0	...	...	...			0	0	0
(4 bytes)	1						...	...	tracking
									22
	.								...
	.								30 state
	.								31
									stack
									36
							...	...	...
							Ntmpl	*Ntmpl*	
	N						...	...	

Fig. B.1: Content and structure of the arrays *profiles* and *timestamp* of size N by 8 as set by the tracking DLL. N represents the number of frames in the experiment. At the end of an experiment information from the arrays was written to a text file with the structure explained in Tab. 3.3.

Tab. B.1: Parameters used in the tracking DLL and storage place in array timestamp.

variable	value	unit	array entry	usage
mode	0/1		timestamp[7][0]	switch between stack acquisition (0) and tracking (1)
tracking parameters				
xhme	64	pxl	timestamp[7][1]	initial search coordinates
yhme	64	pxl	timestamp[7][2]	
zhme	5	V	timestamp[7][3]	
CALoff	0		timestamp[7][4]	calibration fit offset
CALslp	4,8	V^{-1}	timestamp[7][5]	calibration fit slope
CALcorr	1		timestamp[7][6]	calibration scaling factor for signal strength
damp	1		timestamp[7][16]	damping factor for output
LIMdiff	5	pxl	timestamp[7][7]	search area limit if locked in to a particle
LIMsrach	25	pxl	timestamp[7][8]	search area limit if not locked in to a particle
LIMtmplt	4	pxl	timestamp[7][9]	template size
LIMcorr	3	pxl	timestamp[7][10]	size of area for cross-correlation
LIMvarmin	0,4		timestamp[7][11]	minimum valid cross-correlation value
LIMvarmax	1		timestamp[7][12]	maximum valid cross-correlation value
LIMimin	50	cts	timestamp[7][19]	minimum peak height above mean count level
LIMimax	8000	cts	timestamp[7][20]	maximum peak height above mean count level
LIMkbg	0	cts	timestamp[7][15]	background offset above minimum to be subtracted before center of mass calculation
wait	3	frames	timestamp[7][13]	number of frames to wait for a particle to reappear before returning to initial coordinates
gauss	0/1		timestamp[7][14]	if 1 smooth data by 3x3 pixel Gaussian kernel ($\sigma = 1$ pxl) before cross-correlation
LIMjmax	1	µm	timestamp[7][17]	maximum allowed axial displacement while following a particle
pxsize	240	nm	timestamp[7][18]	image pixel size
stack acquisition parameters				
dz	100	nm	timestamp[7][31]	axial distance between stack slices
fperslice	1	frames	timestamp[7][32]	number of image frames to be acquired at each axial position
nslice	1000	frames	timestamp[7][33]	number of slices in stack
zoffset	100	µm	timestamp[7][34]	piezo position for first slice in stack
direction	±1		timestamp[7][35]	sign of dz displacement
doCorr	0/1		timestamp[7][36]	if 1 try to perform tracking without feedback during stack acquisition, e.g. for calibration

B.2 MATLAB localization and trajectory data

Tab. B.2: MATLAB localization table format. Localizations are listed consecutively in temporal order. Further parameters determined for each localization can be appended in additional columns.

1	2	3	4	5	6	7	8	9	10
frame	int [cts]	x [pxl]	y [pxl]	w_x [pxl]	w_y [pxl]	bg [cts]	ξ_1	ξ_2	z [nm]
...	...	...	...	...	...	...	...	...	...
72	919,4	45,77	64,75	0,799	1,334	1275,5	0,711	0,556	317,54
72	1348,7	105,35	45,77	0,742	0,659	1340,7	0,496	0,618	923,92
73	961,5	46,64	65,54	0,879	1,065	1338,1	0,683	0,612	344,23
74	537,9	21,35	62,93	1,009	2,030	1224,4	0,671	0,429	665,96
74	907,1	46,05	65,27	1,082	0,553	1389,8	0,548	0,527	326,84
75	823,5	45,34	66,51	0,819	0,745	1337,6	0,588	0,558	310,34
75	788,7	21,27	62,64	0,760	1,327	1246,9	0,635	0,466	526,92
76	664,6	21,19	63,56	0,753	1,112	1256,1	0,590	0,484	433,92
...	...	...	...	...	...	...	...	...	...

Tab. B.3: MATLAB trajectory table format. The tracking algorithm assigned the localizations to trajectories, which were numbered and listed consecutively in temporal order.

1	2	3	4	5	6	7	8	9	10	11	12
#	trj	frame	x [pxl]	y [pxl]	z [nm]	int	-	ξ_1	ξ_2	w_x	w_y
...	...	...	...	...	...	...		...	...	...	...
41	4	72	45,77	64,75	317,5	919,4		0,711	0,556	0,799	1,334
42	4	73	46,64	65,54	344,2	961,5		0,683	0,612	0,879	1,065
43	4	74	46,05	65,27	326,8	907,1		0,548	0,527	1,082	0,553
44	4	75	45,34	66,51	310,3	823,5		0,588	0,558	0,819	0,745
...	...	...	...	...	...	...		...	...	...	...
45	5	74	21,35	62,93	665,9	537,9		0,671	0,429	1,009	2,030
46	5	75	21,27	62,64	526,9	788,7		0,635	0,466	0,760	1,327
47	5	76	21,19	63,56	433,9	664,6		0,590	0,484	0,753	1,112
...	...	...	...	...	...	...		...	...	...	...

C Appendix - Acquisition parameters

In Tab. C.1, the acquisition parameters for all experiments are listed.

Tab. C.1: Data acquisition parameters for all experiments. n.d.: not determined.

Fig.	specimen	camera	detection	t_{cyc} [ms]
Characterization				
3.9	calibration solution	pco.edge	10×	n.d.
3.10	0,2 µm beads in agarose	Ixon DU897	10×	n.d.
3.11	0,2 µm beads in agarose	Ixon DV860	40×, 2,5×	n.d.
3.12 a), b)	0,2 µm beads in agarose,	Ixon DU897	40×, 2,5×	n.d.
3.12 c)	mRNP oligonucleotides			16,5
3.13 a), b)	0,2 µm beads in agarose	Ixon DV860	40×, 2,5×	n.d.
3.14	0,2 µm beads in agarose	Flash 4.0	40×	0,19
3.15 a)	0,5 µm beads in PBS	pco.edge	40×	16,1
3.15 b)	0,1 µm beads in PBS	pco.edge	40×	5,07
3.15 c)	0,02 µm beads in PBS	pco.edge	40×	2,05
3.16	0,2 µm beads in PBS	Ixon DU897	40×, 2,5×	21,0
3.15 c)	0,5 µm beads in PBS	pco.edge	40×	1,12
Lipid tracking				
4.1	DPPE-ATTO647 / DPPC-chol. (90:10)	Ixon DU897	40×, 2,5×	32,5
4.2	POPE-ATTO647 / DPPC-chol. (50:50)	Ixon DU897	40×, 2,5×	16,1
4.3	POPE-ATTO647 / POPC	Ixon DU897	40×, 2,5×	18,2
C. tentans				
4.4	0,02 µm beads, NTF2-AF546	Ixon DU897	40×, 2,5×	51,0
4.5	0,2 µm beads in agarose	Ixon DV860	40×, 2,5×	n.d.
	BR2.1 oligos (3x Atto647N)			16,1
4.6	rRNA oligos (3x Atto647)	Ixon DV860	40×, 2,5×	16,1
4.7	BR2.1 oligos (3x Atto647N)	Ixon DV860	40×, 2,5×	16,1
4.8	BR2.1 oligos (3x Atto647N),	Ixon DV860	40×, 2,5×	20,3
	SYTOX green, NTF2-AF546			n.d.
4.10	rRNA oligos (3x Atto647)	Ixon DV860	40×, 2,5×	16,5
	NTF2-AF546			n.d.
4.12-4.14	BR2.1 oligos (3x Atto647N)	Ixon DV860	40×, 2,5×	20,3
4.15-4.19	BR2.1 oligos (3x Atto647N),	Ixon DV860	40×, 2,5×	16,5
	SYTOX green, NTF2-AF546			n.d.

D Appendix - PSF shape

After insertion of the cylindrical lens in the detecion arm, the minimum PSF width in the x and y focal plane ($w_{min,x}$, $w_{min,y}$) was slightly increased and the PSF width in the effective focal plane increased by a factor of $w_0/w_0^{reg} = 1{,}02 - 5{,}05$ depending on the exact position of the lens. Results are summarized in Tab. D.1. Experiments were performed in configuration 3, in which the amount of astigmatism ($a = 812$ nm at $\lambda = 640$ nm closely matched the axial extent of the PSF (683 nm $1/e^2$-radius) while the PSF in the effective focal plane was only slightly broadened as compared to regular imaging ($w_0/w_{0,reg} = 1{,}24$)

Tab. D.1: Parameters describing the PSF shape for selected instrument configurations and lens positions. c.r.: correction ring setting. $w_{min,x}$; $w_{min,y}$: PSF width in the x and y focal plane. a: astigmatism. w_0: PSF width in the effective focal plane. w_z: $1/e^2$-radius of axial intensity profile.

pos.	lens	λ [nm]	c.r.	$w_{min,x}$	$w_{min,y}$	a [nm]	w_0 [nm]	w_0/w_0^{reg}	w_z [nm]
-	-	488	0.17	164	166	-38	170	n.d.	477
-	-	532	0.17	189	182	50	186	n.d.	512
-	-	640	0.15	180	182	61	183	n.d.	417
-	-	640	0.17	183	180	39	183	n.d.	475
-	-	640	0.19	208	204	185	208	n.d.	678
T	10 m	640	0.17	n.d.	n.d.	>2000	921	5,05	n.d.
C	10 m	640	0.17	191	191	268	194	1,06	489
1	1 m	640	0.17	189	185	41	187	1,02	513
2	1 m	640	0.17	189	180	389	189	1,04	462
3	1 m	488	0.17	180	217	827	236	1,39	765
3	1 m	532	0.17	175	220	849	236	1,27	805
3	1 m	640	0.17	174	207	812	226	1,24	683
6	1 m	640	0.17	179	176	>2000	517	2,83	n.d.

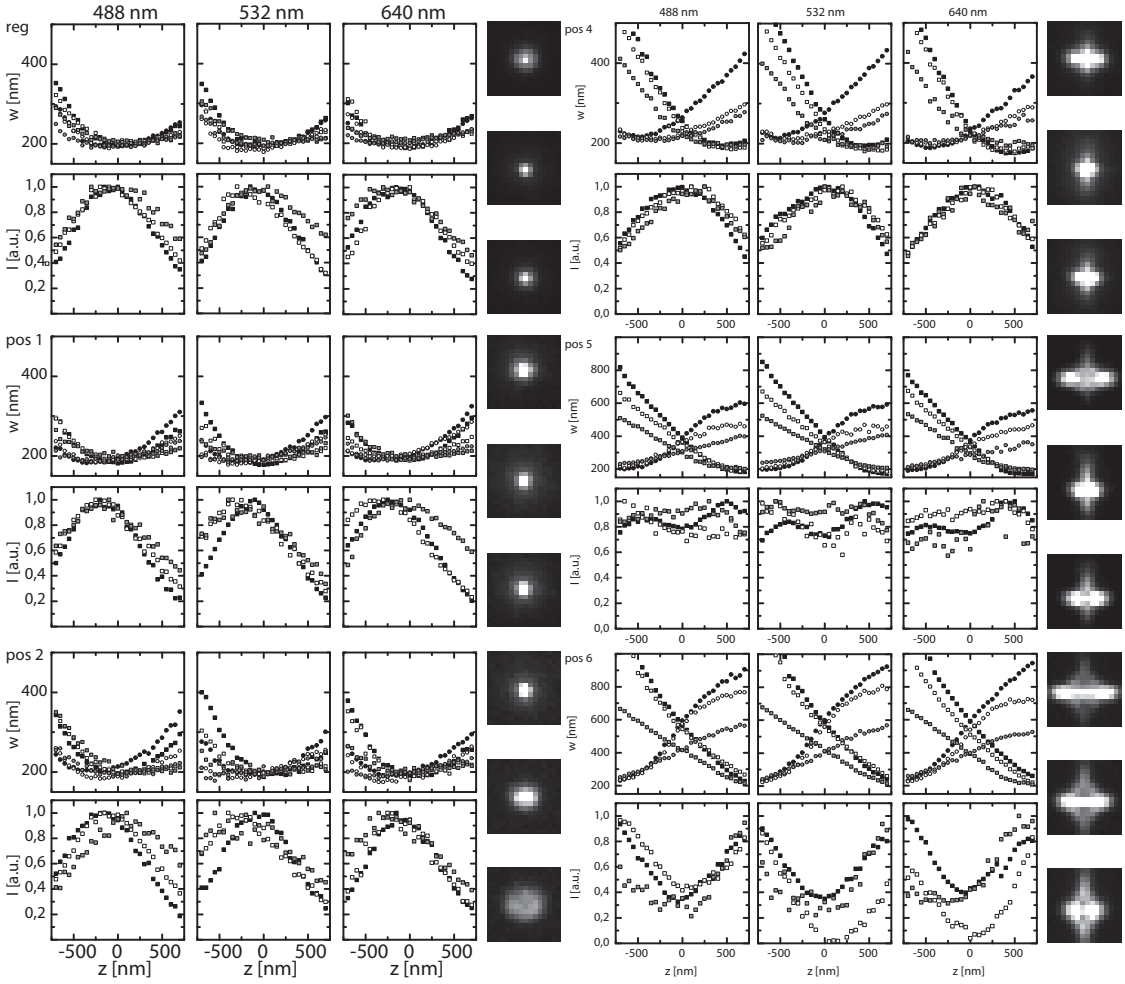

Fig. D.1: PSF shape analysis for different configurations. reg: regular imaging; pos1 - pos5: $f = 1$ m lens at increasing distance from the camera. pos1 and pos2 between camera and 2,5× magnification adapter. pos3 - pos5 between 2,5× magnification adapter and microscope body. At each position, the PSF was acquired using 200 nm TetraSpeck beads in 2% agarose and for excitation with 488 nm, 532 nm or 640 nm laser light. Bead images were fitted with a 2D Gaussian peak and PSF width along x (squares) and y (circles) plotted versus axial position (top panel for each configuration). Additionally, the peak amplitude I was plotted to determine the axial extent of the PSF (bottom panel for each configuration). The correction ring of the 40× objective was set to a coverslip thickness of 150 µm (black), 170 µm (white) and 190 µm (grey). Exemplary PSF images at ±500 nm and in the effective focal plane are shown for each configuration.

Acronyms

2D/3D	two- / three-dimensional
AC	alternating current
ADU	analog-to-digital conversion unit
AOTF	acousto-optical tunable filter
BR	Balbiani ring
BS	beam splitter
COM	center of mass
CPU	central processing unit
CYT	cytoplasm
DC	dichroic mirror
DH	double helix
DLL	dynamic link library
DNA	deoxyribonucleic acid
DPPC	dipalmitoylphosphatidylcholine
DPPE	1,2-**dip**almitoyl-**p**hospho**e**thanolamine
DSLM	digitally scanned light sheet microscopy
EMCCD	electron multiplying charge coupled device
FCS	fluorescence correlation spectrosopy
FPGA	field-programmable gate array
FRAP	fluorescence recovery after photobleaching
FWHM	full width at half maximum
G2D	2D Gaussian peak fitting
GUV	giant unilamellar vesicle
HILO	highly inclined laminated optical sheet microscopy
JD	jump distance
kb	kilo base pairs
LSFM	light sheet fluorescence microscopy
LWD	long working distance
mRNA/mRNP	messenger ribonucleic acid / messenger ribonucleoprotein particle
MLE	maximum likelihood estimator
MSD	mean square displacement
NA	numerical aperture
NE	nuclear envelope
NPC	nuclear pore complex
NTF2	nuclear transport factor 2
NUCL	nucleus
PBS	phosphate-buffered saline
PC	polytene chromosome, personal computer
PICS	particle image correlation spectroscopy
POPC	1-**p**almitoyl-2-**o**leoyl**p**hosphatidyl**c**holine
POPE	1-**p**almitoyl-2-**o**leoyl-**p**hosphoethanolamine
(a)PSF	(astigmatic) point spread function
QE	quantum efficiency
QY	quantum yield
rRNA/rRNP	ribosomal ribonucleic acid / rRNA protein particle
s.d.	standard deviation

s.e.m.	standard error of the mean
sCMOS	scientific complementary metal oxide semiconductor
SC	sample chamber
sM	scanning mirror
SNR	signal to noise ratio
SPT	single particle tracking
TEM_{00}	transverse electromagnetic mode of radial and angular order 0
TIRF	total internal reflection microscopy
TPE	two photon excitation
XCOR	cross-correlation

Symbols

α	semi aperture angle, MSD exponent
a	aperture radius, pixel size
a_i	relative amplitude of a fraction
A	amplitude
b	background fluctuation standard deviation
B	camera conversion factor [ADU]
c	speed of light, $c = 2{,}99792$ m/s
D	diffusion coefficient
ϵ	molar extinction coefficient
η	viscosity
E	energy
f	focal length
h	Planck constant, $h = 6{,}626$ Js
$h(x, y, z)$	electric field amplitude
F	excess noise factor
G	gain factor
I	intensity
J	power density
J_i	i-th order Bessel function
k_B	Boltzmann's constant, $k_B = 1{,}3806$ J/K
k_x	decay rate
λ	wavelength
n	refractive index
ν	frequency
NA	numerical aperture
$\bar{N}$	total number of photons
$\langle N \rangle$	mean number of photons
QE	quantum efficience
QY	quantum yield
p	power

$p(r, \Delta t)dr$	probability density
$\phi(x, y, z)$	electric field phase
r	radius
σ	localization precision (standard deviation)
S_i	electronic singlet state ($i = 0,1$)
τ_{bleach}	photobleaching time constant
τ_{exp}	fluorescence lifetime
τ_F	natural lifetime
t, Δt	time, time-lag
t_{exp}	camera exposure time
t_{CPU}	execution time on CPU
t_{cyc}	camera kinetic cycle time
Θ	beam divergence angle
T	temperature
T_1	electronic triplet state
U_n	Lommel functions
u, v	optical coordinates
w	beam waist ($1/e^2$ radius)
w_0	minimum beam waist
x_R	Rayleigh length
x,y,z	spatial coordinates

List of Figures

List of Tables

Bibliography

[1] E. Betzig and R. J. Chichester. "Single molecules observed by near-field scanning optical microscopy". *Science* 262:5138 (1993), 1422–1425.

[2] T. Funatsu, Y. Harada, M. Tokunaga, K. Saito, and T. Yanagida. "Imaging of single fluorescent molecules and individual ATP turnovers by single myosin molecules in aqueous solution". *Nature* 374:6522 (1995), 555–559.

[3] A. Yildiz and P. R. Selvin. "Fluorescence imaging with one nanometer accuracy: application to molecular motors". *Accounts of Chemical Research* 38:7 (2005), 574–582.

[4] B. Huang, M. Bates, and X. Zhuang. "Super-resolution fluorescence microscopy." *Annual Review of Biochemistry* 78 (2009), 993–1016.

[5] T. Schmidt, G. Schütz, W Baumgartner, H. Gruber, and H Schindler. "Imaging of single molecule diffusion". *Proceedings of the National Academy of Sciences of the USA* 93:7 (1996), 2926–2929.

[6] Y. Sako, S. Minoghchi, and T. Yanagida. "Single-molecule imaging of EGFR signalling on the surface of living cells". *Nature Cell Biology* 2:3 (2000), 168–172.

[7] J. Adler, A. I. Shevchuk, P. Novak, Y. E. Korchev, and I. Parmryd. "Plasma membrane topography and interpretation of single-particle tracks". *Nature Methods* 7:3 (2010), 170–171.

[8] A Dupont, M Gorelashvili, V Schüller, F Wehnekamp, D Arcizet, Y Katayama, D. Lamb, and D Heinrich. "Three-dimensional single-particle tracking in live cells: news from the third dimension". *New Journal of Physics* 15:7 (2013), 075008.

[9] J. P. Siebrasse, R. Veith, A. Dobay, H. Leonhardt, B. Daneholt, and U. Kubitscheck. "Discontinuous movement of mRNP particles in nucleoplasmic regions devoid of chromatin". *Proceedings of the National Academy of Sciences of the USA* 105:51 (2008), 20291–20296.

[10] J. P. Siebrasse, T. Kaminski, and U. Kubitscheck. "Nuclear export of single native mRNA molecules observed by light sheet fluorescence microscopy." *Proceedings of the National Academy of Sciences of the USA* 109:24 (2012), 9426–9431.

[11] F. Persson, M. Lindén, C. Unoson, and J. Elf. "Extracting intracellular diffusive states and transition rates from single-molecule tracking data". *Nature Methods* (2013).

[12] J. G. Ritter, R. Veith, A. Veenendaal, J. P. Siebrasse, and U. Kubitscheck. "Light sheet microscopy for single molecule tracking in living tissue." *PLoS ONE* 5:7 (2010), e11639.

[13] M. Friedrich, R. Nozadze, Q. Gan, M. Zelman-Femiak, V. Ermolayev, T. U. Wagner, and G. S. Harms. "Detection of single quantum dots in model organisms with sheet illumination microscopy". *Biochemical and Biophysical Research Communications* 390:3 (2009), 722–727.

[14] H. P. Kao and A. S. Verkman. “Tracking of single fluorescent particles in three dimensions: use of cylindrical optics to encode particle position.” *Biophysical Journal* 67:3 (1994), 1291–1300.

[15] Y. Katayama, O. Burkacky, M. Meyer, C. Bräuchle, E. Gratton, and D. C. Lamb. “Real-time nanomicroscopy via three-dimensional single-particle tracking.” *Chemphyschem* 10:14 (2009), 2458–2464.

[16] M. F. Juette and J. Bewersdorf. “Three-dimensional tracking of single fluorescent particles with submillisecond temporal resolution.” *Nano Letters* 10:11 (2010), 4657–4663.

[17] N. P. Wells, G. A. Lessard, P. M. Goodwin, M. E. Phipps, P. J. Cutler, D. S. Lidke, B. S. Wilson, and J. H. Werner. “Time-resolved three-dimensional molecular tracking in live cells.” *Nano Letters* 10:11 (2010), 4732–4737.

[18] R. Veith, T. Sorkalla, E. Baumgart, J. Anzt, H. Häberlein, S. Tyagi, J. P. Siebrasse, and U. Kubitscheck. “Balbiani ring mRNPs diffuse through and bind to clusters of large intranuclear molecular structures”. *Biophysical Journal* 99:8 (2010), 2676–2685.

[19] F. Miralles, L.-G. Öfverstedt, N. Sabri, Y. Aissouni, U. Hellman, U. Skoglund, and N. Visa. “Electron tomography reveals posttranscriptional binding of pre-mRNPs to specific fibers in the nucleoplasm”. *The Journal of Cell Biology* 148:2 (2000), 271–282.

[20] A. L. Meskes. “Mikroskopie mit Hochauflösung in drei Dimensionen”. Diploma thesis. Universität Bonn, 2011.

[21] M. Heilemann, S. van de Linde, M. Schüttpelz, R. Kasper, B. Seefeldt, A. Mukherjee, P. Tinnefeld, and M. Sauer. “Subdiffraction-resolution fluorescence imaging with conventional fluorescent probes”. *Angewandte Chemie International Edition* 47:33 (2008), 6172–6176.

[22] F. Kotzur. “3D-Lokalisierung von Nanopartikeln und einzelnen Molekülen auf freistehenden Modellmembranen”. Master thesis. Universität Bonn, 2012.

[23] M. Minsky. *Microscopy apparatus*. US Patent 3,013,467. 1961.

[24] M. D. Egger and M. Petran. “New reflected-light microscope for viewing unstained brain and ganglion cells”. *Science* 157:3786 (1967), 305–307.

[25] J. White, W. Amos, and M Fordham. “An evaluation of confocal versus conventional imaging of biological structures by fluorescence light microscopy.” *The Journal of Cell Biology* 105:1 (1987), 41–48.

[26] G. van Meer, E. Stelzer, R. W. Wijnaendts-van Resandt, and K. Simons. “Sorting of sphingolipids in epithelial (Madin-Darby canine kidney) cells.” *The Journal of Cell Biology* 105:4 (1987), 1623–1635.

[27] M. Chalfie, Y. Tu, G. Euskirchen, W. W. Ward, and D. C. Prasher. “Green fluorescent protein as a marker for gene expression”. *Science* 263:5148 (1994), 802–805.

[28] L Silvestri, A Bria, L Sacconi, G Iannello, and F. Pavone. “Confocal light sheet microscopy: micron-scale neuroanatomy of the entire mouse brain”. *Optics Express* 20:18 (2012), 20582–20598.

[29] S. Kumar, D. Wilding, M. B. Sikkel, A. R. Lyon, K. T. Macleod, and C. Dunsby. “High-speed 2D and 3D fluorescence microscopy of cardiac myocytes.” *Optics Express* 19:15 (2011), 13839–13847.

[30] A. Maizel, D. von Wangenheim, F. Federici, J. Haseloff, and E. H. K. Stelzer. “High-resolution live imaging of plant growth in near physiological bright conditions using light sheet fluorescence microscopy.” eng. *Plant Journal* 68:2 (2011), 377–385.

[31] D. A. Agard and J. W. Sedat. “Three-dimensional architecture of a polytene nucleus”. *Nature* 302:5910 (1983), 676–681.

[32] W. Supatto, T. V. Truong, D. Débarre, and E. Beaurepaire. “Advances in multiphoton microscopy for imaging embryos.” *Current Opinion in Genetics & Development* (2011).

[33] M. Tokunaga, N. Imamoto, and K. Sakata-Sogawa. “Highly inclined thin illumination enables clear single-molecule imaging in cells”. *Nature Methods* 5:2 (2008), 159–161.

[34] D. Axelrod. “Cell-substrate contacts illuminated by total internal reflection fluorescence.” *The Journal of Cell Biology* 89:1 (1981), 141–145.

[35] P. J. Keller, A. D. Schmidt, J. Wittbrodt, and E. H. K. Stelzer. “Reconstruction of zebrafish early embryonic development by scanned light sheet microscopy.” *Science* 322:5904 (2008), 1065–1069.

[36] H. Siedentopf and R. Zsigmondy. “Uber Sichtbarmachung und Größenbestimmung ultramikoskopischer Teilchen, mit besonderer Anwendung auf Goldrubingläser”. *Annalen der Physik* 315:1 (1902), 1–39.

[37] A. H. Voie, D. H. Burns, and F. A. Spelman. “Orthogonal-plane fluorescence optical sectioning: three-dimensional imaging of macroscopic biological specimens.” *Journal of Microscopy* 170:3 (1993), 229–236.

[38] J. Huisken, J. Swoger, F. D. Bene, J. Wittbrodt, and E. H. K. Stelzer. “Optical sectioning deep inside live embryos by selective plane illumination microscopy.” *Science* 305:5686 (2004), 1007–1009.

[39] H.-U. Dodt, U. Leischner, A. Schierloh, N. Jährling, C. P. Mauch, K. Deininger, J. M. Deussing, M. Eder, W. Zieglgänsberger, and K. Becker. “Ultramicroscopy: three-dimensional visualization of neuronal networks in the whole mouse brain.” *Nature Methods* 4:4 (2007), 331–336.

[40] J. G. Ritter, R. Veith, J.-P. Siebrasse, and U. Kubitscheck. “High-contrast single-particle tracking by selective focal plane illumination microscopy.” *Optics Express* 16:10 (2008), 7142–7152.

[41] J. Huisken and D. Y. R. Stainier. “Even fluorescence excitation by multidirectional selective plane illumination microscopy (mSPIM).” *Optics Letters* 32:17 (2007), 2608–2610.

[42] R. Tomer, K. Khairy, F. Amat, and P. J. Keller. “Quantitative high-speed imaging of entire developing embryos with simultaneous multiview light-sheet microscopy.” *Nature Methods* 9:7 (2012), 755–763.

[43] U. Krzic, S. Gunther, T. E. Saunders, S. J. Streichan, and L. Hufnagel. “Multiview light-sheet microscope for rapid in toto imaging.” *Nature Methods* 9:7 (2012), 730–733.

[44] T. V. Truong, W. Supatto, D. S. Koos, J. M. Choi, and S. E. Fraser. “Deep and fast live imaging with two-photon scanned light-sheet microscopy.” *Nature Methods* 8:9 (2011), 757–760.

[45] F. O. Fahrbach and A. Rohrbach. “A line scanned light-sheet microscope with phase shaped self-reconstructing beams.” *Optics Express* 18:23 (2010), 24229–24244.

[46] A. Kaufmann, M. Mickoleit, M. Weber, and J. Huisken. “Multilayer mounting enables long-term imaging of zebrafish development in a light sheet microscope”. *Development* 139:17 (2012), 3242–3247.

[47] P. J. Keller, A. D. Schmidt, A. Santella, K. Khairy, Z. Bao, J. Wittbrodt, and E. H. K. Stelzer. "Fast, high-contrast imaging of animal development with scanned light sheet-based structured-illumination microscopy." *Nature Methods* 7:8 (2010), 637–642.

[48] M. Weber and J. Huisken. "Light sheet microscopy for real-time developmental biology." *Current Opinion in Genetics & Development* 21:5 (2011), 566–572.

[49] T. A. Planchon, L. Gao, D. E. Milkie, M. W. Davidson, J. A. Galbraith, C. G. Galbraith, and E. Betzig. "Rapid three-dimensional isotropic imaging of living cells using Bessel beam plane illumination." *Nature Methods* 8:5 (2011), 417–426.

[50] Y. Wu, A. Ghitani, R. Christensen, A. Santella, Z. Du, G. Rondeau, Z. Bao, D. Colón-Ramos, and H. Shroff. "Inverted selective plane illumination microscopy (iSPIM) enables coupled cell identity lineaging and neurodevelopmental imaging in Caenorhabditis elegans." *Proceedings of the National Academy of Sciences of the USA* 108:43 (2011), 17708–17713.

[51] Y. Li, Y. S. Hu, and H. Cang. "Light Sheet Microscopy for Tracking Single Molecules on the Apical Surface of Living Cells". *Journal of Physical Chemistry B* (2013).

[52] J. C. M. Gebhardt, D. M. Suter, R. Roy, Z. W. Zhao, A. R. Chapman, S. Basu, T. Maniatis, and X. S. Xie. "Single-molecule imaging of transcription factor binding to DNA in live mammalian cells". *Nature Methods* 10:5 (2013), 421–426.

[53] J. Huisken and D. Y. R. Stainier. "Selective plane illumination microscopy techniques in developmental biology." *Development* 136:12 (2009), 1963–1975.

[54] A. G. York, A. Ghitani, A. Vaziri, M. W. Davidson, and H. Shroff. "Confined activation and subdiffractive localization enables whole-cell PALM with genetically expressed probes". *Nature Methods* 8:4 (2011), 327–333.

[55] F. C. Zanacchi, Z. Lavagnino, M. P. Donnorso, A. D. Bue, L. Furia, M. Faretta, and A. Diaspro. "Live-cell 3D super-resolution imaging in thick biological samples." *Nature Methods* 8:12 (2011), 1047–1049.

[56] J. R. Lakowicz. *Principles of fluorescence spectroscopy*. 3rd Edition. Springer, 2006.

[57] J. Vogelsang, C. Steinhauer, C. Forthmann, I. H. Stein, B. Person-Skegro, T. Cordes, and P. Tinnefeld. "Make them blink: probes for super-resolution microscopy." *Chemphyschem* 11:12 (2010), 2475–2490.

[58] R. Steinmeyer, A. Noskov, C. Krasel, I. Weber, C. Dees, and G. Harms. "Improved Fluorescent Proteins for Single-Molecule Research in Molecular Tracking and Co-Localization". English. *Journal of Fluorescence* 15:5 (2005), 707–721.

[59] R. B. Altman, D. S. Terry, Z. Zhou, Q. Zheng, P. Geggier, R. A. Kolster, Y. Zhao, J. A. Javitch, J. D. Warren, and S. C. Blanchard. "Cyanine fluorophore derivatives with enhanced photostability". *Nature Methods* 9:1 (2012), 68–71.

[60] F. Pinaud, S. Clarke, A. Sittner, and M. Dahan. "Probing cellular events, one quantum dot at a time". *Nature Methods* 7:4 (2010), 275–285.

[61] T. Xia, N. Li, and X. Fang. "Single-Molecule Fluorescence Imaging in Living Cells". *Annual Review of Physical Chemistry* 64 (2013), 459–480.

[62] H. Hong, T. Gao, and W. Cai. "Molecular imaging with single-walled carbon nanotubes". *Nano Today* 4:3 (2009), 252–261.

[63] E. Wolf and M. Born. *Principles of optics*. Vol. 6. Pergamon Press, 1980.

[64] B. Zhang, J. Zerubia, and J.-C. Olivo-Marin. “Gaussian approximations of fluorescence microscope point-spread function models.” *Applied Optics* 46:10 (2007), 1819–1829.

[65] D. Patra, I. Gregor, and J. Enderlein. “Image analysis of defocused single-molecule images for three-dimensional molecule orientation studies”. *The Journal of Physical Chemistry A* 108:33 (2004), 6836–6841.

[66] R. E. Thompson, D. R. Larson, and W. W. Webb. “Precise nanometer localization analysis for individual fluorescent probes.” *Biophysical Journal* 82:5 (2002), 2775–2783.

[67] K. I. Mortensen, L. S. Churchman, J. A. Spudich, and H. Flyvbjerg. “Optimized localization analysis for single-molecule tracking and super-resolution microscopy.” *Nature Methods* 7:5 (2010), 377–381.

[68] H. Deschout, K. Neyts, and K. Braeckmans. “The influence of movement on the localization precision of sub-resolution particles in fluorescence microscopy.” *Journal of Biophotonics* 5:1 (2012), 97–109.

[69] A. Kusumi, C. Nakada, K. Ritchie, K. Murase, K. Suzuki, H. Murakoshi, R. S. Kasai, J. Kondo, and T. Fujiwara. “Paradigm shift of the plasma membrane concept from the two-dimensional continuum fluid to the partitioned fluid: high-speed single-molecule tracking of membrane molecules”. *Annual Review of Biophysical and Biomolecular Structure* 34 (2005), 351–378.

[70] D Axelrod, D. Koppel, J Schlessinger, E. Elson, and W. Webb. “Mobility measurement by analysis of fluorescence photobleaching recovery kinetics”. *Biophysical Journal* 16:9 (1976), 1055–1069.

[71] E. L. Elson and D. Magde. “Fluorescence correlation spectroscopy. I. Conceptual basis and theory”. *Biopolymers* 13:1 (1974), 1–27.

[72] N. O. Petersen, P. L. Höddelius, P. Wiseman, O Seger, and K. Magnusson. “Quantitation of membrane receptor distributions by image correlation spectroscopy: concept and application”. *Biophysical Journal* 65:3 (1993), 1135–1146.

[73] S. Semrau and T. Schmidt. “Particle image correlation spectroscopy (PICS): retrieving nanometer-scale correlations from high-density single-molecule position data”. *Biophysical Journal* 92:2 (2007), 613–621.

[74] M. J. Saxton and K. Jacobson. “Single-particle tracking: applications to membrane dynamics”. *Annual Review of Biophysics and Biomolecular Structure* 26:1 (1997), 373–399.

[75] K. Braeckmans, L. Peeters, N. N. Sanders, S. C. De Smedt, and J. Demeester. “Three-dimensional fluorescence recovery after photobleaching with the confocal scanning laser microscope”. *Biophysical Journal* 85:4 (2003), 2240–2252.

[76] C. Lanctôt, T. Cheutin, M. Cremer, G. Cavalli, and T. Cremer. “Dynamic genome architecture in the nuclear space: regulation of gene expression in three dimensions”. *Nature Reviews Genetics* 8:2 (2007), 104–115.

[77] B. Shuang, J. Chen, L. Kisley, and C. F. Landes. “Troika of single particle tracking programing: SNR enhancement, particle identification, and mapping”. *Physical Chemistry Chemical Physics* (2014).

[78] M. J. Mlodzianoski, M. F. Juette, G. L. Beane, and J. Bewersdorf. “Experimental characterization of 3D localization techniques for particle-tracking and super-resolution microscopy.” *Optics Express* 17:10 (2009), 8264–8277.

[79] M. K. Cheezum, W. F. Walker, and W. H. Guilford. "Quantitative comparison of algorithms for tracking single fluorescent particles." *Biophysical Journal* 81:4 (2001), 2378–2388.

[80] R. Parthasarathy. "Rapid, accurate particle tracking by calculation of radial symmetry centers." *Nature Methods* 9:7 (2012), 724–726.

[81] C. S. Smith, N. Joseph, B. Rieger, and K. A. Lidke. "Fast, single-molecule localization that achieves theoretically minimum uncertainty." *Nature Methods* 7:5 (2010), 373–375.

[82] T Dertinger, R Colyer, G Iyer, S Weiss, and J Enderlein. "Fast, background-free, 3D super-resolution optical fluctuation imaging (SOFI)". *Proceedings of the National Academy of Sciences of the USA* 106:52 (2009), 22287–22292.

[83] L. Weimann, K. A. Ganzinger, J. McColl, K. L. Irvine, S. J. Davis, N. J. Gay, C. E. Bryant, and D. Klenerman. "A Quantitative Comparison of Single-Dye Tracking Analysis Tools Using Monte Carlo Simulations". *PloS ONE* 8:5 (2013), e64287.

[84] A. Serge, N. Bertaux, H. Rigneault, and D. Marguet. "Dynamic multiple-target tracing to probe spatiotemporal cartography of cell membranes". *Nature Methods* 5:8 (2008), 687–694.

[85] P.-H. Wu, A. Agarwal, H. Hess, P. P. Khargonekar, and Y. Tseng. "Analysis of Video-Based Microscopic Particle Trajectories Using Kalman Filtering". *Biophysical Journal* 98:12 (2010), 2822–2830.

[86] G. J. Schuetz, M. Axmann, and H. Schindler. "Imaging Single Molecules in Three Dimensions". *Single Molecules* 2:2 (2001), 69–74.

[87] H. C. Berg. "How to track bacteria". *Review of Scientific Instruments* 42:6 (1971), 868–871.

[88] G. A. Lessard, P. M. Goodwin, and J. H. Werner. "Three-dimensional tracking of individual quantum dots". *Applied Physics Letters* 91:22 (2007), 224106.

[89] S. R. P. Pavani, M. A. Thompson, J. S. Biteen, S. J. Lord, N. Liu, R. J. Twieg, R. Piestun, and W. Moerner. "Three-dimensional, single-molecule fluorescence imaging beyond the diffraction limit by using a double-helix point spread function". *Proceedings of the National Academy of Sciences of the USA* 106:9 (2009), 2995–2999.

[90] E. Toprak, H. Balci, B. H. Blehm, and P. R. Selvin. "Three-dimensional particle tracking via bifocal imaging." *Nano Letters* 7:7 (2007), 2043–2045.

[91] S. Ram, E. S. Ward, and R. J. Ober. "How accurately can a single molecule be localized in three dimensions using a fluorescence microscope?" *Proceedings of SPIE* 5699 (2005), 426–435.

[92] S. Ram, P. Prabhat, J. Chao, E. S. Ward, and R. J. Ober. "High accuracy 3D quantum dot tracking with multifocal plane microscopy for the study of fast intracellular dynamics in live cells." *Biophysical Journal* 95:12 (2008), 6025–6043.

[93] S. Abrahamsson, J. Chen, B. Hajj, S. Stallinga, A. Y. Katsov, J. Wisniewski, G. Mizuguchi, P. Soule, F. Mueller, C. D. Darzacq, et al. "Fast multicolor 3D imaging using aberration-corrected multifocus microscopy". *Nature Methods* 10:1 (2012), 60–63.

[94] E. A. K. Cohen and R. J. Ober. "Image registration error analysis with applications in single molecule microscopy". *IEEE International Symposium on Biomedical Imaging*. 2012.

[95] S. R. P. Pavani and R. Piestun. “Three dimensional tracking of fluorescent microparticles using a photon-limited double-helix response system.” *Optics Express* 16:26 (2008), 22048–22057.

[96] I. Izeddin, M. E. Beheiry, J. Andilla, D. Ciepielewski, X. Darzacq, and M. Dahan. “PSF shaping using adaptive optics for three-dimensional single-molecule super-resolution imaging and tracking.” *Optics Express* 20:5 (2012), 4957–4967.

[97] C. Sheppard, D. Hamilton, and I. Cox. “Optical microscopy with extended depth of field”. *Proceedings of the Royal Society of London. A. Mathematical and Physical Sciences* 387:1792 (1983), 171–186.

[98] A. Rohrbach and E. H. Stelzer. “Three-dimensional position detection of optically trapped dielectric particles”. *Journal of Applied Physics* 91:8 (2002), 5474–5488.

[99] Q. Wang and W. E. Moerner. “An Adaptive Anti-Brownian ELectrokinetic trap with real-time information on single-molecule diffusivity and mobility.” *ACS Nano* 5:7 (2011), 5792–5799.

[100] A. Einstein. “Ueber die von der molekularkinetischen Theorie der Waerme geforderte Bewegung von in ruhenden Fluessigkeiten suspendierten Teilchen”. *Annalen der Physik* 322:8 (1905), 549–560.

[101] E. Sackmann and R. Merkel. *Lehrbuch der Biophysik*. Wiley-VCH Berlin, 2010.

[102] P. Walde, K. Cosentino, H. Engel, and P. Stano. “Giant vesicles: preparations and applications”. *ChemBioChem* 11:7 (2010), 848–865.

[103] B. Alberts. *Molecular Biology of the Cell*. 4th edition. Garland, 2002.

[104] N. Kahya, D. Scherfeld, K. Bacia, and P. Schwille. “Lipid domain formation and dynamics in giant unilamellar vesicles explored by fluorescence correlation spectroscopy”. *Journal of Structural Biology* 147:1 (2004), 77–89.

[105] J. Korlach, P. Schwille, W. W. Webb, and G. W. Feigenson. “Characterization of lipid bilayer phases by confocal microscopy and fluorescence correlation spectroscopy”. *Proceedings of the National Academy of Sciences of the USA* 96:15 (1999), 8461–8466.

[106] M. I. Angelova and D. S. Dimitrov. “Liposome electroformation”. *Faraday Discussions of the Chemical Society* 81 (1986), 303–311.

[107] R. F. de Almeida, A. Fedorov, and M. Prieto. “Sphingomyelin / phosphatidylcholine / cholesterol phase diagram: boundaries and composition of lipid rafts”. *Biophysical Journal* 85:4 (2003), 2406–2416.

[108] B. Daneholt. “Assembly and transport of a premessenger RNP particle”. *Proceedings of the National Academy of Sciences of the USA* 98:13 (2001), 7012–7017.

[109] R. Veith. “Mobilität endogener mRNA im chromatinfreien Nukleoplasma der Speicheldrüsenzellkerne von Chironomus tentans”. PhD thesis. Bonn University, 2011.

[110] B. Daneholt. “Packing and delivery of a genetic message”. *Chromosoma* 110:3 (2001), 173–185.

[111] L. Wieslander. “The Balbiani ring multigene family: coding repetitive sequences and evolution of a tissue-specific cell function”. *Progress in Nucleic Acid Research and Molecular Biology* 48 (1994), 275–313.

[112] G. Paulsson, K. Bernholm, and L. Wieslander. “Conserved and variable repeat structures in the Balbiani ring gene family in Chironomus tentans.” *Journal of Molecular Evolution* 35:3 (1992), 205–216.

[113] T. Wurtz, A. Loennroth Annroth, L. Ovchinnikov, U. Skoglund, and B. Daneholt. “Isolation and initial characterization of a specific premessenger ribonucleoprotein particle”. *Proceedings of the National Academy of Sciences of the USA* 87:2 (1990), 831–835.

[114] Y. Deng and J. W. Shaevitz. “Effect of aberration on height calibration in three-dimensional localization-based microscopy and particle tracking.” *Applied Optics* 48:10 (2009), 1886–1890.

[115] T. Kaminski, J.-H. Spille, C. Nietzel, J. P. Siebrasse, and U. Kubitscheck. “Nuclear trafficking and export of single, native mRNPs in Chironomus tentans salivary gland cells”. *Methods in Molecular Biology* (2013).

[116] M. Muselli. “Simple expressions for success run distributions in bernoulli trials”. *Statistics & Probability Letters* 31:2 (1996), 121 –128.

[117] J. G. Ritter, J.-H. Spille, T. Kaminski, and U. Kubitscheck. “A cylindrical zoom lens unit for adjustable optical sectioning in light sheet microscopy.” *Biomedical Optics Express* 2:1 (2010), 185–193.

[118] F. Long, S. Zeng, and Z.-L. Huang. “Localization-based super-resolution microscopy with an sCMOS camera Part II: Experimental methodology for comparing sCMOS with EMCCD cameras”. *Optics Express* 20:16 (2012), 17741–17759.

[119] L. Holtzer, T. Meckel, and T. Schmidt. “Nanometric three-dimensional tracking of individual quantum dots in cells”. *Applied Physics Letters* 90:5 (2007), 053902.

[120] B. Huang, S. A. Jones, B. Brandenburg, and X. Zhuang. “Whole-cell 3D STORM reveals interactions between cellular structures with nanometer-scale resolution.” *Nature Methods* 5:12 (2008), 1047–1052.

[121] J.-H. Spille, T. Kaminski, H.-P. Königshoven, and U. Kubitscheck. “Dynamic three-dimensional tracking of single fluorescent nanoparticles deep inside living tissue.” *Optics Express* 20:18 (2012), 19697–19707.

[122] D. Ernst and J. Koehler. “Measuring a diffusion coefficient by single-particle tracking: statistical analysis of experimental mean squared displacement curves”. *Physical Chemistry Chemical Physics* 15:3 (2013), 845–849.

[123] R. Henriques, M. Lelek, E. F. Fornasiero, F. Valtorta, C. Zimmer, and M. M. Mhlanga. “QuickPALM: 3D real-time photoactivation nanoscopy image processing in ImageJ”. *Nature Methods* 7:5 (2010), 339–340.

[124] S. Wolter, A. Löschberger, T. Holm, S. Aufmkolk, M.-C. Dabauvalle, S. van de Linde, and M. Sauer. “rapidSTORM: accurate, fast open-source software for localization microscopy.” *Nature Methods* 9:11 (2012), 1040–1041.

[125] M. Speidel, A. Jonás, and E.-L. Florin. “Three-dimensional tracking of fluorescent nanoparticles with subnanometer precision by use of off-focus imaging.” *Optics Letters* 28:2 (2003), 69–71.

[126] *Piezo Tutorial*. http://www.physikinstrumente.com/en/, accessed 10.07.2013 12:27. Physik Instrumente, 2013.

[127] U. Schmitz-Ziffels. “Fluoreszenzmarker der hochauflösenden Einzelmolekül-mikroskopie”. PhD thesis. University of Bonn, 2013.

[128] M. J. Saxton. “Lateral diffusion in an archipelago. Single-particle diffusion.” *Biophysical Journal* 64:6 (1993), 1766–1780.

[129] G Adam and M Delbrück. “Reduction of dimensionality in biological diffusion processes”. *Structural Chemistry and Molecular Biology* 198 (1968).

[130] J. Elf, G.-W. Li, and X. S. Xie. “Probing transcription factor dynamics at the single-molecule level in a living cell”. *Science* 316:5828 (2007), 1191–1194.

[131] C. von Middendorff, A. Egner, C. Geisler, S. W. Hell, and A. Schönle. “Isotropic 3D Nanoscopy based on single emitter switching.” *Optics Express* 16:25 (2008), 20774–20788.

[132] M. Badieirostami, M. D. Lew, M. A. Thompson, and W. E. Moerner. “Three-dimensional localization precision of the double-helix point spread function versus astigmatism and biplane.” *Applied Physics Letters* 97:16 (2010), 161103.

[133] R. Starr, S. Stahlheber, and A. Small. “Fast maximum likelihood algorithm for localization of fluorescent molecules”. *Optics Letters* 37:3 (2012), 413–415.

[134] S. Ram, D. Kim, R. J. Ober, and E. S. Ward. “3D Single Molecule Tracking with Multifocal Plane Microscopy Reveals Rapid Intercellular Transferrin Transport at Epithelial Cell Barriers”. *Biophysical Journal* 103:7 (2012), 1594–1603.

[135] K. Kylberg, B. Björkroth, B. Ivarsson, N. Fomproix, and B. Daneholt. “Close coupling between transcription and exit of mRNP from the cell nucleus”. *Experimental Cell Research* 314:8 (2008), 1708–1720.

[136] S. Krull, J. Dörries, B. Boysen, S. Reidenbach, L. Magnius, H. Norder, J. Thyberg, and V. C. Cordes. “Protein Tpr is required for establishing nuclear pore-associated zones of heterochromatin exclusion.” *EMBO Journal* 29:10 (2010), 1659–1673.

[137] M. F. Juette, F. E. Rivera-Molina, D. K. Toomre, and J. Bewersdorf. “Adaptive optics enables three-dimensional single particle tracking at the sub-millisecond scale”. *Applied Physics Letters* 102:17 (2013), 173702–173702.

[138] J. Chao, S. Ram, E. S. Ward, and R. J. Ober. “Ultrahigh accuracy imaging modality for super-localization microscopy”. *Nature Methods* 10:4 (2013), 335–338.

[139] H. Ma, H. Kawai, E. Toda, S. Zeng, and Z.-L. Huang. “Localization-based super-resolution microscopy with an sCMOS camera part III: camera embedded data processing significantly reduces the challenges of massive data handling”. *Optics Letters* 38:11 (2013), 1769–1771.

Publications

Peer-reviewed articles

[1] K. Pelka, J. Zimmermann, L. Labzin, K. Phulphagar, R. Stahl, **J.-H. Spille**, S. Hoening, and E. Latz. "TLR8 traffics with UNC93B1 via the cell surface but signals from AP-2 independent endosomal compartments." *submitted* (2013).

[2] G. O. Bodea, **J.-H. Spille**, P. Abe, A. Senturk Andersson, A. Acker-Palmer, R. Stumm, U. Kubitscheck, and S. Blaess. "Reelin and CXCL12 regulate distinct migratory behaviors during the development of the dopaminergic system." *Development* (2013), *in press.*

[3] **J.-H. Spille**, T. Kaminski, H.-P. Königshoven, and U. Kubitscheck. "Dynamic three-dimensional tracking of single fluorescent nanoparticles deep inside living tissue." *Optics Express* 20:18 (2012), 19697–19707.

[4] **J.-H. Spille**, A. Zürn, C. Hoffmann, M. J. Lohse, and G. S. Harms. "Rotational diffusion of the alpha(2a) adrenergic receptor revealed by FlAsH labeling in living cells." *Biophysical Journal* 100:4 (2011), 1139–1148.

[5] J. G. Ritter, **J.-H. Spille**, T. Kaminski, and U. Kubitscheck. "A cylindrical zoom lens unit for adjustable optical sectioning in light sheet microscopy." *Biomedical Optics Express* 2:1 (2010), 185–193.

in preparation

[6] **J.-H. Spille**, T. Kaminski, K. Scherer, J. S. Rinne, A. Heckel, and U. Kubitscheck. "Extended, sensitive and fast 3D-tracking of single molecules and RNA particles in living tissue." (2013).

Book chapters

[7] T. Kaminski, **J.-H. Spille**, C. Nietzel, J. P. Siebrasse, and U. Kubitscheck. "Nuclear trafficking and export of single, native mRNPs in Chironomus tentans salivary gland cells". *Methods in Molecular Biology* (2013).

Invited publications

[8] **J.-H. Spille**, J. P. Siebrasse, T. Kaminski, and U. Kubitscheck. "Single molecule light sheet microscopy." *G.I.T. Imaging & Microscopy* 3 (2012), 30–32.

Conference contributions

Platform presentations

[1] **J.-H. Spille**, T. Kaminski, K. Scherer, F. Kotzur, and U. Kubitscheck. "Fast 3D single molecule tracking with high sensitivity". *Focus on Microscopy* (24.03.2013).

[2] **J.-H. Spille**. "Applications of light sheet microscopy". *Optics, forces & development. In vivo 3D-microscopy for the analysis of cell behaviour in developing embryos* (14.01.2013).

[3] **J.-H. Spille**. "Tiefer, schneller, länger – 3D Verfolgung einzelner Moleküle in lebenden Zellen". *Doktorandenforum der Studienstiftung des deutschen Volkes* (8.11.2012).

[4] **J.-H. Spille**, T. Kaminski, and U. Kubitscheck. "Faster, darker, longer: Improved Dynamic 3D Particle Tracking". *4th Light Sheet Microscopy Workshop* (19.09.2012).

[5] **J.-H. Spille**, T. Kaminski, and U. Kubitscheck. "Dynamic 3D particle tracking deep inside living tissue". *Focus on Microscopy* (1.04.2012).

[6] **J.-H. Spille**. "Verfolgung einzelner Moleküle in 3D – mit Brille". *Doktorandenforum der Studienstiftung des deutschen Volkes der Studienstiftung des deutschen Volkes* (17.11.2011).

[7] **J.-H. Spille**, T. Kaminski, J. Ritter, and U. Kubitscheck. "Extended 3D single molecule tracking inside living cells". *3rd Light Sheet Microscopy Workshop* (13.10.2011).

[8] **J.-H. Spille**. "Einzelmolekülverfolgung in der dritten Dimension". *Doktorandenforum der Studienstiftung des deutschen Volkes* (2.06.2011).

[9] **J.-H. Spille**, J. Ritter, T. Kaminski, and U. Kubitscheck. "Astigmatic light sheet microscopy allows 3D localization deep inside living cells". *Focus on Microscopy* (17.04.2011).

[10] **J.-H. Spille**, J. Ritter, T. Kaminski, J.-P. Siebrasse, and U. Kubitscheck. "3D tracking of single fluorescent molecules with astigmatic imaging of a light-sheet illuminated sample". *The Second Light Sheet based Fluorescence Microscopy Workshop* (2.09.2010).

Poster presentations

[11] **J.-H. Spille**, T. Kaminski, and U. Kubitscheck. "A Feedback Loop for Dynamic 3D Tracking Deep Inside Living Tissue". *IEEE International Symposium on Biomedical Imaging* (2.05.2012).

[12] **J.-H. Spille**, T. Kaminski, and U. Kubitscheck. "3D tracking of single fluorescent molecules". *34th Annual Meeting of the German Society for Cell Biology* (30.03.2011).

[13] **J.-H. Spille**, J. Ritter, T. Kaminski, and U. Kubitscheck. "3D tracking of single fluorescent molecules". *Annual Meeting of the German Biophysical Society* (3.10.2010).

[14] **J.-H. Spille**, J. Ritter, and U. Kubitscheck. "Light-sheet based microscopy for 3D single particle tracking". *EMBO Workshop Advanced Light Microscopy - 10th International ELMI Meeting* (18.05.2010).

[15] **J.-H. Spille** and U. Kubitscheck. "3D Single Particle Tracking using Light-Sheet Illumination". *XII. Annual Linz Winter Workshop* (5.02.2010).

Co-authored contributions

[16] G. O. Bodea, **J.-H. Spille**, P. Abe, A. S. Andersson, A. Acker-Palmer, R. Stumm, U. Kubitscheck, and S. Blaess. "Molecular mechanisms regulating neuronal migration during the development of the dopaminergic system". *Neuroscience* (9.11.2013).

[17] E. Baumgart, **J.-H. Spille**, and U. Kubitscheck. "How to upgrade your light sheet microscope to a true confocal microscope". *Focus on Microscopy* (24.03.2013).

[18] F. Kotzur, **J.-H. Spille**, K. Scherer, and U. Kubitscheck. "3D Single-molecule tracking on vesicles". *Focus on Microscopy* (24.03.2013).

[19] K. Bennett, **J.-H. Spille**, E. Toda, T. Maruno, and T. Takahashi. "Impact of CMOS Rolling Shutter in Super-Resolution Single Molecule Tracking Localization Microscopy". *Single Molecule Biophysics* (6.01.2013).

[20] J.-P. Siebrasse, M. Schiener, T. Kaminski, C. Nietzel, **J.-H. Spille**, and U. Kubitscheck. "Single Molecule Kinetics of the RNA Helicase Dbp5". *The Complex Life of mRNA* (7.10.2012).

[21] E. Baumgart, **J.-H. Spille**, and U. Kubitscheck. "Rapid Light Sheet Fluorescence Microscopy with Enhanced Optical Resolution". *4th Light Sheet Fluorescence Microscopy Workshop* (19.09.2012).

[22] F. Kotzur, **J.-H. Spille**, K. Scherer, and U. Kubitscheck. "3D Single Particle Tracking on Vesicles". *4th Light Sheet Microscopy Workshop* (19.09.2012).

[23] G. O. Bodea, **J.-H. Spille**, U. Kubitscheck, and S. Blaess. "Unraveling the molecular mechanisms regulating dopaminergic neuron migration in the developing midbrain". *8th FENS Forum of Neuroscience* (14.07.2012).

[24] E. Baumgart, **J.-H. Spille**, H. Spiecker, and U. Kubitscheck. "Rapid Light Sheet Fluorescence Microscopy with Confocal Slit Detection". *Focus on Microscopy* (1.04.2012).

[25] E. Baumgart, **J.-H. Spille**, and U. Kubitscheck. "Light Sheet Microscopy with Enhanced Contrast". *3rd Light Sheet Microscopy Workshop* (13.10.2011).

[26] J. Ritter, **J.-H. Spille**, E. Baumgart, and U. Kubitscheck. "Adjustable light sheet dimensions by a cylindrical zoom lens". *The Second Light Sheet based Fluorescence Microscopy Workshop* (2.09.2010).

[27] J. Ritter, **J.-H. Spille**, R. Veith, J.-P. Siebrasse, and U. Kubitscheck. "Single molecule imaging with light sheet-based microscopy in living tissue". *Microscience* (28.06.2010).

Danksagung

Diese Arbeit wurde am Institut für Theoretische und Physikalische Chemie der Rheinischen Friedrich-Wilhelms-Universität Bonn angefertigt.

Mein besonderer Dank gilt Prof. Dr. Ulrich Kubitscheck. Er hat mir nicht nur die Möglichkeit geboten, dieses spannende Thema zu bearbeiten, sondern auch alle Freiheiten bei der Bearbeitung der Fragestellung gelassen und die Teilnahme an vielen spannenden Konferenzen und Tagungen auf vier Kontinenten ermöglicht. Er war jeder Zeit bereit, eine ehrliche und unvoreingenommene Meinung zum Stand der Arbeit zu äußern und hatte immer ein offenes Ohr für die sich zwangsläufig ergebenden Probleme.

Bei Prof. Dr. Rudolf Merkel, Prof. Dr. Arne Lützen und Prof. Dr. Hanns Häberlein, möchte ich mich für die umgehende, freundliche Bereitschaft bedanken, in der Prüfungskommission mitzuwirken.

Dr. Jörg Ritter hat mich in die Kunst der Lichtscheibenmikroskopie eingewiesen und war eine große Hilfe beim Aufbau des Mikroskops. Tim Kaminski und Katharina Scherer haben viele Stunden im Labor verbracht, um für meine Messungen Mückenlarven zu zerlegen und Lipide in die richtige Anordnung zu bringen. Vielen Dank für eure Mühe und die Geduld, so lange weiterzuarbeiten bis ich endlich mit den Proben zufrieden war. Vielen Dank auch für die vielen inspirierenden und erheiternden Gespräche.

Allen ehemaligen und derzeitigen Mitgliedern der Arbeitsgruppe Biophysikalische Chemie, insbesondere Werner Wendler, sei für ihre Unterstützung und die unkomplizierte und angenehme Atmosphäre gedankt.

Bedanken möchte ich mich auch, stellvertretend für die ganze Feinmechanikwerkstatt unseres Instituts, bei Herrn Backhaus und Herrn Königshoven, ohne deren fachkundigen Ratschlag und tatkräftigen Einsatz das Mikroskop so nicht hätte entstehen können.

Gleiches gilt für die Kooperation mit LaVision BioTec aus Bielefeld, die bereitwillig die Schnittstelle für meine Bildanalysecode geschaffen haben und so die Umsetzung der Arbeit in dieser Form erst ermöglicht haben.

Ebenso haben Jennifer Rinne und Prof. Dr. Alexander Heckel durch die Synthetisierung und Bereitstellung der mehrfach fluoreszenzmarkierten Oligonukleotide eine großen Teil zum Gelingen dieser Arbeit beigetragen.

Schließlich haben die anregenden Diskussionen auf zahlreichen Konferenzen mit Keith Bennett von Hamamatsu Photonics den Anstoß für die Entwicklung der axialen Lokalisierungsmethode gegeben.

Allen Kooperationspartnern danke ich für ihre Hilfe, ebenso wie der Studienstiftung des deutschen Volkes für die finanzielle und ideelle Förderung und der Studienstiftung wie auch dem DAAD für die Förderung zahlreicher Konferenzbesuche auf der ganzen Welt.

Außerhalb des Labors haben mir meine Freunde von FrankN und Bonnsai geholfen, die Lichtscheiben zumindest für ein paar Stunden in der Woche zugunsten einer Plastikscheibe zu vergessen.

Bei meiner Familie möchte ich mich für die fortwährende Unterstützung bedanken. Ihr seid mir jederzeit ein sicherer und verlässlicher Rückhalt.

Karin, danke, dass du da bist!

Erklärung

Hiermit versichere ich, dass ich die vorliegende Arbeit persönlich, selbstständig und ohne Benutzung anderer als der angegebenen Quellen und Hilfsmittel angefertigt habe, sowie direkt oder indirekt übernommene Daten und Konzepte unter Angabe der Quelle kenntlich gemacht habe.
Ich habe keine früheren Promotionsversuche unternommen und die Arbeit wurde bisher weder im In- noch im Ausland in gleicher oder ähnlicher Form einer anderen Prüfungsbehörde vorgelegt.
Für die Erstellung der vorgelegten Arbeit und/oder die Gelegenheit zur Promotion habe ich keine fremde Hilfe, insbesondere keine entgeltliche Hilfe von Vermittlungs- bzw. Beratungsdiensten in Anspruch genommen.

Bonn, den 28. April 2014

Jan-Hendrik Spille